

Studies of
Stars with Neutron Cores
and of
X-ray Binaries displaying
Quasi-periodic Oscillations

Thesis by
Garrett Biehle

In Partial Fulfillment of the Requirements
for the Degree of
Doctor of Philosophy

California Institute of Technology
Pasadena, California

1993

(defended October 22, 1992)

ACKNOWLEDGEMENTS

I have had the privilege of working under two advisors at Caltech and have come to appreciate the viewpoints and attributes of both. I thankfully acknowledge Kip Thorne's patient encouragement and guidance, especially when I entered the field. I appreciate his careful approach to research and his striving to obtain a "deep understanding" of the phenomena in this universe (or sometimes not in this universe). I hope I have learned some of that approach. I also gratefully acknowledge Roger Blandford's encouragement and contagious enthusiasm. I was impressed by his knowledge and whirlwind of ideas, and I hope I have absorbed some of his imagination to generate new ideas.

There are too many other people who have helped me during my stay at Caltech for me to mention everyone by name, but I do especially want to thank Jeremy Mould, Sterl Phinney, and Petr Vogel for always welcoming me into their offices to ask questions. I also thank Tom Tombrello and Claire Patterson for conversations which helped me to understand research in a broader perspective. I thank Curt Cutler, Lars Bildsten, Alice Quillen, and Scott Thornburg for friendly explanation, conversation, and criticism (except for Alice's remark that some of my writing sounded like gobbledy-gook).

I thank Donna Driscoll for getting me out of numerous bureaucratic messes, some of which I did not even know about until later. I thank Shirley Hampton-Parker for making the astrophysics office a cheerful and efficient place. And I thank Michelle Vine for listening to me complain when astrophysics was just frustrating.

ABSTRACT

This thesis contains the results of two investigations: one into the nature of stars with degenerate neutron cores and the other into the interpretation of the phenomenology of luminous low-mass X-ray binaries (LMXBs) displaying slow quasi-periodic oscillations (QPOs) in their X-ray flux.

A star with a degenerate neutron core would be a red giant or supergiant. In this thesis we investigate the structure of such a supergiant, particularly examining the energy production and seeking an identifying observational signature. This star is convective from near the photosphere down to the base of the envelope just outside the degenerate core (radius 10 km). The star's luminosity comes from the rp-process in a convective burning region within 100 km of the base of the envelope. The convection brings fuel for the rp-process into the burning region from throughout the envelope and deposits the products of rp-burning back into the envelope, including the photosphere. After about 10^5 years, the abundances of Br, Rb, Y, and Nb at the surface of the star will be about 200 times greater than their solar abundances, and that of Mo, over 1000 times solar. A suitable observational signature would be the strong enhancement of absorption lines for these elements in the star's spectrum. As many as 10 of the nearest 100 red supergiants (those within 5 kpc) could have neutron cores.

The other investigation concerns a model of rapid accretion onto an unmagnetized neutron star with radius somewhat less than $6GM/c^2$. This model is applied to the phenomenology of a class of LMXBs displaying slow (~ 6 Hz) QPOs in X-ray flux. These sources are highly luminous (approximately Eddington) and display what appears to be three modes ("branches") of accretion. In this model, at low accretion rates, the neutron star lies within the inner edge of the accretion disk, and matter is dripped onto the neutron star from the inner edge. As the accretion rate increases, the transition from the "horizontal branch" to the "normal branch" occurs when the disk thickens and its inner edge touches the star and forms a boundary layer. The formation of a boundary layer changes the structure of the inner disk and the spectral character of the escaping X-rays.

The transition from the normal branch to the “flaring branch” occurs when the boundary layer covers the whole surface of the neutron star and radiation escapes primarily through convective instabilities. This thesis presents an exploration of this model, with an emphasis on establishing the plausibility that a neutron star could indeed lie inside an accretion disk accreting at the observed rate and that a change of mass accretion rate could push the inner radius onto the surface of the star.

CONTENTS

Acknowledgements	ii
Abstract	iii
Chapter 1. Introduction	1
Chapter 2. High-Mass Stars with Degenerate Neutron Cores	16
1. Introduction	17
2. Foundations of supergiant models	22
3. Physical structure	27
4. Nuclear-abundance structure: first model	29
5. Nuclear-abundance structure: second model	48
6. A consistent model	56
7. Possible observations	62
8. Conclusion	64
Appendix	65
Chapter 3. Calculation of Beta-Decay Halflives of Proton-Rich Nuclei of Intermediate Mass	77
Chapter 4. Observational Prospects for Massive Stars with Degenerate Neutron Cores	84
1. Introduction	85
2. Surface nuclear abundances	87
3. Absorption spectroscopy	102
4. Number of T \dot{Z} supergiants in the solar neighborhood	105
5. Conclusion	109
Chapter 5. Hard Apex Transition in Quasi-periodic Oscillators— Closing the Accretion Gap	114
1. Introduction and summary	115
2. Slender accretion disks	118
3. Boundary layer formation	130
4. Mass-Radius relationship for a neutron star	133
5. Discussion	137
Appendix 1	141
Appendix 2	143

Chapter 1

Introduction

Short history of the discovery of degenerate neutron matter

In 1932 Chadwick brought to a favorable end the speculation about the existence of neutrons by producing them in his laboratory. Shortly thereafter two groups independently proposed the existence of gravitationally bound neutron degenerate matter (i.e., what we now call a neutron star) in two astrophysical contexts. Baade and Zwicky (1934) proposed (prophetically, it turns out) that a supernova marks the transition from an ordinary star to a neutron star, and Landau (1937) proposed that a degenerate neutron core could lie in the sun and that the sun's energy could derive from matter falling onto this core (accretion). As a model for the sun, this idea has not prevailed, but we will have plenty to say in this thesis about neutron cores in the center of stars.

During the next thirty years, before any explicit identification of a neutron star, there was some small but sustained theoretical interest in neutron stars in the context of determining the destiny of massive stars. Less massive stars, like our sun, end up as lumps of gravitationally bound electron degenerate matter, but not all stars can end up this way. It slowly became clear that more massive stars end up as neutron stars and the most massive stars as black holes. (But they are not part of our story.) Oppenheimer and Serber (1938), Tolman (1939), and Oppenheimer and Volkoff (1939) worked out an approximate structure of a neutron star and set bounds on the minimum and maximum allowable masses. The destiny of stars interested J. A. Wheeler, Ya. B. Zel'dovich, and others in the 1950s and 60s, and they sought to improve the nuclear equation of state and refine the calculation of the structure of a neutron star.

Confirmation by observation was to take longer for neutron stars than for neutrons, and it is difficult to point to a single event as the first definitive ob-

ervation of a neutron star. For instance, although Baade (1942) and Minkowski (1942) correctly identified the power source of the Crab nebula, they incorrectly identified it as a white dwarf, this despite the fact that the Crab nebula was known to be a supernova remnant and Baade proposed in 1934 that a supernova produces a neutron star. A turning point in neutron star observation came in 1962 when Giacconi *et al.* announced the discovery, using Geiger counter detectors aboard an Aerobee rocket, of non-solar X-rays. The source is now known to be Sco X-1, a bright low-mass X-ray binary (LMXB) (and we will have more to say about LMXBs in this thesis as well). This discovery fueled interest in neutron stars, since many theorists thought (incorrectly) that the X-rays could be coming from a cooling neutron star.

The discovery of a pulsar in 1967 (Hewish *et al.* 1968) and its subsequent identification as a magnetized rotating neutron star brought about an explosion of interest in neutron stars. Since then there have been some thousands of papers written on almost every imaginable aspect of a neutron star's existence: on their creation in supernovae (and possibly in accretion-induced collapse of white dwarfs), on their structure, on their evolution, including magnetic field decay, spin down, and star quakes, and on their behavior in binary systems and in interstellar encounters.

The chapters in this thesis represent a small part of the interest generated by neutron star observations. The first three chapters are concerned with Landau's idea of a degenerate neutron core in the center of a star, this time applied not to the sun but to red supergiants. The fourth is concerned with the phenomenology of certain X-ray sources, those in which the neutron star has a low-mass companion and whose X-ray luminosity displays slow quasi-periodic oscillations.

Stars with degenerate neutron cores

In the thirty years following 1932, while several researchers slowly developed the proposal of Baade and Zwicky, that is, a neutron star as an end stage in a star's life, everyone more or less forgot the idea of Landau. One reason was that Oppenheimer and Serber (1938) showed that the sun could not possibly contain a

degenerate neutron core. Soon the idea prevailed that nuclear fusion provides the energy of the sun (Bethe 1939). Furthermore, as researchers were struggling to understand the events in the life of a star, at no time did a star with a degenerate neutron core appear in their calculations. Except for Fermi's speculation in the 1950s, that such a star—if it existed—would be a red giant, there is no mention of the idea that anyone recalls before the 1970s.

Then in the early 1970s B. Paczyński suggested to A. Żytkow that she use formalism developed for the study of red giants to investigate the idea of a star with a degenerate neutron core. She enlisted the aid of K. Thorne to work out the relativistically correct stellar structure equations, and together they worked out the details of the interface between the neutron degenerate region and the envelope (Thorne and Żytkow 1975, 1977). For this reason these objects are now called Thorne-Żytkow objects or TŻOs. They actually found two classes of solutions for the structure of such stars: TŻ giants and TŻ supergiants.

TŻ giants function more or less like Landau had envisioned. A large tenuous envelope lies on top of an electron degenerate region surrounding a neutron degenerate core. Material gradually accretes onto the core and thus releases energy, and the resulting radiation pressure holds up the envelope. Thorne and Żytkow constructed models for stars with a core mass of $1 M_{\odot}$ and total mass between $3 M_{\odot}$ and $9 M_{\odot}$. For total masses less than about $3 M_{\odot}$ the envelopes are probably not stable to radial oscillations, and there is no equilibrium solution with the above description for stars with total mass greater than $9 M_{\odot}$.

They found that if there existed a solution for the structure of such a star with mass greater than $9 M_{\odot}$ (a TŻ supergiant), then it would have to have the following unusual properties: The envelope would be deeply convective, almost all the way down to the neutron core. Nuclear burning would occur in the lowest several convective cells in the envelope, those hot enough to have a profusion of electron-positron pairs, and this nuclear burning would provide most ($\sim 90\%$) of the luminosity of the star. After a parcel of material had burned its nuclear fuel, it would generally be swept by convection back into the envelope rather than

accreting onto the core.

Interest in TŻOs began to grow in the 1970s for several reasons. By this time theorists were becoming pretty confident of the story of the life history of a star, at least in outline, and so some theorists were beginning to turn their attention to the more complicated stories of binary systems and of stellar encounters. Besides, more data on binary systems was becoming available from X-ray observations made by satellites launched in the 1970s; these provided evidence for the existence of binary systems consisting of a neutron star and an ordinary star in a close orbit. It became natural to ask the question, what is the destiny for a system like Cen X-3? Cen X-3 consists of a neutron star ($\sim 1.4 M_{\odot}$) and an ordinary star ($\sim 20 M_{\odot}$) with an orbital radius ($P_b = 2.1$ days) which is much smaller than the radius of a red giant. The ordinary star must eventually enter a red giant phase. What will happen then? Ostriker and Paczyński (1975, private communication) suggested that this star might engulf the neutron star, which then would spiral to the center, forming a star with a degenerate neutron core.

It now looks as if the fate of a star which swallows a neutron star depends on when the star swallows it. Taam *et al.* (1978) used a one-dimensional hydrodynamic code with dynamic friction and traced the evolution of a star's envelope ($16 M_{\odot}$) from the time when a point mass (the neutron star, $1 M_{\odot}$) has just entered the envelope to the time when it is very close to the center. (The initial and final stages are far more difficult to study.) They found that if the initial orbital period is less than about 120 days, then the envelope is always able to radiate energy away as fast as the neutron star deposited energy into it. If, however, the initial period is greater than 120 days, then the star is somewhat evolved when its surface encounters the neutron star and the interior envelope density is lower than in the previous case. During the last stages of spiral-in, the density is too low to efficiently carry away the deposited energy, and the energy goes into ejecting the envelope. It seems likely, then, that a system like Cen X-3, with a period of 2.1 days, would eventually form a TŻO. Further studies in the process of spiral-in, using a two- and three-dimensional analysis, are currently being carried

out (Taam, 1992, private communication) and these should clarify the issue.

Also in the 1970s, Fabian, Pringle, and Rees (1975) introduced the idea of producing exotic objects (in their case, X-ray sources) in stellar collisions or near-collisions (with tidal effects) in globular clusters. Hills (1976) extended this idea to the interaction of a field star and a binary system. Hut and Paczyński (1984) suggested that TŻOs could result from such an encounter. In their model the field star perturbed the binary in such a way as to cause runaway mass transfer and coalescence. Krolik (1984) discussed the creation of massive nonequilibrium accretion disks about neutron stars and analyzed the number and appearance of such systems. Ray, Kembhavi, and Antia (1987) return to the idea of nearly colliding single stars, this time a neutron star and ordinary star. Among the possible outcomes they include a detached binary, an X-ray binary, a neutron star with an accretion disk, and a TŻO. Recently Davies, Benz, and Hills (1991) have used smooth particle hydrodynamics (SPH) to investigate the collision between a point mass (e.g., a neutron star) and a red giant and have found that the system often forms a common envelope, possibly resulting in a TŻO. It is possible that the TŻOs could eventually become millisecond pulsars, which are observed in globular clusters and whose origin has been controversial. Whereas TŻOs formed in binary systems are likely to be massive, the TŻOs formed by a collision in a globular cluster are light and possibly subject to instabilities.

So interest grew in TŻOs during the 1970s, but not everyone welcomed the reintroduction of stars with degenerate cores into scientific thought. In 1984, Bisnovatyi-Kogan and Lamzin took issue with the boundary condition at the neutron star-envelope interface used by TŻ, saying that the idealized boundary condition artificially suppressed the production of neutrinos in TŻ giants. They claimed that an envelope about a neutron star would necessarily collapse onto the neutron star in a shower of neutrinos and that there are not equilibrium solutions to the stellar structure equations once neutrino production is taken into account.

Eich *et al.* responded in 1989 with a more careful treatment of the neutron star-envelope interface, demonstrating the existence of an equilibrium solution for

TŻ giants. Questions of stability are still open, however, and some people still believe that a TŻO would collapse in a shower of neutrinos (G. S. Bisnovatyi-Kogan and S. Colgate, private communication).

Meanwhile, M. Zimmermann (1979) was working on a more serious flaw in the models of TŻ supergiants. When they constructed their supergiant models, TŻ used a standard expression for nuclear energy production which was derived assuming that a parcel of material had a constant density and temperature and that $^{14}\text{N} + p \rightarrow ^{15}\text{O} + \gamma$ was the limiting reaction. Because the burning region in TŻ supergiants is convective, so that a parcel of material experiences rapid change in density and temperature, and because the timescales for convective turnover and beta decay are longer than for proton addition onto ^{14}N , the expression used in TŻ was clearly not applicable. (TŻ were aware of this flaw, but they produced models in order to give some idea as to how they might look.)

Zimmermann searched for a consistent model for a TŻ supergiant with total mass $16 M_{\odot}$ and a $1 M_{\odot}$ core. He addressed the problem of modeling a convective burning region by solving the physical structure (density and temperature as a function of radius) and the nuclear-abundance structure (nuclear abundances as a function of radius) separately. An integration of the stellar structure equations yields a one-parameter family of envelopes in the $(L_{\text{ph}}, T_{\text{ph}})$ plane which have a $1 M_{\odot}$ core. Given a particular envelope, he first determined the physical structure. He then determined the nuclear-abundance structure using diffusion equations, setting a generalized diffusion constant (to order of magnitude) equal to the product of convective velocity and pressure scale height (as a function of radius). The boundary condition at the base of the envelope was determined in a complicated way using an extensive nuclear reaction network (hot CNO) for the isotopes with $Z \leq 11$. Given a nuclear-abundance structure, he calculated the luminosity produced at the base of the envelope L_{nuc} . A consistent model is obtained if $L_{\text{nuc}} = L_{\text{ph}}$ for one of the envelopes. He found that as long as he kept the temperature at the base of the envelope less than 2×10^9 K (above which the hot CNO reactions are not applicable) he always obtained $L_{\text{nuc}} \lesssim 0.05 L_{\text{ph}}$, so

that he did not find a consistent model.

Chapter 2 of this thesis continues the search for a consistent model for a T \dot{Z} supergiant. We use Zimmermann's strategy of solving the physical structure and nuclear-abundance structure separately, but we now employ a nuclear reaction network appropriate for a hydrogen-rich environment with $T \gtrsim 10^9$ K, that is, the rp-process (Wallace and Woosley 1981). In this model convection carries down fuel (C, N, O, and H) from the outer envelope. In the burning region at the base of the envelope the temperature and density are high enough that the CNO fuel nuclei break out of the CNO cycle into the rp-process. In the rp-process nuclear seeds (initially C, N, and O) undergo alternately proton addition and positron decay until heavy elements are produced (heavier than Fe). In the star this happens like this: Convection carries down a seed nucleus (any nucleus with $Z \geq 10$) to the burning region at the base of the envelope. It quickly burns by proton addition to a proton-rich species at the proton drip line. Since no further strong reactions may occur, convection sweeps the seed back out into the cooler portions of the envelope. It random walks around (because of convection) until it decays. If the decay time is short, then the decay probably occurs at a small radius, and the seed is likely to random walk back to the burning region to add more protons and produce more energy. On the other hand, if the decay time is long, then the decay probably occurs at a large radius, and the seed is more likely to random walk to the surface of the star than back down to the burning region. Chapter 2 answers in the affirmative the question, is this process efficient enough to produce the energy required to maintain the distended envelope? That is, we present a model for which $L_{\text{nuc}} = L_{\text{ph}}$.

The convection of some long-lived proton-rich species to the surface of the star, although bad news for sustaining the rp-process and producing energy, is good news for providing an observational signature for a T \dot{Z} supergiant. The reaction network used in Chapter 2 was adequate to predict the dominant source of energy for the star, but in order to predict surface abundances on a T \dot{Z} supergiant, we needed to improve the nuclear physics. In Chapter 3 we present part of

the improvement in the nuclear physics: a calculation of the halflives of several proton-rich beta-unstable species using the random phase approximation with the quasiparticle formalism. In Chapter 4 we use the new halflives and improve other nuclear physics in order to predict the surface abundances of elements heavier than Fe.

In Chapter 4 we determine that the abundances of Mo, Ru, Rh, Pd, and Ag on the surface of a TŻ supergiant should be over 1000 times their solar abundances. The abundances of these elements determines the strength of absorption lines in the star’s optical spectrum. Current technology in optical spectroscopy can easily achieve the spectral resolution necessary to measure these abundances and determine whether a red supergiant has a nondegenerate core (i.e., a “normal” supergiant) or a neutron degenerate core (i.e., a TŻ supergiant). It is hoped that this work will lead to an observational project which will identify a TŻO.

Low-mass X-ray binaries exhibiting quasi-periodic oscillations

Whereas the subject of TŻOs consists of theory but no direct observations (yet), the subject of low-mass X-ray binaries is rich in observations and phenomenology but lacking in a comprehensive theory which would explain the observations. In the early 1980s it became clear that there were two populations of galactic X-ray sources. (See White and Mason 1985 for an early review.) The one population consists of about 150 sources (100 of which are transient) whose ratio of X-ray luminosity to optical luminosity is less than 1, which have longer periods (2-300 days), which are found in the galactic disk among older (Population I) stars, and which occasionally have X-ray pulsations and eclipses. It was soon realized that the companion in these systems is a massive ($\gtrsim 16 M_{\odot}$) main sequence star (O, B, or Be), hence the name high-mass X-ray binary (HMXB). The other population consists of about 100 sources whose X-ray luminosity far exceeds their optical luminosity by a factor of 10-1000, which are faintly blue in the optical, which have short periods (4-48 hours), which are found primarily in the galactic bulge but also in globular clusters among younger (Population II) stars, and which do not eclipse or pulse. In these systems the companion is a low-mass

($\lesssim 1 M_{\odot}$) (F, G,) K or M star, hence the name low-mass X-ray binary (LMXB). Because LMXBs show no pulsations, it is generally assumed they have small magnetic fields ($< 10^{11}$ gauss); however, several have shown cyclotron lines, indicating a $\sim 10^{12}$ gauss magnetic field (Her X-1, Mihara *et al.* 1990; 4U 0115+63, Nagase *et al.* 1991; 4U 1538–52, Clark *et al.* 1990; V 0332+53, Makishima *et al.* 1990; Cep X-4, Mihara *et al.* 1991; among others)

The origin of LMXBs has proved quite a puzzle: How can the orbital radius lie not only within the radius of the red giant precursor to the neutron star but often within the radius of the massive main sequence precursor to the red giant? One creation scenario (van den Heuvel 1983) begins with a wide binary with stars of somewhat disparate masses. When the more massive star becomes a red giant, it swallows the less massive star, which spirals toward the center and ejects the red giant envelope during the final stages of spiral-in, thus forming a helium star and the less massive main-sequence star. The helium star undergoes supernova, and the resulting binary system circularizes via tidal interaction. A LMXB forms when the main-sequence star overflows its Roche lobe. A second creation scenario begins with a similar wide binary which becomes a white dwarf and main-sequence star after the spiral-in and envelope ejection. When the main-sequence star overflows its Roche lobe, the white dwarf accretes enough matter to exceed the Chandrasekhar limit and it collapses to a neutron star, thus forming a LMXB after circularization. The third creation scenario (Eggleton and Verbunt 1986), also the most exotic, begins with a triple system: a massive close binary and a circumbinary low-mass main-sequence star. The massive close binary forms a TŻO in a way we have discussed before. This TŻO swallows the low-mass star, which spirals in and ejects the TŻO envelope, thus forming a LMXB.

The LMXBs naturally divide into two luminosity classes (van Paradijs and Lewin 1986): The lower-luminosity objects (10^{36-37} erg s $^{-1}$) are generally bursters (which produce continuous X-rays punctuated by bursts) and soft X-ray transients. The ~ 10 higher-luminosity objects ($\gtrsim 10^{38}$ erg s $^{-1}$) are continuous sources of a wide spectral range of X-rays. Of these 10 there are 6 whose X-ray flux dis-

plays quasi-periodic oscillations (QPOs) at 6-60 Hz. The fifth chapter of this thesis is concerned with this final class of objects.

The following picture of LMXBs with QPOs gradually emerged in the years 1971-1987: When the X-ray flux from an individual source is plotted on a two-color diagram over a period of 1-10 hours, the flux traces a one-parameter locus resembling a stylized **Z** (see Figure 1 of Chapter 5 or Figure 1 of Hasinger 1988). Actually, most sources trace only two strokes, or “branches”, of the **Z**, but Cyg X-2, Sco X-1, and GX 17+2 have shown activity on all three branches. It turns out that the phenomenology of a source depends on what branch of the **Z** it is on: the horizontal branch (HB, the top stroke), the normal branch (NB, the cross stroke), or the flaring branch (FB, the bottom stroke). It is believed that the position on the **Z** is governed by the mass accretion rate, and that accretion rate increases in the direction one would normally draw a **Z** (Vrtilek *et al.* 1991). The mass accretion rate is on the order of the Eddington limit, and the full range of the **Z** represents about a factor of 2 in mass accretion rate.

The Fourier spectrum of the X-ray intensity roughly follows a power law from 10^{-2} - 10^2 Hz on all three branches. In addition, however, on the HB there is an excess of power in the range 0.1-10 Hz, called the low-frequency noise (LFN). And there is a low- Q ($Q \sim 4$ -9) quasi-periodic oscillation (HB QPO) whose frequency varies from 10 to 60 Hz positively correlated with the mass-accretion rate. This oscillation has been seen on occasion at the top of the NB (Hasinger *et al.* 1990). A possible clue to the origin of these QPOs is the fact that the hard X-ray photons trail the softer X-ray photons by 0.2-4 ms (“hard lag”). It is believed that some softer photons are scattered up in energy by hot electrons. (See Hasinger 1986 and van der Klis *et al.* 1987.)

On the NB there is no LFN; in fact, the LFN cuts off abruptly and dramatically ($\lesssim 200$ s) as a source moves from the HB to the NB (Hasinger 1988). On the middle and lower portion of the NB there is a ~ 6 Hz quasi-periodic oscillation (NB QPO). That there are two mechanisms for these oscillations was confirmed by the occasional simultaneous observation of both (Hasinger *et al.* 1990 and ref-

erences therein). In the case of NB QPOs the hard photons trail the softer X-ray photons by about 80 ms. Also, most of the oscillation occurs in the harder photons ($\gtrsim 9$ keV). (See Mitsuda and Dotani 1989.) On the FB there is sometimes a QPO which, it is conjectured, has the same mechanism as the NB QPO. The correlation of QPO frequency (6-10 Hz) with intensity is, however, erratic. There is no LFN.

Two (related) theories have been developed to explain the QPOs on the HB and NB. In the beat-frequency model (BFM) (Alpar and Shaham 1985, Lamb *et al.* 1985, Shibazaki and Lamb 1987), which applies to the HB QPO, the neutron star has a magnetic field and matter is accreted from lumps which form by some instability at the Alfvén radius. Accretion is facilitated when the magnetic field lines up with a lump, so that the QPO frequency is given by the difference of the orbital frequency at that radius and the neutron star spin frequency (hence, the beat frequency). As the accretion rate increases, the Alfvén radius shrinks and the QPO frequency increases. A problem with this theory is that the fundamental spin frequency has not been observed in the QPO sources. Also, the lumps of material need to have a lifetime of at least several orbital times, and it is difficult to see how they could avoid getting sheared into smoothness in much less than an orbital time.

Another theory, applying to the NB QPO, holds that the neutron star is surrounded by a hot spherical corona, in addition to a thin accretion disk (Lamb 1989, Fortner *et al.* 1989, Miller and Lamb 1992). The mass accretion rate from the corona is modulated by an overstable variation in opacity in the corona at a radius of about 300 km. That is, an increase in accretion rate causes a shower of photons at the neutron star surface. These photons stream outward and interact with the infalling matter at ~ 300 km, choking off the inflow and decreasing the accretion rate. This happens in an overstable manner in order to create the NB QPO. It is not clear how much tuning is needed in this model in order to obtain the relatively constant ~ 5 -7 Hz observed among several sources. Other models have been proposed (Alpar *et al.* 1992) involving slow oscillations in a thick accretion

disk.

In Chapter 5 we propose a different model from the above. In this model the three branches of the **Z** represent three modes of accretion, and transitions among branches correspond to changes in the interface between the star and the accretion disk. We propose that the neutron star lies within the inner radius of the accretion disk on the HB, and matter is dripped onto the neutron star from the inner edge. (See Kluźniak and Wagoner 1985, Kluźniak and Wilson 1991, Sunyaev and Shakura 1986, and Shakura and Sunyaev 1988.) As the accretion rate increases, the transition to the NB occurs when the inner edge of the accretion disk touches the neutron star and forms a boundary layer. As the accretion rate increases further, the boundary layer becomes thicker. The transition from the NB to the FB occurs when the boundary layer covers the whole surface of the neutron star and radiation escapes primarily through convective instabilities.

Chapter 5 is an exploration of this model, with an emphasis on establishing the plausibility that a neutron star could indeed lie inside an accretion disk accreting at the observed rate and that a change of mass accretion rate could push the inner radius onto the surface of the star. We also speculate as to how this model could produce the observed spectral pattern (**Z** shape on the two-color plot).

REFERENCES

- Alpar, M. A., Hasinger, G., Shaham, J., & Yancopoulos, S. 1992, *A&A*, **257**, 627.
- Alpar, M. A., & Shaham, J. 1985, *Nature*, **316**, 239.
- Baade, W. 1942, *ApJ*, **96**, 188.
- Baade, W., & Zwicky, F. 1934, *Phys. Rev.*, **45**, 138.
- Bethe, H. 1939, *Phys. Rev.*, **55**, 434.
- Bisnovaty-Kogan, G. S., & Lamzin, S. A. 1984, *Astron. Zh.* **61**, 323 [English trans. in *Sov. Astron.-A. J.*, **28**, 187].
- Chadwick, J. 1932, *Nature*, **129**, 312, and *Proc. Roy. Soc.*, **A136**, 692.
- Clark, G. W., Woo, J. W., Nagase, F., Makishima, K., & Sakao, T. 1990, *ApJ*, **353**, 274.
- Davies, M. B., Benz, W., Hills, J. G. 1991, *ApJ*, **381**, 449.
- Eggleton, P. P., & Verbunt, F. 1986, *MNRAS*, **220**, 13P.
- Eich, C., Zimmermann, M. E., Thorne, K. S., & Żytkow, A. N. 1989, *ApJ*, **346**, 277.
- Fabian, A. C., Pringle, J. E., & Rees, M. J. 1975, *MNRAS*, **172**, 15P.
- Fortner, B., Lamb, F. K., & Miller, G. S. 1989, *Nature*, **342**, 775.
- Giacconi, R., Gursky, H., Paolini, F., & Rossi, B. 1962, *Phys. Rev. Lett.*, **9**, 439.
- Hasinger, G. 1986, in *The Origin and Evolution of Neutron Stars, IAU Symposium 125*, ed. D. J. Helfand & J. H. Huang (Dordrecht: Reidel).
- Hasinger, G. 1988, in *Physics of Neutron Stars and Black Holes*, ed. Y. Tanaka (Tokyo: Universal Academy Press), p. 97.
- Hasinger, G., van der Klis, M., Ebisawa, K., Dotani, T., & Mitsuda, K. 1990, *A&A*, **235**, 131.

- Hewish, A., Bell, S. J., Pilkington, J. D. H., Scott, P. F., & Collins, R. A. 1968, *Nature*, **217**, 709.
- Hills, J. G. 1976, *MNRAS*, **175**, 1P.
- Hut, P., & Paczyński, B. 1984, *ApJ*, **284**, 675.
- Kluźniak, W., & Wagoner, R. V. 1985, *ApJ*, **297**, 548.
- Kluźniak, W., & Wilson, J. R. 1991, *ApJ*, **372**, L87.
- Krolik, J. H. 1984, *ApJ*, **282**, 452.
- Lamb, F. K. 1989, *Proc. 23rd ESLAB Symposium on X-ray Astronomy*, ed. N. E. White (ESA SP-296), p. 215.
- Lamb, F. K., Shibazaki, N., Alpar, M. A., & Shaham, J. 1985, *Nature*, **317**, 617.
- Landau, L. D. 1937, *Doklady Akad. Nauk USSR*, **17**, 301 [English trans. in *Nature*, **141**, 333 (1938)].
- Makishima, K., Mihara, T., Ishida, M., Ohashi, T., Sakao, T., Tashiro, M., Tsuru, T., Kii, T., Makino, F., Murakami, T., Nagase, F., Tanaka, Y., Kunieda, H., Tawara, Y., Kitamoto, S., Miyamoto, S., Yoshida, A., & Turner, M. J. L. 1990, *ApJ*, **365**, L59.
- Mihara, T., Makishima, K., Ohashi, T., Sakao, T., Tashiro, M., Nagase, F., Tanaka, Y., Kitamoto, S., Miyamoto, S., Deeter, J. E., & Boynton, P. E. 1990, *Nature*, **346**, 250.
- Mihara, T., Makishima, K., Kamijo, S., Ohashi, T., Nagase, F., Tanaka, Y., & Koyama, K. 1991, *ApJ*, **379**, L61.
- Miller, G. S., & Lamb, F. K. 1992, *ApJ*, **388**, 541.
- Minkowski, R. 1942, *ApJ*, **96**, 199.
- Mitsuda, K., & Dotani, T. 1989, *Pub. Astr. Soc. Japan*, **41**, 557.
- Nagase, F., Dotani, T., Tanaka, Y., Makishima, K., Mihara, T., Sakao, T., Tsunemi, H., Kitamoto, S., Tamura, K., Yoshida, A., & Nakamura, H. 1991, *ApJ*, **375**, L49.

- Oppenheimer, J. R., & Serber, R. 1938, *Phys. Rev.*, **54**, 540.
- Oppenheimer, J. R., & Volkoff, G. M. 1939, *Phys. Rev.*, **55**, 374.
- Ray, A., Kembhavi, A. K., & Antia, H. M. 1987, *A&A*, **184**, 164.
- Shakura, N. I., & Sunyaev, R. A. 1988, *Adv. Space Res.*, **8**, 135.
- Shibazaki, N., & Lamb, F. K. 1987, *ApJ*, **318**, 767.
- Sunyaev, R. A., & Shakura, N. I. 1986, *Sov. Astron. Lett.*, **12**, 117.
- Taam, R. E., Bodenheimer, P., & Ostriker, J. P. 1978, *ApJ*, **222**, 269.
- Thorne, K. S., & Żytkow, A. N. 1975, *ApJ*, **199**, L19.
- Thorne, K. S., & Żytkow, A. N. 1977, *ApJ*, **212**, 832 (TŻ).
- Tolman, R. C. 1939, *Phys. Rev.*, **65**, 364.
- van den Heuvel, E. P. J. 1983, in *Accretion Driven Stellar X-ray Sources*, p. 303, eds. W. H. G. Lewin & E. P. J. van den Heuvel (Cambridge: Cambridge Univ. Press).
- van der Klis, M., Hasinger, G., Stella, L., Langmeier, A., van Paradijs, J., & Lewin W. H. G. 1987, *ApJ*, **319**, L13.
- van Paradijs, J., & Lewin, W. H. G. 1986, in *The Evolution of Galactic X-ray Binaries*, eds. J. Trümper, *et al.* (Dordrecht: Reidel), p. 87.
- Vrtilek, S. D., Penninx, W., Raymond, J. C., Verbunt, F., Hertz, P., Wood, K., Lewin, W. H. G., & Mitsuda, K. 1991, *ApJ*, **376**, 278.
- Wallace, R. K., & Woosley, S. E. 1981, *ApJS*, **45**, 389.
- White, N. E., & Mason, K. O. 1985, *Space Sci. Rev.*, **40**, 167.
- Zimmermann, M. E. 1979, Ph.D. thesis, Caltech, available as OAP 586.

Chapter 2

High-Mass Stars with Degenerate Neutron Cores

*Garrett T. Biehle**Adagio*

Except for the addition of several paragraphs and tables in this thesis, this chapter originally appeared in *Astrophysical Journal*, **380**, 167 (1991).

1. Introduction and summary

Work on stars with degenerate neutron cores has waxed and waned ever since these stars were proposed in the 1930s. Early work includes that of Gamow (1937) and Landau (1937). Later (c. 1950), Fermi (unpublished) speculated that such stars would be red supergiants. The first detailed analysis of steady-state models of massive stars with degenerate neutron cores was performed by Thorne and Żytkow (1977, hereafter TŻ). They confirmed Fermi's speculation, finding that such stars with masses between 3 and 25 M_{\odot} would have luminosities between 30,000 and 130,000 L_{\odot} and surface temperatures between 2600 and 3100 K. These features are common to any star with a 1 M_{\odot} compact core and inner temperatures hot enough to ignite nuclear burning. Such a star would look very much like a red giant with a degenerate electron core, residing in the HR diagram just on the stable side of the Hayashi forbidden region.

In their work Thorne and Żytkow built successful models (which they called "giants") for stars with total mass less than 9 M_{\odot} and a core mass of 1 M_{\odot} . The luminosity of these giant stars was produced almost entirely by gradual, steady accretion of the envelope onto the core, though there was a small contribution from nuclear burning.

Thorne and Żytkow did not, however, succeed in building fully satisfactory models for stars more massive than 9 M_{\odot} with 1 M_{\odot} neutron cores. They showed, however, that such stars (which they called "supergiants") (1) must have luminosities in excess of 70,000 L_{\odot} , (2) cannot produce their required luminosities primarily by gradual, steady accretion onto the core, and (3) might be able to produce their luminosities primarily by nuclear burning, but only if convection extends continuously from the base of the nuclear burning region (just above the core) out to the star's photosphere. (In §2.1 we shall review the Thorne-Żytkow proof of these properties.) Thorne and Żytkow built a set of admittedly flawed models of such stars, based on normal CNO burning without proper account of the convection sweeping material into and out of the burning region. These models had masses greater than 12 M_{\odot} . No models were found in the "mass gap"

between 9 and 12 M_{\odot} .

Zimmermann (1979) tried to correct this flaw in TŻ by building supergiant models based on the hot CNO cycle and a convective burning region, but these models failed. (See also the summary of Zimmermann's work in Eich *et al.* 1989.) The failure had two causes: (1) The fuel was cycled into and out of the burning region so rapidly that there was inadequate time for the hot CNO cycle's beta decays to go to completion in the burning region. By the time the beta decays were complete, most of the fuel was back up at such great radii and low temperatures that it could not undergo the strong-interaction part of the cycle. (2) This impediment to the hot CNO cycle was partially circumvented (the energy generation was increased) by pushing the burning region to higher and higher temperatures, but long before the energy generation was great enough to support the star, the temperatures were so high that the burning broke out of the hot CNO cycle and into the rp-process (i. e., the rapid-proton process) (Wallace and Woosley 1981).

This paper takes up the next step, constructing models with a convective burning region based on the rp-process. These models are spherically symmetric, nonrotating, nonmagnetic, nonaccreting, and Newtonian. As such, the models have systematic errors of about 10% and are meant to elucidate only the essential features of such a star. The bottom line of the analysis is that rp burning can indeed provide the required luminosity when the envelope mass is above the upper edge of a mass gap ($M_{\text{env}} > M_{\text{upper}} \sim 16 M_{\odot}$). More specifically, the analysis produces self-consistent stellar models with the following type of structure:

Near the base of the envelope, temperatures are on the order of 10^9 K; densities, 10^4 g cm $^{-3}$; and typical turbulent (convective) velocities, 10^7 cm s $^{-1}$. Convective mixing brings fresh material down from the outer layers of the envelope and takes burned material and reaction intermediates away from the inner layers. In the hot, innermost several tens of kilometers of the envelope, temperatures and densities are such that protons are rapidly pushed onto the nuclei, thereby building up heavier and heavier metals in a nonequilibrium process. Enough energy is thereby produced to maintain the convection and supply the luminosity radiated

from the photosphere.

The convection, which extends from the base of the burning region all the way out to the photosphere, carries rp-process reaction products into the photosphere, where they might be observable. The most promising spectral feature of these reaction products is the rotational structure of absorption lines from hydrides of certain heavy, proton-rich nuclei. A promising example is ^{84}SrH . Observation of such a molecule on the surface of a red supergiant star would be strong evidence that the star has a degenerate neutron core rather than an degenerate electron core. Another diagnostic would be an overabundance of several elements with $32 \leq Z \leq 40$ on the surface of the star, although precisely which elements would be difficult to determine. (However, see Chapter 4 of this thesis.)

The prospects for discovering such stars depend on their rate of formation and their lifetimes. The formation of such stars (if they ever form at all) is poorly understood. The most promising mode of formation is in massive binary systems, where the more massive star evolves into a neutron-star state and then might be captured by and sink into the core of its companion. See Taam, Bodenheimer, and Ostriker (1978); Taam (1979); Hut and Paczyński (1984); Cameron and Iben (1986); and Ray, Kembhavi, and Antia (1987) for some discussion. The formation rate by this process is presumably far lower than the rate of formation of normal red supergiants, i. e., with degenerate electron cores.

The rp burning phase terminates with exhaustion of the envelope's supply of light metals (^{12}C , ^{14}N , and ^{16}O), which act as seeds for the rp-process. If the envelope abundances are Population I (say, 2% light metals by mass), then the duration of the rp burning would be about 1×10^6 yr for a $16 M_{\odot}$ star (roughly the same as the life of a red supergiant with degenerate electron core). If earlier phases of evolution have enhanced the light-metal abundance beyond Population I, the rp phase would be correspondingly longer.

The star's fate, after exhausting its light metals, is far from clear. If no other source of energy can be tapped, then the envelope presumably will collapse onto the core, and the star, as a red supergiant, will be extinguished; however,

(as E. Salpeter 1990, private communication, has pointed out) the star might be able to tap its huge store of gravitational energy by means of nonsteady and/or nonspherical accretion of the envelope onto the core, an accretion in which the inner portion of the envelope might undergo relaxation oscillations, while the outer envelope remains little changed from the earlier, rp burning phase. If this happens (and if the envelope has not long been driven away by stellar winds), then its lifetime as a star with peculiar abundances could be extended by an additional $\sim 2 \times 10^7$ yr. It is unlikely that these lifetimes are enough larger than those of a normal red supergiant with degenerate electron core to compensate for a far smaller formation rate. Accordingly, at most only a small fraction of the red supergiants in our Galaxy are likely to have degenerate neutron cores.

Almost all of this paper is devoted to building models for the envelope of a star with total mass $16 M_{\odot}$ and with a $1 M_{\odot}$ core. We begin, in §2, by laying foundations for the model building. Specifically, we sketch a derivation of the three properties of such a star that were discussed in the third paragraph of this section. Then we argue that if we want to establish that such a star can be supported by nuclear burning, then we need not build models for the full star but only build models of the envelope, from the base of the burning region (just above the degenerate neutron core) out to the photosphere. We argue that an appropriate strategy will entail splitting the envelope's structure into two parts: its physical structure and its nuclear-abundance structure with associated nuclear energy generation.

In §3 we build a one-parameter family of models for the physical structure (density, temperature, turbulent velocity, and so on) of the star's envelope under the idealized assumption that the star's luminosity is all generated in an infinitesimally thin region at the base of the convective zone (bottom of the envelope). Each model is for a $15 M_{\odot}$ envelope that joins smoothly onto a $1 M_{\odot}$ core. The models differ slightly in their total luminosities but differ greatly in the temperature and density of the energy-generation region.

In §4 we build a first model for the nuclear-abundance structure and its nu-

clear energy generation for each of the envelopes constructed in §3. Zimmermann's models failed because the long beta decays required by the hot CNO cycle prevented sufficient energy generation. Consequently, in this section we investigate whether the rp-process is plagued by the same difficulty. Energy generation is assumed to occur in the infinitesimally thin base of the convective zone, and the radial distribution of nuclear abundances is computed using a simple diffusion equation for material transport and using a simplified rp reaction network. From the radial distribution of abundances, we compute the total nuclear energy generation. One envelope is found (with luminosity $88,600 L_{\odot}$) which is self-consistent, that is, the computed nuclear energy generation is equal to that required by the model's physical structure. We argue that the long beta decays do not prevent the rp-process from producing the required energy, even when the model's idealizing assumptions are relaxed.

In §5 we relax one of the idealizing assumptions in §4, that is, that the energy is produced in an infinitesimally thin region. Using the physical envelopes of §3, we compute the radial distribution of the energy generation by letting the rp-process occur at several radii in the envelope. (In order to keep the model tractable, we no longer consider all the beta decay parents of §4, thus idealizing what we once investigated.) We find the local luminosity as a function of radius and discover that the resulting local luminosity is still everywhere in the envelope great enough to power the convection (this is a vital check on self-consistency).

In §6 we input the local luminosity function from §5 back into our calculation of the physical model, thereby relaxing the physical model's idealization of energy generation in an infinitesimally thin region. The new physical model is then used as the foundation for a new nuclear-abundance model, and the new nuclear-abundance model is found to be nearly the same as that in §5. This means that we have achieved our goal: We have constructed mutually consistent physical and nuclear-abundance structures for a $16 M_{\odot}$ star with a $1 M_{\odot}$ core with properties consistent with the discussion in §2. Several properties of this model are briefly discussed.

In §7 we discuss the possibility of using spectral lines from the hydrides of rp-process nuclei to distinguish such a star from one with a degenerate electron core. Finally, in §8 we give a brief, concluding summary.

2. Foundations of supergiant models

This section describes general features that any supergiant star with a degenerate neutron core must have and sketches a general strategy for constructing such models.

We seek spherically symmetric, nonrotating, Newtonian models without magnetic fields, which are in slowly evolving steady states (i.e., which have density, temperature, and nuclear abundances varying on time scales long compared with the star’s hydrodynamic and thermal diffusion times). Specifically, we seek such models for a star of mass $16 M_{\odot}$ with a $1 M_{\odot}$ core. Constructing such a model consists of determining density, temperature, and nuclear abundances as functions of radius (and only weakly as functions of time). We shall see that it is enough to determine these quantities for the region extending from just outside the core to the surface of the star. We will define the “edge of the core” to be the radius at which significant energy production and thus convection begin (called the “knee” in TŻ).

2.1. General features

First we ask the question, if a model of the type described above is to exist, what features must it incorporate? We will find that a model must have the following characteristics: 1) The local luminosity L_r (luminosity flowing across a shell of constant radius r) must rise very quickly to about the star’s full luminosity just outside the degenerate region of the core. 2) Most of this luminosity must be provided by nuclear reactions. 3) Convection must extend from the photosphere into the hydrogen burning region, so the nuclear reactions are in nonequilibrium. These three characteristics can be seen from the following arguments, summarized from TŻ.

The force balance equation for the plasma gas is

$$-\frac{dP_g}{dr} - \frac{GM_r\rho}{r^2} + \frac{\kappa\rho L_r^{\text{rad}}}{4\pi cr^2} = 0, \quad (1)$$

where r is the radius, P_g is pressure due to the plasma (gas), M_r is the mass contained in radius r , ρ is the density, κ is opacity (due to Compton scattering), $L_r^{\text{rad}} = L_r - L_r^{\text{conv}}$ is local radiative luminosity, and L_r^{conv} is the convective luminosity. This force balance equation can be rewritten as follows:

$$\frac{dP_g}{dr} = -\frac{GM_r\rho}{r^2} \left(1 - \frac{L_r^{\text{rad}}}{L_r^{\text{crit}}}\right), \quad (2)$$

where $L_r^{\text{crit}} = 4\pi cGM_r/\kappa$. The symbol L_r^{crit} is the Eddington critical luminosity, that is, the luminosity at which radiation pressure balances gravitational attraction. Using the ideal gas equation

$$P_g = \frac{\rho k_B T}{\mu_e m_H},$$

where k_B is the Boltzmann constant, μ_e is the mean molecular weight (unitless), and m_H is the mass of the hydrogen atom, we obtain for the pressure scale height

$$\begin{aligned} l_{\text{pres}} &\equiv -\frac{P_g}{dP_g/dr} \\ &= (6 \times 10^{-4} r) \left(\frac{T}{10^9 \text{K}}\right) \left(\frac{1}{\mu_e}\right) \left(\frac{r}{10 \text{km}}\right) \left(\frac{M_r}{M_\odot}\right)^{-1} \left(1 - \frac{L_r^{\text{rad}}}{L_r^{\text{crit}}}\right)^{-1}. \end{aligned} \quad (3)$$

In order to have an extended envelope, we must have l_{pres} be on the order of r . In order for this to happen, just outside the region of electron degeneracy L_r^{rad} must rise to nearly L_r^{crit} . Such a rise will trigger convection, which will easily carry a luminosity somewhat larger than L_r^{crit} . We can approximate L_r^{crit} by substituting $1 M_\odot$ for M_r and the opacity due to the low-energy Thomson cross section for κ :

$$L_r^{\text{crit}} \approx \frac{4\pi cGM_{\text{core}}}{\kappa_{\text{Thomson}}} \approx 30,000 L_\odot.$$

A better estimate can be obtained by substituting the opacity due to the Compton cross section at a temperature just below that required to produce electron-positron pairs. In that case we obtain $L_r^{\text{crit}} \approx 80,000 L_\odot$. In the models of TŻ this luminosity was provided by gravitational energy release and by nuclear burning.

The second and third requirements (luminosity due largely to nuclear burning and convection from burning zone to photosphere) come out of the following considerations: Consider integrating the stellar equations inward from the photosphere toward the center. The local luminosity L_r begins at a high value ($\sim 10^5 L_\odot$) at the photosphere and must somehow decrease to zero (to satisfy the boundary condition in the interior: $L_r = 0$ at $r = 0$). Refer to Figure 1, in which are shown the results from two models in TŻ. Local luminosity is plotted versus temperature, along with the Eddington critical luminosity. (The script R is a general relativistic correction; the Thorne-Żytkow models included the effects of general relativity, but ours will not.) For low temperatures L_r^{crit} is approximately constant because the opacity, due mainly to electron scattering, is constant. In this figure we see L_r^{crit} rise with increasing T as relativistic corrections to the Thomson cross section become significant. At $\log T \sim 8.7$ the temperature becomes great enough to produce electron-positron pairs, the opacity κ then rises because of the increased number of scatterers, and L_r^{crit} plummets. Thus, there is a local maximum in L_r^{crit} at $\log T \sim 8.7$.

Now, there are two mechanisms by which the actual luminosity L_r could be turned off as r decreases (and T increases): 1) At some radius the critical luminosity may rise above the local luminosity; then convection turns off and the gravitational energy of accreting matter is converted to heat. (As long as the total luminosity is greater than the critical luminosity, there is convection, which is nearly adiabatic, and little gravitational energy is converted to heat.) 2) Temperatures and densities may become high enough to initiate nuclear burning, which causes L_r to turn off with decreasing r .

The former mechanism dominates in stars less than $9 M_\odot$ (called “giants” in TŻ). For stars greater than $9 M_\odot$ (called “supergiants” in TŻ) the luminosity at the photosphere is greater than the maximum L_r^{crit} (i. e., the local maximum in Figure 1), so L_r^{crit} never rises above L_r , and the former mechanism fails. If a model is to be found in this mass range, it must employ the second mechanism, which means that nuclear burning must turn on while the envelope is still convective.

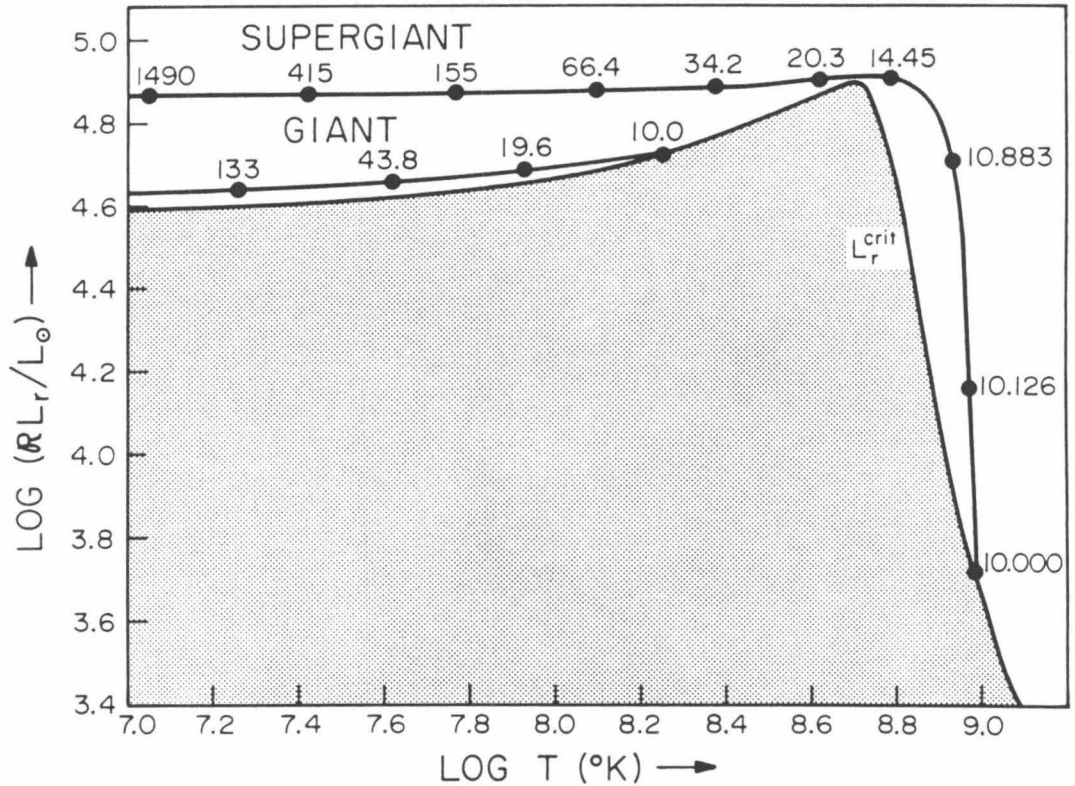


Fig. 1—Local luminosity L_r and Eddington critical luminosity L_r^{crit} plotted as functions of temperature T for two models: a $5 M_\odot$ giant model and a $12 M_\odot$ supergiant model constructed by TŽ. (The script R is a general relativistic correction.) The L_r curves are parameterized by the radius r in kilometers. The edge of the core occurs where L_r goes subcritical ($r \simeq 10$ km).

Hence, for a $16 M_{\odot}$ star, say, we know that at least a portion of the nuclear burning zone is convective. Also, because the L_r^{crit} falls so quickly as T increases, and because the various nuclear mechanisms turn on somewhat after $\log T$ exceeds 8.7, L_r^{crit} will be comparatively small when L_r finally decreases enough to equal it. Thus nuclear energy generation must account for most of the luminosity ($\sim 90\%$), with gravitational energy release accounting for the remainder ($\sim 10\%$).

To summarize, if a spherical, steady-state model for a $16 M_{\odot}$ star is to exist, it must entail an envelope (1) which is convective from the photosphere almost to the neutron star surface, (2) in which nuclear reactions occur predominantly in the convective cell nearest the neutron star surface, and (3) in which these nuclear reactions provide most of the luminosity. Because the nuclear reactions in the envelope produce most of the luminosity, for the purpose of finding out whether supergiant models can exist and determining their overall features, it is enough to describe this envelope and to approximate it as nonaccreting.

The connection of the envelope to a several-meter-thick isothermal halo below it and then onto the degenerate neutron region was done well in TŻ and in Eich *et al.* (1989) and is independent of the manner in which L_r turns off, so these issues will not be explored here. Instead, we shall focus on the issue where TŻ was defective: the details of the nuclear burning region and its connection to the convective envelope above it.

2.2. General strategy

The above discussion suggests dividing the problem of constructing a model into two parts which largely decouple: the physical structure and the nuclear-abundance structure. The former consists of density, temperature, internal energy, convective velocity, and mass inside a shell as functions of radius; these are governed by the stellar structure equations. The latter consists of the nuclear abundances as functions of radius; these are governed by a set of diffusion equations and appropriate boundary conditions given in part by nuclear reaction equations. These two parts almost decouple because the stellar structure equations make almost no reference to the details of nuclear abundances. (There is

some coupling due to the way the nuclear reactions affect the distribution of luminosity production. This is treated in §6. There is also a slight coupling because the opacity and the equation of state depend somewhat on composition.)

We will see in the next section that, from the stellar structure equations and an idealization that all energy generation occurs at the envelope's base, it is possible to construct a one-parameter family of envelopes each with the same total mass, core mass, and photospheric abundances, but differing from the others in its assumed photospheric luminosity. For each choice of photospheric luminosity we get a definite physical structure for the envelope, and from this we can determine the radial distribution of nuclear abundances. From the distribution of abundances we can determine how quickly the various nuclear species are diffusing into the burning region at the envelope's base to be burned. The luminosity resulting from this burning we will call the nuclear luminosity. The envelope for which the photospheric luminosity and the nuclear luminosity agree is a viable model. This is the basic strategy used to construct models in §§3 and 4.

3. Physical structure

3.1. Assumptions and theory

The envelope (i. e., the tenuous, nondegenerate, convective region above the edge of the core) was built by integrating the stellar structure equations using GOB, a computer program described by Paczyński (1969), which calculates static, Newtonian stellar envelopes with extended atmospheres. After we set a total mass M and photospheric abundances X_{ph} , Y_{ph} , Z_{ph} (mass fractions of hydrogen, helium, and all heavier elements, respectively), GOB allows two degrees of freedom: the photospheric luminosity L_{ph} and the photospheric temperature T_{ph} . One constraint is that we want a $1 M_{\odot}$ compact object for the core within a radius of 10 km. (Here we assume that the edge of the core lies at about 10 km.) This constraint reduces the two free parameters L_{ph} , T_{ph} to one, giving us the one-parameter family of envelopes discussed in the previous section. We assume (for now) that the local luminosity is constant all the way down to near the neutron star surface, that is, that all the luminosity is produced at the edge of the core.

Because the densities and temperatures near the core turn out to be on the order of 10^4 g cm^{-3} and $2 \times 10^9 \text{ K}$, it was necessary to modify GOB to take into account production of electron-positron pairs. This was done using the theory from Chapter 24 of Cox and Giuli (1968). Briefly, ρ and T were used to find a degeneracy parameter η by a table lookup (see Fig. 24.6 of Cox and Giuli 1968). Phase-space integrals were then performed at each integration step in GOB to find pressure, internal energy, and their derivatives with respect to η and T , and a change of variables was made back to ρ and T . Pains were taken to cope with numerical errors, so that the final derivatives were accurate to better than 5% near the tricky regime where pairs turn on and to better than 1% in all other regimes. Pressures and internal energies were accurate to better than 1% in all regimes. This procedure assumes that the envelope is everywhere in local thermodynamic equilibrium. This assumption turns out to be reasonable, since the longest time scales for pair production to occur are of order of 0.001 s in this model, while the time scale for turnover of convection cells is of order of 0.1 s or longer. GOB was also modified, in the manner described by TŻ, to take account of relativistic corrections to opacity.

In integrating the stellar structure equations, about 500 to 1000 steps were taken from the photosphere to the core, with a higher concentration taken at the largest and smallest radii.

3.2. Results

Table 1 gives details of several envelopes with total mass $M = 16 M_{\odot}$ and core mass $M_{\text{core}} = 1 M_{\odot}$.

In this table L_{ph} is the photospheric luminosity input into GOB, T_{ph} is the photospheric temperature, defined as the temperature of the envelope where optical depth is 0.667. The density ρ_0 and temperature T_0 are given at $r_0 = 10 \text{ km}$, i. e., at the edge of the core. The time scale for turnover of the largest turbulent eddies at r_0 is t_{turb} (defined as $v_{\text{turb}}/l_{\text{pres}}$, the ratio of the average turbulent velocity, as computed from the mixing length formalism for convection, to the pressure scale height). The ratio n_+/n_e is the ratio at r_0 of positron density to

TABLE 1

Physical Data for Various Envelopes^a

$L_{\text{ph}}(L_{\odot})$	$T_{\text{ph}}(\text{K})$	$\rho_0(\text{g cm}^{-3})$	$T_0(10^9\text{K})$	$t_{\text{turb}}(\text{s})$	n_+/n_e	$L_0^{\text{crit}}(L_{\odot})$
86000	3030.40	2.58×10^5	6.026	0.14	20.	12300
87000	3031.80	7.00×10^4	4.408	0.09	25.	6900
87500	3032.56	3.02×10^4	3.619	0.07	28.	5000
88000	3033.33	1.23×10^4	2.948	0.05	29.	3800
88500	3034.10	3.98×10^3	2.291	0.03	31.	2900
88600	3034.24	2.79×10^3	2.120	0.03	31.	2700
89000	3034.80	7.59×10^2	1.605	0.02	29.	2600
89500	3035.64	1.06×10^2	1.052	0.01	12.	4000

^a The envelopes correspond to a star with $M = 16 M_{\odot}$ and $M_{\text{core}} = 1 M_{\odot}$.

the density of ionization electrons. The last column contains the value L_0^{crit} of L^{crit} at r_0 . Table 1A shows some details of the internal structure of the envelope with $L = 88,600 L_{\odot}$ (the envelope which will produce the viable model in §5). Figure 2 shows a graph of T versus ρ for envelopes with $L = 88,600 L_{\odot}$ and $L = 86,000 L_{\odot}$.

Figure 3 shows the locus of points in the $(L_{\text{ph}}, T_{\text{ph}})$ -plane which satisfy the constraint that the core be $1 M_{\odot}$. The parameter Z will be explained in the last paragraph of §4. We note (Table 1A) that the maximum sound speed is given approximately by $v_s \approx (\frac{4}{3}P/\rho)^{1/2} \approx 6.1 \times 10^9 \text{ cm s}^{-1} \approx 0.2c$ near the surface of the core, where $P \approx \frac{1}{3}aT^4$. Also, the maximum of v_{turb}/v_s occurs near $r = 1.226 \times 10^{12} \text{ cm}$, so that we may estimate this ratio as 0.23. A more precise calculation gives the maximum $v_{\text{turb}}/v_s = 0.18$. These values are large enough to be disturbing, but not so large as to invalidate this approximate model.

4. Nuclear-abundance structure—first model

4.1. Assumptions and theory

From the physical structure we know how ρ , v_{turb} , and l_{pres} vary with r for

TABLE 1A

Physical Structure of one Envelope^a

$r(\text{cm})$	ρ (g cm^{-3})	v_{turb} (cm s^{-1})	l_{pres}/r	t_{turb} (s)	$T(\text{K})$	n_+/n_e	L_r^{crit} (L_{\odot})
1.004(6)	2.74(3)	8.04(6)	0.218	2.7(-2)	2.11(9)	3.42(1)	2.74(3)
1.134(6)	1.78(3)	8.56(6)	0.218	2.9(-2)	1.87(9)	2.93(1)	2.92(3)
1.279(6)	1.15(3)	9.14(6)	0.219	3.1(-2)	1.66(9)	2.42(1)	3.24(3)
1.444(6)	7.38(2)	9.78(6)	0.222	3.3(-2)	1.48(9)	1.90(1)	3.76(3)
1.663(6)	4.42(2)	1.06(7)	0.227	3.6(-2)	1.28(9)	1.34(1)	4.83(3)
1.916(6)	2.67(2)	1.14(7)	0.234	3.9(-2)	1.12(9)	8.35(0)	6.85(3)
2.209(6)	1.64(2)	1.21(7)	0.241	4.4(-2)	9.71(8)	4.57(0)	1.09(4)
2.548(6)	1.03(2)	1.25(7)	0.247	5.0(-2)	8.45(8)	2.03(0)	1.96(4)
2.879(6)	6.99(1)	1.22(7)	0.251	5.9(-2)	7.49(8)	7.39(-1)	3.36(4)
3.320(6)	4.53(1)	1.02(7)	0.254	8.3(-2)	6.52(8)	1.68(-1)	6.13(4)
3.829(6)	2.97(1)	6.74(6)	0.255	1.4(-1)	5.66(8)	1.72(-2)	8.16(4)
4.417(6)	1.95(1)	7.94(6)	0.255	1.4(-1)	4.92(8)	1.30(-3)	7.86(4)
5.096(6)	1.28(1)	9.47(6)	0.250	1.4(-1)	4.28(8)	5.06(-5)	7.38(4)
5.882(6)	8.42(0)	1.08(7)	0.256	1.4(-1)	3.72(8)	1.15(-6)	6.93(4)
6.791(6)	5.53(0)	1.20(7)	0.257	1.5(-1)	3.23(8)	1.40(-8)	6.53(4)
7.845(6)	3.64(0)	1.32(7)	0.258	1.5(-1)	2.81(8)	0.	6.18(4)
1.347(7)	7.64(-1)	1.71(7)	0.257	2.1(-1)	1.67(8)	0.	5.22(4)
3.176(7)	6.96(-2)	2.29(7)	0.274	3.8(-1)	7.48(7)	0.	4.46(4)
7.930(7)	6.40(-3)	2.83(7)	0.298	8.4(-1)	3.35(7)	0.	4.12(4)
2.210(8)	6.14(-4)	3.15(7)	0.341	2.4(0)	1.49(7)	0.	3.95(4)
7.444(8)	6.60(-5)	2.97(7)	0.408	1.0(1)	6.59(6)	0.	3.88(4)
3.291(9)	8.90(-6)	2.16(7)	0.495	7.5(1)	2.88(6)	0.	3.81(4)
1.964(10)	1.63(-6)	1.17(7)	0.578	9.7(2)	1.25(6)	0.	3.74(4)
1.487(11)	4.06(-7)	4.92(6)	0.650	2.0(4)	5.35(5)	0.	3.54(4)
1.226(12)	1.38(-7)	1.88(6)	0.743	4.8(5)	2.28(5)	0.	2.39(4)
1.005(13)	5.81(-8)	6.80(5)	1.215	1.8(7)	1.02(5)	0.	9.92(3)
4.860(13)	2.02(-8)	3.34(5)	0.311	4.5(7)	4.82(4)	0.	1.51(4)
6.801(13)	9.07(-9)	3.74(5)	0.106	1.9(7)	2.20(4)	0.	1.20(4)
7.607(13)	4.92(-9)	2.66(5)	0.030	8.7(6)	9.97(3)	0.	7.39(3)
7.722(13)	6.76(-9)	6.80(3)	0.011	1.2(8)	4.57(3)	0.	3.55(7)

^a The envelope corresponds to a star with $M = 16 M_{\odot}$, $M_{\text{core}} = 1 M_{\odot}$, and $L_{\text{ph}} = 88,600 L_{\odot}$.

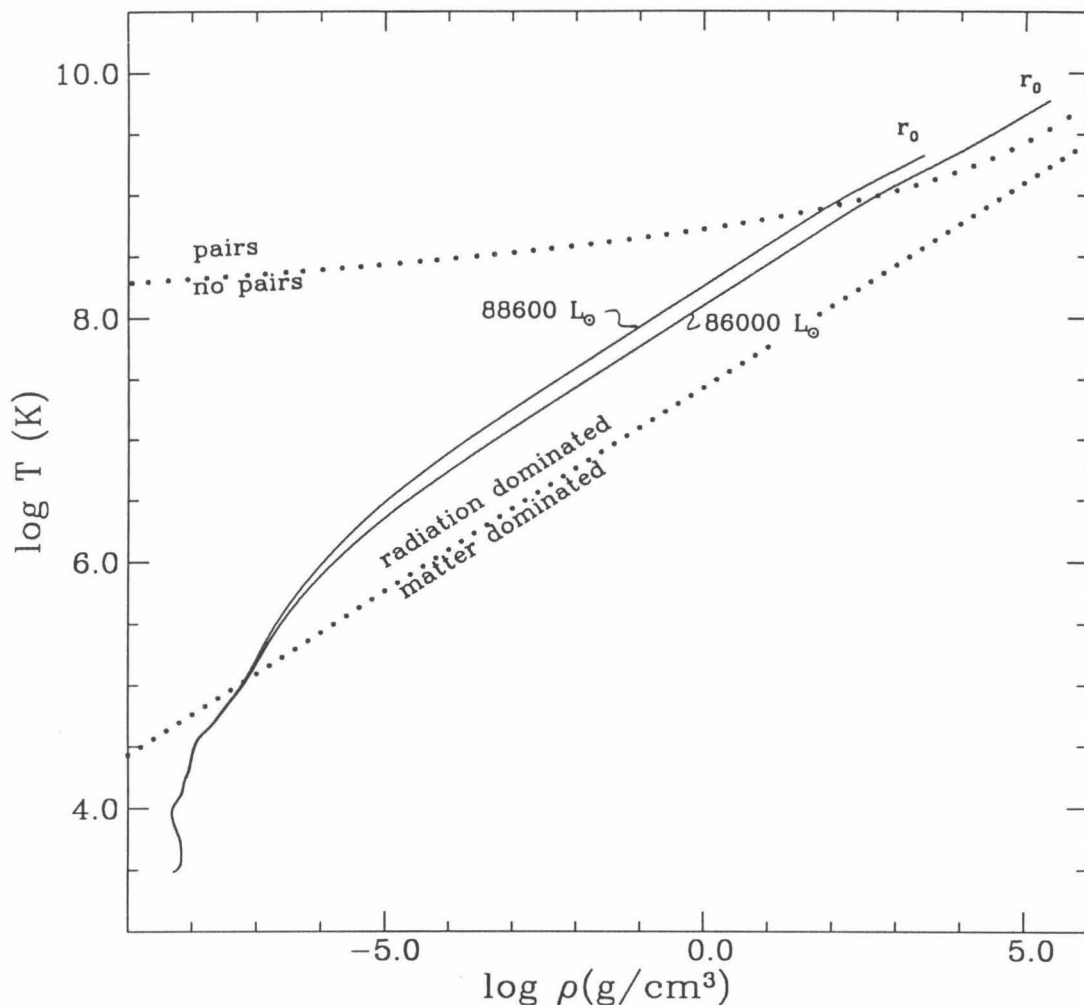


Fig. 2—Temperature versus density plotted (solid line) for the interiors of two candidate envelopes corresponding to total mass $16 M_{\odot}$, core mass $1 M_{\odot}$, photospheric abundances $X_{\text{ph}} = 0.7$, $Y_{\text{ph}} = 0.28$, $Z_{\text{ph}} = 0.02$ and to photospheric luminosities $86,000 L_{\odot}$ and $88,600 L_{\odot}$, respectively. The terminus at the lower left corner corresponds to the photosphere, i.e., where optical depth $\tau = \frac{2}{3}$, while the terminus at the upper right corner corresponds to the base of the envelope (radius $r_0 = 10 \text{ km}$), where local luminosity becomes subcritical and convection ceases. The upper dotted line shows where the density of positrons is equal to the density of ionization electrons (see the Appendix of TŻ for its calculation), and the lower dotted line shows where the radiation pressure and gas pressure are equal.

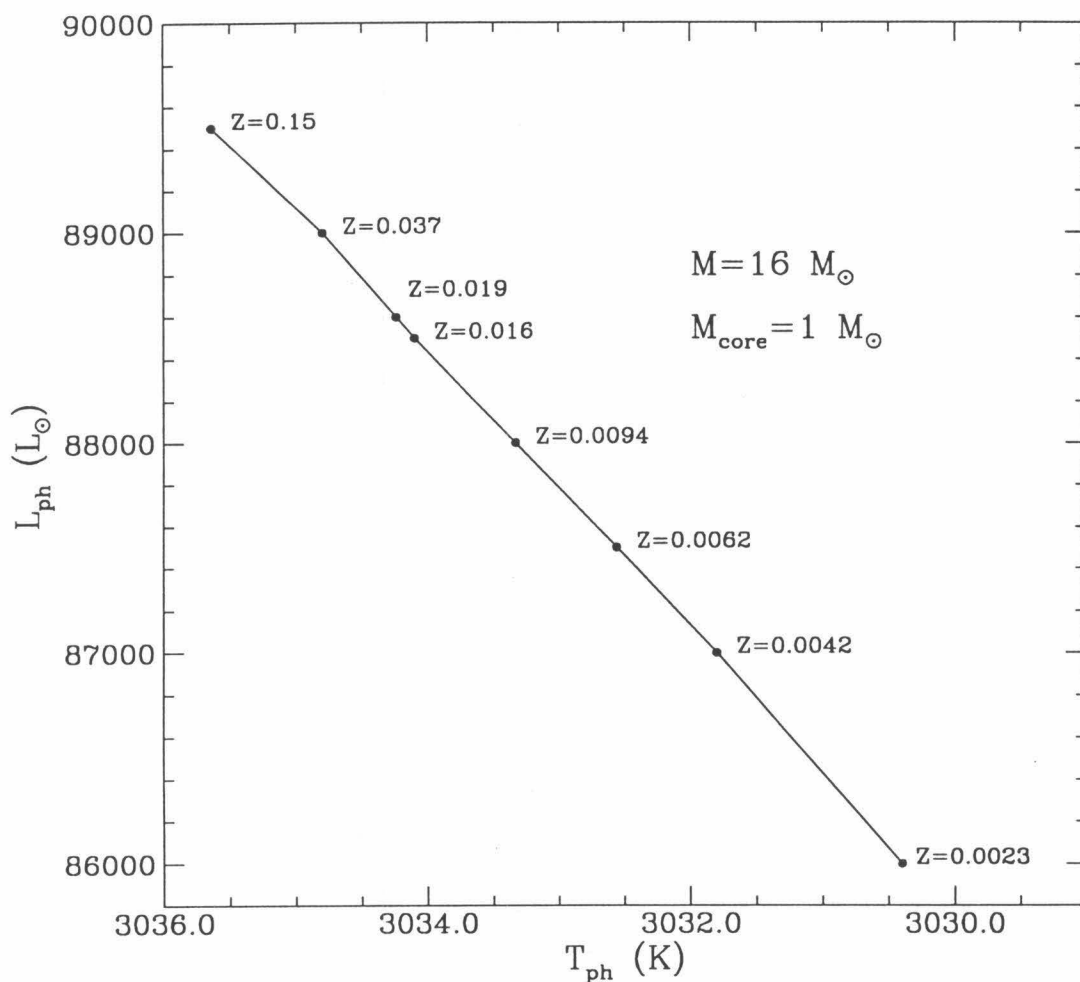


Fig. 3—Photospheric luminosity versus photospheric temperature shown for the one-parameter family of envelopes that have a $1 M_{\odot}$ compact core. The “consistent model” of §4 corresponds to a point parameterized by $Z = 0.02$. If we imagine photospheric metallicity Z to be a parameter, then the curve is parameterized by Z , the photospheric metallicity for which the envelope corresponds to a consistent model. The details are given in §4.

several trial envelopes. The task is to determine how the various Y_i vary with r , where Y_i is the abundance (in moles g^{-1}) of a nuclear species i . To solve for Y_i we will use an approximation investigated by Despain (1976), which is based on the mixing length theory of diffusion. Thus we say that Y_i satisfies a modified diffusion equation:

$$0 = \frac{\partial Y_i}{\partial t} = \frac{1}{\rho r^2} \frac{\partial}{\partial r} \left(r^2 \rho D \frac{\partial Y_i}{\partial r} \right) - \beta_i Y_i + \beta_j Y_j. \quad (4)$$

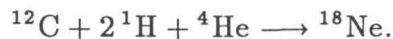
Here we are assuming that species j decays via beta decay into species i with time constant β_j and that species i decays with time constant β_i . The variable D is a generalized diffusion coefficient which is set to $v_{\text{turb}} l_{\text{pres}}$ and thus is a function of r . (Hence we are setting the mixing length to one pressure scale height. Models with a different ratio of mixing length to scale height did not produce qualitatively different results.) By making this approximation we are introducing modest errors, since the turbulent turnover time scale will often be on the order of the strong reaction time scales. Note also that this analysis assumes that beta decays may occur anywhere in the envelope.

Equation (4), with i running over the various species, is a set of coupled ordinary differential equations which the Y_i must satisfy. We must augment these equations by boundary conditions. We will assume that at the surface of the star the nuclear abundances have the standard Population I values, except that we will simplify the analysis by lumping all the "metals" (^{12}C , ^{14}N , ^{16}O , and other elements with $A > 12$) into ^{12}C , again introducing modest errors. Thus, we have

$$\begin{aligned} Y_{\text{H}}(r_{\text{ph}}) &= 0.7000, & Y_{\text{He}}(r_{\text{ph}}) &= 0.0700 \\ Y_{^{12}\text{C}}(r_{\text{ph}}) &= 0.0017, & Y_i(r_{\text{ph}}) &= 0.0000 \quad \text{otherwise.} \end{aligned} \quad (5)$$

(Multiply by atomic weight to convert these abundances to mass fractions.)

For the models of this section, we will assume that the strong reactions occur only at r_0 , that is, at the edge of the core, and that they go to completion. An example will illustrate the translation of this assumption into boundary conditions. Consider the strong reaction which starts off the rp-process:



The nucleus ^{18}Ne cannot be burned but must wait for a beta decay. For the boundary conditions we have

$$Y_{^{12}\text{C}}(r_0) = 0, \quad (6)$$

$$4\pi r_0^2 \rho D \frac{dY_{^{12}\text{C}}(r_0)}{dr} = -4\pi r_0^2 \rho D \frac{dY_{^{18}\text{Ne}}(r_0)}{dr}.$$

The former equation expresses the idea that ^{12}C is completely burned at the edge of the core. The left-hand side of the latter equation is the flux of ^{12}C into the shell at radius r_0 in moles s^{-1} (see eq. [4]), and the right-hand side is the flux of ^{18}Ne out of this shell. Of course, this simplifies to

$$\frac{dY_{^{12}\text{C}}(r_0)}{dr} = -\frac{dY_{^{18}\text{Ne}}(r_0)}{dr}. \quad (7)$$

In the two reaction networks (hot CNO and rp), each species i considered was either the product or the reactant of a strong reaction, and so equations (6) and (7) are prototypes for all the boundary conditions we shall meet.

In the hot CNO cycle, ^{12}C is a catalyst for the reaction



which provides about 21 MeV per cycle. The limiting reaction is the decay of ^{15}O which takes 176 seconds (mean lifetime).

In the rp-process (Wallace and Woosley 1981), a ^{12}C nucleus is used as a "seed" for a reaction chain summarized by



which produces about 500 MeV per seed nucleus. The burning region of our star looks approximately like this: A seed nucleus is swept into the burning region, burned (mainly by dripping on protons) to a proton-rich species, and swept back out into the envelope. It random walks around awaiting beta decay, decays, and then random walks back to the burning region, where protons are dripped on to form another proton-rich species. This continues until heavy nuclei are built up. Instead of following all the isotopes in the rp-process, we shall identify a smaller

number of species i , such that finding Y_i as a function of r gives us a good idea of the physics in the star. We note that in Zimmermann's analysis the problem was that the burning region became clogged with long-lived beta-unstable species which could not undergo any further strong reactions. For us also, the main question will be, how badly do the incomplete beta decays hinder the rp-process? To answer this question, we must track the following nuclear species: ^{12}C (which is the initial seed), the long-lived beta-unstable species, and their decay products.

For the hot CNO cycle the chosen species (see §3 of the Appendix) are ^{12}C , ^{15}O , and the daughter of ^{15}O : ^{15}N . Our chemical structure thus consists of $Y_{^{12}\text{C}}$, $Y_{^{15}\text{O}}$, and $Y_{^{15}\text{N}}$ as functions of r . The simplified reactions are given in Table 1B. The first and third reactions (being strong reactions or fast beta decays) occur very quickly at r_0 , and the second (being a long beta decay) occurs throughout the envelope. The second column, E_{rxn} , is given by the mass difference of the nuclides. The third column gives the total energy released in beta decays, and the fourth column gives the approximate heat energy made available to the envelope. We assume that about half the beta decay energy is lost to neutrinos, so that $E_{\text{heat}} = E_{\text{rxn}} - \frac{1}{2}E_{\beta}$. The boundary conditions, deduced in accord with the prototypes (6) and (7) above, become

$$Y_{^{12}\text{C}}(r_0) = 0, \quad (8a)$$

$$Y_{^{15}\text{N}}(r_0) = 0, \quad (8b)$$

$$-Y'_{^{15}\text{O}}(r_0) = Y'_{^{12}\text{C}}(r_0) + Y'_{^{15}\text{N}}(r_0). \quad (8c)$$

The first two equations express the idea that ^{15}N and ^{12}C are burned at r_0 ; and the third, that the flux of reactants into the shell of radius r_0 is equal to the flux of products out.

The Appendix (§§1 and 2) gives full details as to why certain species were chosen for the rp-process network. These species are those in the third and fourth columns of Table 2, plus ^{12}C ; and our nuclear-abundance structure consists of their Y_i . Shown in column 2 is the reaction at the core edge which produces the parent. For each of the long-lived beta decays that we track, the mean life of the

TABLE 1B

Simplified hot CNO Cycle			
reaction	E_{rxn} (MeV)	E_{β} (MeV)	E_{heat} (MeV)
$^{12}\text{C} + 3\text{}^1\text{H} \longrightarrow ^{15}\text{O} + e^+ + \nu$	17.848	4.45	15.6
$^{15}\text{O} \longrightarrow ^{15}\text{N} + e^+ + \nu$	1.620	1.620	0.8
$^{15}\text{N} + \text{}^1\text{H} \longrightarrow ^{12}\text{C} + \text{}^4\text{He}$	4.966	0.000	5.0

parent species is given by the τ in column 5. In column 6 is shown the total energy of this reaction, plus the beta decay energy released when the parent decays into the daughter, plus the energy released by the annihilation of positrons. Column 7 gives the total energy due to all the beta decays in the reaction in column 2 and the decay of the species in column 3. Column 8 is the total heat energy available to the envelope once the reaction in column 2 and the subsequent beta decay have occurred. Again we assume that about half of the beta-decay energy is lost to neutrinos, so that $E_{\text{heat}} = E_{\text{rxn}} - \frac{1}{2}E_{\beta}$.

The boundary conditions on the rp-process abundances, deduced in accord with the prototypes (6) and (7), are

$$Y_{12\text{C}}(r_0) = 0, \quad (9a)$$

$$Y'_{18\text{Ne}}(r_0) = -Y'_{12\text{C}}(r_0), \quad (9b)$$

$$Y_D(r_0) = 0, \quad (9c)$$

$$Y'_{\text{P},k+1}(r_0) = -Y'_{\text{D},k}(r_0), \quad (9d)$$

where P and D refer to parent and daughter species in Table 2.

Once we have solved the set of coupled equations represented by equation (4) subject to the boundary conditions (8) or (9), we can then calculate the luminosity produced by the nuclear burning, L_{nuc} , as follows: Assume k is a species, that is, either ^{12}C or a beta decay daughter, which is burned at the edge of the core

TABLE 2

Data for Simplified rp-Process

k	reaction	parent	daughter	τ (s)	E_{rxn} (MeV)	E_{β} (MeV)	E_{heat} (MeV)
1	$^{12}\text{C} + 2\ ^1\text{H} +\ ^4\text{He} \longrightarrow\ ^{18}\text{Ne}$	^{18}Ne	^{18}F	2.41	16.131	4.447	14.0
2	$^{18}\text{F} + 4\ ^1\text{H} \longrightarrow\ ^{22}\text{Mg} + e^+ + \nu$	^{22}Mg	^{22}Na	5.57	35.210	17.888	26.3
3	$^{22}\text{Na} + 4\ ^1\text{H} \longrightarrow\ ^{26}\text{Si} + e^+ + \nu$	^{26}Si	^{26}Al	3.17	36.185	17.805	27.3
4	$^{26}\text{Al} + 4\ ^1\text{H} \longrightarrow\ ^{30}\text{S} + e^+ + \nu$	^{30}S	^{30}P	1.70	37.145	19.934	27.2
5	$^{30}\text{P} + 38\ ^1\text{H} \longrightarrow\ ^{68}\text{Se} + 19e^+ + 19\nu$	^{68}Se	^{68}As	140	315.55	176	228
6	$^{68}\text{As} + 4\ ^1\text{H} \longrightarrow\ ^{72}\text{Kr} + e^+ + \nu$	^{72}Kr	^{72}Br	25.1	29.32	15.1	21.8
7	$^{72}\text{Br} + 5\ ^1\text{H} \longrightarrow\ ^{77}\text{Sr} + 2e^+ + 2\nu$	^{77}Sr	^{77}Rb	13	42.63	25.3	30
8	$^{77}\text{Rb} + 4\ ^1\text{H} \longrightarrow\ ^{81}\text{Zr} + e^+ + \nu$	^{81}Zr	^{81}Y	900	32.1	17	24
9	$^{81}\text{Y} +\ ^1\text{H} \longrightarrow\ ^{82}\text{Zr}$	^{82}Zr	^{82}Y	800	7.1	6	4
10	$^{82}\text{Y} + 4\ ^1\text{H} \longrightarrow\ ^{86}\text{Mo} + e^+ + \nu$	^{86}Mo	^{86}Nb	30	31.9	16	24
11	$^{86}\text{Nb} + 5\ ^1\text{H} \longrightarrow\ ^{91}\text{Ru} + 2e^+ + 2\nu$	^{91}Ru	^{91}Tc	30	40.7	25	48
12	$^{91}\text{Tc} + 5\ ^1\text{H} \longrightarrow\ ^{96}\text{Pd} + 2e^+ + 2\nu$	^{96}Pd	^{96}Rh	(end)	47.5	27	34

yielding energy $E_{\text{heat},k}$. Then L_{nuc} is given by

$$L_{\text{nuc}} = 4\pi r_0^2 \rho_0 D_0 \sum_k Y'_k(r_0) E_{\text{heat},k}, \quad (10)$$

where ρ_0 and D_0 are the values of ρ and D at r_0 . We recognize $4\pi r_0^2 \rho_0 D_0 Y'_k(r_0)$ as the flux of species k into the shell of radius r_0 , and $E_{\text{heat},k}$ is the energy in column 8 of Table 2. Since $E_{\text{heat},k}$ includes the heat released by the eventual beta decay, which actually occurs somewhere above r_0 , in equation (10) we are artificially putting that beta decay heat into the star at r_0 .

The solution of equations (4), (9), and (10) for the rp-process is presented in §4.3. Several ingredients are involved, which are discussed in §4.2.

4.2. Numerical methods

For the various parent species i , the diffusion equation (4) and boundary conditions (9) take the forms

$$\frac{1}{\rho r^2} (\rho r^2 D Y'_i)' - \beta_i Y_i = 0, \quad (11a)$$

$$Y_i(r_{\text{ph}}) = 0. \quad (11b)$$

We shall embody the solution of these homogeneous equations in the ratio

$$\eta_i = -Y'_i(r_0)/Y_i(r_0). \quad (11c)$$

We compute numerically the η_i for our various parent species by the standard technique of “shooting”: We first set $Y_i(r_0)$ to 1 and choose trial values of $Y'_i(r_0)$ until we satisfy equation (11b).

We also introduce a function $\Xi(r)$ (useful for ^{12}C and daughter species), defined as the solution to these equations:

$$\frac{1}{\rho r^2} (\rho r^2 D \Xi')' = 0,$$

$$\Xi(r_0) = 0, \quad (12a)$$

$$\Xi(r_{\text{ph}}) = 1.$$

The computation of $\Xi(r)$ is easily reduce to quadratures:

$$\Xi(r) = \frac{\int_{r_0}^r \frac{dr}{r^2 \rho D}}{\int_{r_0}^{r_{\text{ph}}} \frac{dr}{r^2 \rho D}}. \quad (12b)$$

In analogy to η_i defined above, we define

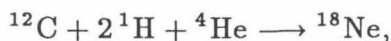
$$\eta_s = \Xi'(r_0). \quad (12c)$$

In §4.3, we will see that these ingredients (eqs. [11] and [12] and associated numerical calculations) are sufficient to determine all the abundances $Y_i(r)$ and from them L_{nuc} and hence to obtain a viable model.

4.3. Results

When this formalism was applied to the hot CNO network, no self-consistent model was found. More specifically, for all the envelopes we studied, each with a T_{ph} and L_{ph} along the curve in Figure 3, this formalism produced values of L_{nuc} far smaller than L_{ph} . The lowest values of T_{ph} and L_{ph} in Figure 3 produce envelopes with the lowest ρ_0 and T_0 at the edge of the core, and correspondingly the lowest $L_{\text{nuc}}/L_{\text{ph}}$. As T_{ph} and L_{ph} were raised, ρ_0 , T_0 , and $L_{\text{nuc}}/L_{\text{ph}}$ went up. Eventually, however, at $T_{\text{ph}} = 3034.80$ K and $L_{\text{ph}} = 89000 L_{\odot}$, ρ_0 and T_0 became so high (cf. Table 1) that the nuclear burning could easily break out of the hot CNO cycle and into the rp-process. At this point the hot CNO cycle produced its maximum luminosity, $L_{\text{nuc}}/L_{\text{ph}} = 0.07$. This is in accord with results obtained by Zimmermann (1979); see also Eich *et al.* (1989).

When the hot CNO cycle failed to produce enough luminosity, we turned attention to the rp-process. We might fear that for the rp-process the above formalism would produce a large number of hopelessly coupled equations. On the contrary, it turns out that the equations are easy to solve and interpret. Let us consider the first part of the rp chain:





cf. Table 2.

Consider first ${}^{12}\text{C}$, for which we must solve equation (4) with $\beta_i = \beta_j = 0$ subject to equations (5) and (9a). Clearly the solution is

$$Y_{12\text{C}}(r) = Y_T \Xi(r), \quad (13)$$

where Y_T is the molar concentration of ${}^{12}\text{C}$ at the surface of the star, i.e., 0.0017 moles g^{-1} . Figure 4 illustrates this function.

Consider next ${}^{18}\text{Ne}$, for which (because it is a beta decay parent) we must solve equation (11) with $Y'_{18\text{Ne}}$ given by equation (9b). By the method in §4.2, we find $\eta_{18} \equiv -Y'_{18\text{Ne}}(r_0)/Y_{18\text{Ne}}(r_0)$. The quantity $Y'_{18\text{Ne}}(r_0)$ is determined by the boundary condition (9b) and the solution for $Y_{12\text{C}}$ to be

$$Y'_{18\text{Ne}}(r_0) = -Y_T \eta_s.$$

From the definition of η_{18} we then obtain

$$Y_{18\text{Ne}}(r_0) = Y_T \frac{\eta_s}{\eta_{18}}. \quad (14)$$

We can obtain $Y_{18\text{Ne}}(r)$ at other radii r by multiplying the function Y_i (calculated as described in the first paragraph of §4.2) by the factor $Y_{18\text{Ne}}(r_0)$; however, our primary goal is to obtain L_{nuc} , for which we need only information at r_0 .

Next consider the sum

$$Y_{18}(r) = Y_{18\text{Ne}}(r) + Y_{18\text{F}}(r), \quad (15)$$

which satisfies

$$\frac{1}{\rho r^2} (\rho r^2 D Y'_{18})' = 0,$$

$$Y_{18}(r_0) = Y_{18\text{Ne}}(r_0) + Y_{18\text{F}}(r_0) = Y_{18\text{Ne}}(r_0),$$

$$Y_{18}(r_{\text{ph}}) = 0.$$

(Here $Y_{18\text{F}}(r_0) = 0$, just like $Y_{12\text{C}}(r_0) = 0$, because ^{18}F , like ^{12}C , is a reactant in a strong reaction.) Clearly, then, Y_{18} is given by

$$Y_{18}(r) = Y_{18\text{Ne}}(r_0)(1 - \Xi(r)), \quad (16)$$

from which we obtain the following, by differentiating and using equations (15) and (16):

$$Y'_{18\text{F}}(r_0) = Y_T \eta_s \zeta_{18\text{Ne}}, \quad (17)$$

where $\zeta_{18\text{Ne}} \equiv 1 - \eta_s/\eta_{18}$. Figure 5a shows $Y_{18\text{Ne}}$ and $Y_{18\text{F}}$ versus $\log r$. ($Y_{18\text{F}}$ is obtained by solving for it in eq. [15] and substituting eq. [16] into it.)

Let us pause to consider what we have done. Expression (10) for L_{nuc} uses $Y'_{12\text{C}}(r_0)$ and $Y'_{18\text{F}}(r_0)$. The former is given by $Y_T \eta_s$ and the latter by $Y_T \eta_s \zeta_{18\text{Ne}}$. The flux $4\pi r_0^2 \rho_0 D_0 Y'_{18\text{F}}(r_0)$ of ^{18}F into the burning region thus is the same as the flux of ^{12}C into the burning region $4\pi r_0^2 \rho_0 D_0 Y'_{12\text{C}}(r_0)$ multiplied by the easily calculable hindrance factor $\zeta_{18\text{Ne}} = 1 - \eta_s/\eta_{18}$, which depends on the mean time for ^{18}Ne to decay. This hindrance factor provides a good handle on the amount of “damage” done by a particular beta decay, since it gives the fraction of daughter species which make it back to the burning region to be burned. We similarly work our way down the chain. The next link (reaction 2 in Table 2, followed by its beta decay) yields

$$Y'_{22\text{Na}}(r_0) = Y_T \eta_s \zeta_{18\text{Ne}} \zeta_{22\text{Mg}},$$

where $\zeta_{22\text{Mg}} = 1 - \eta_s/\eta_{22}$. Similarly, the flux of any other daughter species into the burning region is the product of $Y_T \eta_s$ and all the hindrance factors for parent species which precede it in the chain. By a repetition of the above steps we can calculate all the hindrance factors, and from them all the quantities $Y'_D(r_0)$, and we can then substitute these into equation (10) to obtain L_{nuc} . The result is

$$L_{\text{nuc}} = 4\pi r_0^2 \rho_0 D_0 Y_T \eta_s \sum_{k=1} \left(E_{\text{heat},k} \prod_{i=0}^{k-1} \zeta_i \right), \quad (18)$$

where we set $\zeta_0 = 1$. Figure 5b shows $Y_{22\text{Mg}}$ and $Y_{22\text{Na}}$ versus $\log r$, and Figure 5c shows a parent and daughter much later in the chain: $Y_{81\text{Zr}}$ and $Y_{81\text{Y}}$ versus $\log r$.

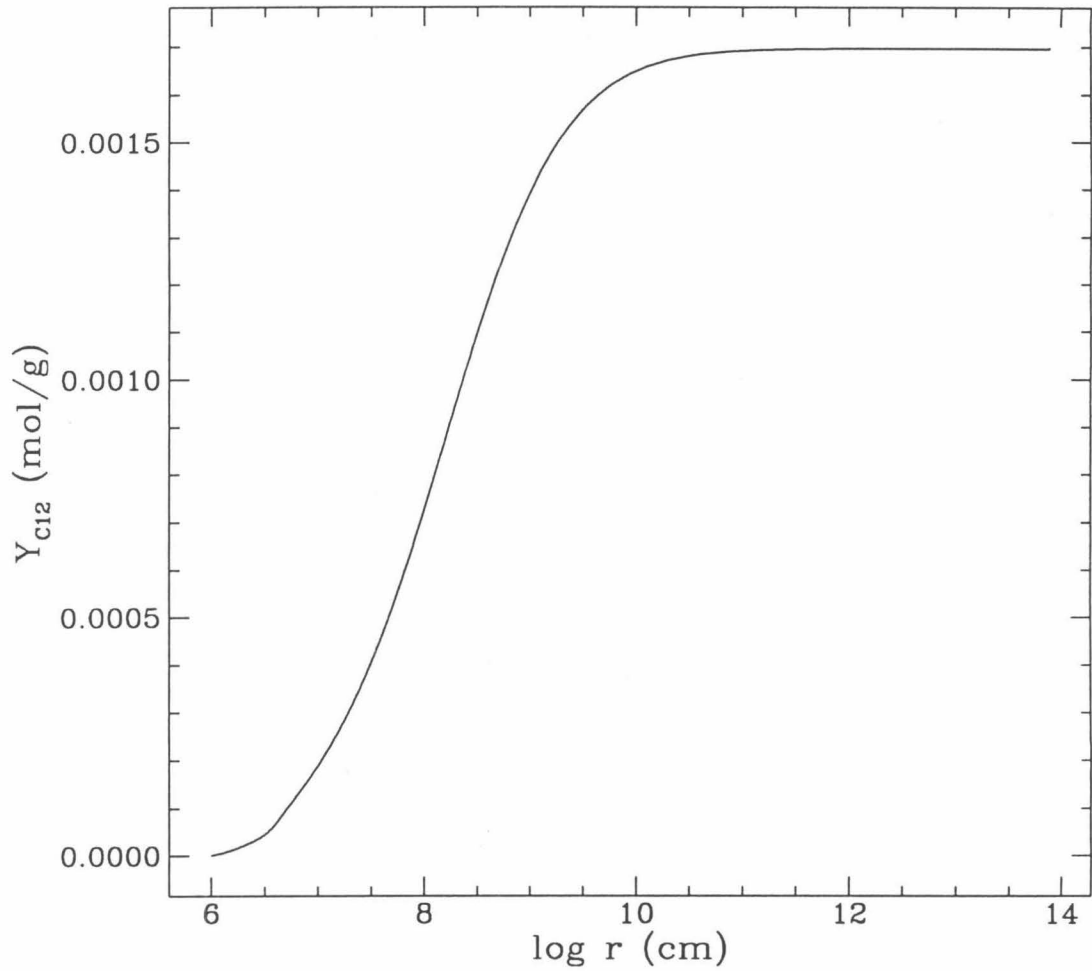


Fig. 4—The concentration of ^{12}C plotted as a function of r for a typical envelope. The nucleus ^{12}C is burned near the edge of the core ($r = r_0 = 10$ km), hence its zero concentration there. Near $r = 10^{10}$ cm the nucleus ^{12}C attains almost its Population I abundance. Thus most of the envelope has nearly the Population I abundance of ^{12}C .

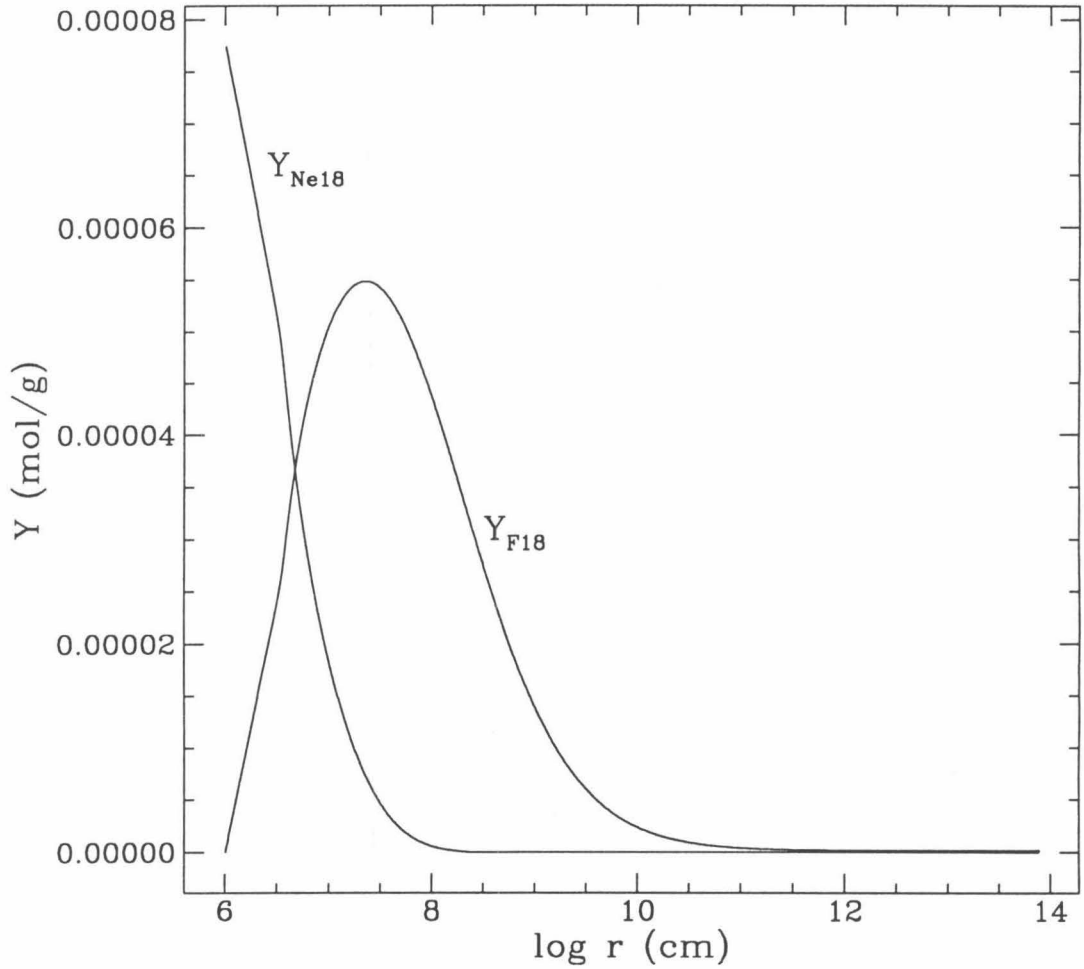


Fig. 5(a)—The concentrations of the nuclei ^{18}Ne (beta-decay parent) and ^{18}F (its daughter) shown as functions of r . The former is produced in the hot burning region near the core, while the latter is consumed there. Parents, having been produced near the edge of the core, random walk in the envelope until their decay and possible return to the burning region for further strong reactions. The nucleus ^{18}Ne has a mean lifetime of 2.41 s.

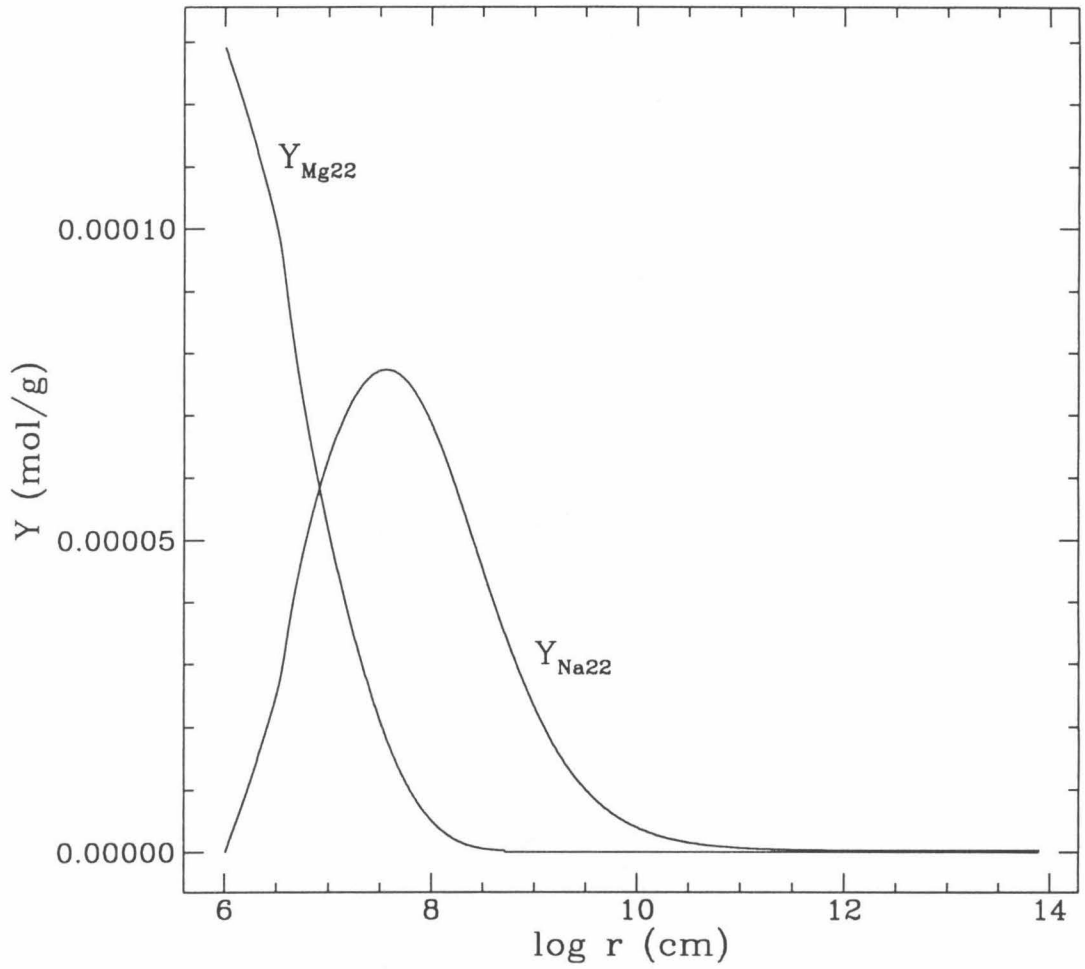


Fig. 5(b)—Concentrations of ^{22}Mg (parent) and ^{22}Na (daughter) as functions of r . The nucleus ^{22}Mg has a mean lifetime of 5.57 s.

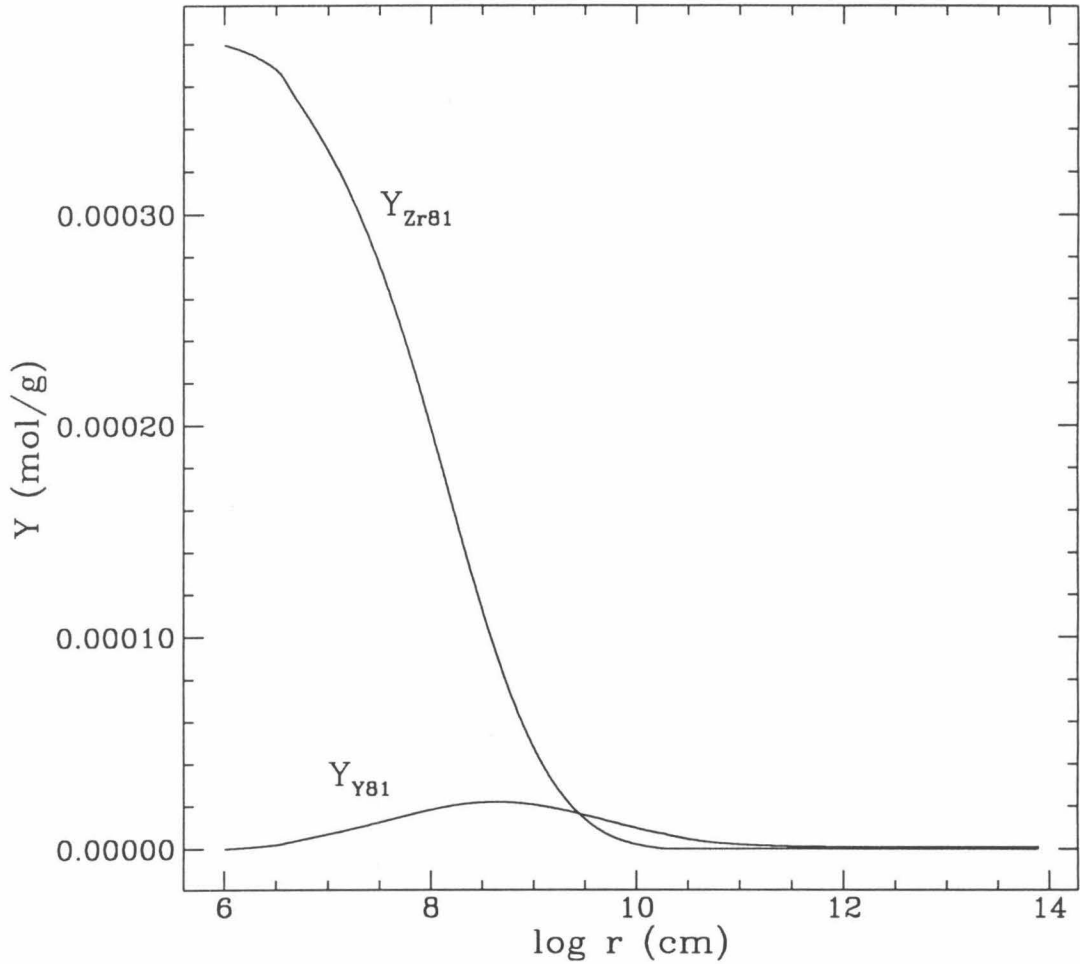


Fig. 5(c)—Concentrations of ^{81}Zr (parent) and ^{81}Y (daughter) as functions of r . The nucleus ^{81}Zr has a mean lifetime of 900 s, so that it random walks far into the envelope before its eventual decay, and little of the ^{81}Y makes it back to the burning region ($17.3\% \equiv \zeta_{s1\text{Zr}}$; cf. Table 3). Long decays such as this one tend to cut off the rp-process.

There is a similarity in shape among the three graphs of parents and daughters in Figure 5. Note, however, that Y_{SiY} is quite small and Y_{SiZr} is large at greater radii than the other parents, approximately $r = 10^9$ cm. An average turbulent turnover time in this region is 1 s, and the decay time for ^{81}Zr is 900 s. If we assume the ^{81}Zr random walks for 900 s, we would expect to find it $\sqrt{900 \text{ s}/1 \text{ s}} \approx 30$ random walk steps from its origin, that is, (noting that a pressure scale height is about $.25r$) at a radius $(10^6 \text{ cm})1.25^{30} \approx 10^9$ cm, in agreement with the figure.

In Table 3 we present the hindrance factors for the model envelope with $L = 88,600 L_{\odot}$ and $T_{\text{ph}} = 3034.24$ K. Notice that for parent species with decay time less than 6 s, the daughter species generally ($\sim 90\%$) make it back to the burning region where they are burned. For parent species with decay time greater than 20 s, the hindrance factor becomes more prohibitive (~ 0.5). When these quantities are used to calculate L_{nuc} for the envelopes in Table 1, we get the results in the first three columns of Table 4.

What can we conclude from this analysis? *First*, we can be assured that we can find a viable model. For the last five envelopes in Table 4 (those envelopes which do not have dangerously high temperatures at r_0 (see the Appendix)) $L_{\text{nuc}}/L_{\text{ph}}$ ranges from 0.14 to 1.97, which guarantees an envelope which is consistent, i.e., for which $L_{\text{nuc}}/L_{\text{ph}} = 1$, even if we were to include all the beta decays and correct the systematic errors (effects of about 10%) that we have made in this analysis. We will be taking a closer look at the envelope with $L = 88,600 L_{\odot}$ in the subsequent section, since it is the one lying closest to $L_{\text{nuc}}/L_{\text{ph}} = 1$. *Second*, we note (see eq. [18]) that the expression for L_{nuc} is proportional to Y_T . This means that if we were to change the value of Y_T , we could go to Table 4 and easily point to the envelope which would yield a model. (Recall that $Y_T = Z/12$.) The last column of Table 4 tabulates this quantity as Z_{req} (i.e., the photospheric metallicity required to have a consistent model). In Figure 3 each envelope is labeled with the value of Z (photospheric metallicity) for which it is a viable model, Z is calculated as $0.02L_{\text{ph}}/L_{\text{nuc}}$. *Third*, we note that beta decays on the order of seconds, such as at the beginning of the rp-process, do little to hinder the rp-

TABLE 3

Nuclear-Abundance Results for an Envelope^a

species	τ (s)	$r_0\eta$	ζ^b
¹⁸ Ne	2.41	0.2744	0.954
²² Mg	5.57	0.1571	0.920
²⁶ Si	3.17	0.2285	0.945
³⁰ S	1.70	0.3464	0.964
⁶⁸ Se	140	0.0247	0.494
⁷² Kr	25.1	0.0600	0.792
⁷⁷ Sr	13	0.0904	0.862
⁸¹ Zr	900	0.0151	0.173
⁸² Zr	800	0.0154	0.187
⁸⁶ Mo	30	0.0593	0.684
⁹¹ Ru	30	0.0539	0.684

^a The envelope corresponds to a star with $M = 16 M_\odot$, $M_{\text{core}} = 1 M_\odot$, and $L_{\text{ph}} = 88,600 L_\odot$.

^b The quantity ζ is the fraction of fuel returning after the given beta decay. It is called the “hindrance factor” in the text and determines the nuclear burning luminosity L_{nuc} through equation (18).

process, while decays on the order of tens of seconds begin to choke it off. It thus makes sense to say that the rp-process is pushed not to ¹²⁰Ba, as we would surmise if the rp-process were limited by proton addition (see §2 of the Appendix), but stops at about ⁶⁸Se because of several long beta decays. (However, see Chapter 4 of this thesis.)

TABLE 4

Nuclear-Abundance Data for Various Envelopes^a

$L_{\text{ph}}(L_{\odot})$	$r_0\eta_s$	$L_{\text{nuc}}/L_{\text{ph}}^{\text{b}}$	$Z_{\text{req}}^{\text{c}}$
86000	0.00312	8.46	0.0021
87000	0.00450	4.59	0.0038
87500	0.00579	3.05	0.0058
88000	0.00774	1.97	0.0089
88500	0.0112	1.11	0.016
88600	0.0125	0.92	0.019
89000	0.0109	0.46	0.038
89500	0.0322	0.14	0.133

^a These envelopes correspond to a star with $M = 16 M_{\odot}$ and $M_{\text{core}} = 1 M_{\odot}$.

^b A viable model is one for which this parameter is 1 (for metallicity $Z = 0.02$).

^c This is the “required surface metallicity” for which the envelope is a viable model, if we think of letting the surface metallicity Z be a parameter.

5. Nuclear-abundance structure—second model

5.1. Assumptions and theory

In §4 we assumed that all of the strong reactions occurred at r_0 and all the energy generation occurred at r_0 , whereas in fact the beta decay energy is deposited throughout a large portion of the envelope and the energy of strong reactions is deposited throughout the first several pressure scale heights of the envelope (\sim several km). In this section we will address this flaw of §4 by creating a model in which the energy is deposited at four specific radii and by then interpolating the local luminosity as a function of radius. We would like to be assured that indeed the local luminosity does exceed the critical luminosity for all $r > r_0$. If this is

so, then it is not important to know exactly how the local luminosity depends on radius, for the structure of the envelope is not much affected by changes in luminosity. If this turns out at any radius not to be so, then the model is necessarily inconsistent, since this condition is necessary to maintain convection, and we have assumed all along that convection is the main mechanism for heat and material transport. This is the motivation for this section. The cost of this “more nearly complete” analysis is that we will no longer track individually the various beta-unstable parents as in §4, having been assured that these decays do not cut off the rp-process.

Although energy is deposited throughout the lower portion of the envelope, we will approximate this by placing the nuclear burning at the four discrete radii r_0 , r_1 , r_2 , and r_3 . We take r_0 to be the edge of the core. We let r_1 be the radius at which “breakout” from the hot CNO cycle is likely to occur, that is, the radius at which the time required for $^{15}\text{O} + ^4\text{He} \rightarrow ^{19}\text{Ne} + \gamma$ (the reaction that breaks out of the CNO cycle) is about the same as the turbulent turnover time. We let r_3 be the radius at which the critical luminosity attains a local maximum, and r_2 we arbitrarily choose to be the geometric mean of r_1 and r_3 .

The first several kilometers of the envelope, which comprise the burning region, consist of a complex, turbulent mixture of nuclei, resembling a kind of nuclear soup of proton-rich nuclei, with turbulent turnover, beta decays, and strong reactions all occurring on about the same time scales, about 0.1 to 10 s. How shall we idealize this situation in order to obtain a tractable model? First, let us picture a situation in which breakout from the hot CNO cycle is facile and beta decays are immediate, so that the limiting reactions are the proton additions. In this situation a seed nucleus random walks from the outer envelope inward, and as it reaches hotter, denser portions of the envelope, it becomes easier for protons to overcome the Coulomb barrier and build up heavier nuclei. Energy is released throughout the proton addition region.

Next, let us turn on the shorter beta decays, those less than, say, 1.5 s. (See Fig. 7.) This does not change the picture very much, since a nucleus Nu_1 is about

as likely to random walk from r_0 to r_1 before decay and further proton addition as it is likely to random walk from r_1 to r_0 before decay and proton addition. Thus the distribution of luminosity production is not much changed from the scenario we had in the previous paragraph, except that it is smeared over a slightly larger region and the rp-process is slightly less efficient (since, with several seconds of cumulative beta decay time, some of the seed escapes).

Next, let us turn on the longer beta decays, greater than 10 s, which occur later in the chain, that is, ^{68}Se and beyond. As noted in the last paragraph of §4, these tend to carry the seed nuclei out of the burning region and into the envelope, whence they do not return. Thus the hotter, denser regions of the envelope do not push the seed nuclei as far along the rp chain as we surmised when we were considering proton addition as the limiting process. The result is a decrease of the amount of energy produced near the edge of the core.

Finally, let us consider the beginning of the rp-process in more detail. (See §1 of the Appendix.) The first step, breakout from the hot CNO cycle, is not facile but occurs only when ^4He can overcome the Coulomb barrier in being added to ^{15}O . This happens deep in the burning region at r_1 . The product quickly burns to ^{21}Mg , decays, and burns to ^{22}Mg , which, after a longer decay of 5.57 s, becomes ^{22}Na . This decay distributes the species ^{22}Na throughout the burning region. As the rp-process proceeds, the longer decays of ^{26}Si (3.17 s) and ^{30}S (1.70 s) further distribute seed nuclei throughout the burning region. Adding these details alters somewhat the distribution of luminosity production in the previous paragraph.

To summarize thus far, in creating a model in this section, we will be guided by several principles: (1) Proton addition (in the rp-process) does not proceed as far in cooler portions of the envelope as it does in hotter portions. (2) The rp-process generally stops at ^{68}Se because of long beta decays. (3) Long-lived beta-decay parents random walk to large radii and deposit energy there (energy both from beta decay and from the subsequent proton addition which can occur in the region of the beta decay).

Considering the first two principles, in §2 of the Appendix we discuss to what

extent proton addition pushes the rp-process at our four radii r_n . At each r_n the reaction network looks like Figure 7 (see the Appendix), except that at r_3 burning proceeds only to ^{35}Cl and at r_2 burning proceeds only to ^{49}Ti , in accordance with the first principle above. At r_0 and r_1 the burning would proceed very far (to ^{120}Ba at r_0) except that (see second principle above) beta decays prevent it from going much past ^{68}Se , which eventually decays to ^{68}Zn .

Considering the third principle above, we are especially concerned with how much energy is deposited outside r_3 (where L_r^{crit} is maximized), since if too much energy is deposited there, the local luminosity L_r will drop below L_r^{crit} at r_3 and the model will be rendered inconsistent. The most dangerous candidate for depositing energy outside r_3 is ^{22}Mg , since its mean lifetime (5.57 s) is longer than those for ^{26}Si and ^{30}S (3.17 s and 1.70 s) and it can be burned up to ^{35}Cl . (The Appendix discusses this issue somewhat more thoroughly.)

This whole discussion suggests that we follow in detail the following abundances: $Y_{^{12}\text{C}}$, $Y_{^{22}\text{Mg}}$ (long-lived beta-decay parent), $Y_{^{22}\text{Na}}$ (its daughter), $Y_{^{35}\text{Cl}}$, $Y_{^{49}\text{Ti}}$, and $Y_{^{68}\text{Zn}}$ (end products of the rp-process at different radii). The reaction network is summarized as follows: (1) The hot CNO cycle, breakout, and the first portion of the rp-process are replaced by ^{12}C burning to ^{22}Mg . This is idealized as all occurring at r_1 , since breakout is here the limiting reaction, and it occurs predominantly at r_1 . (2) The nucleus ^{22}Mg , which is produced solely at r_1 , diffuses upward and downward from there as it decays to ^{22}Na . (3) The nucleus ^{22}Na is produced throughout the envelope by that decay and continues to diffuse. The ^{22}Na diffusing into r_3 is burned to ^{35}Cl . (4) The ^{22}Na diffusing into r_2 is burned to ^{49}Ti . In addition, any ^{35}Cl diffusing into r_2 (from r_3) is burned to ^{49}Ti . (5) The ^{22}Na diffusing into r_1 is burned to ^{68}Zn . Any ^{49}Ti diffusing into r_1 is burned to ^{68}Zn . (6) The ^{22}Na diffusing into r_0 is burned to ^{68}Zn .

After we have determined Y_k for these six species, it is a simple matter to determine the flux of these species into r_n and thus the luminosity produced there. In §5.2 we show details of how these calculations were done.

5.2. Method of solution

The algebra for obtaining this model is not dissimilar to that in §4. $Y_{12\text{C}}$ is nonzero for $r_1 < r < r_{\text{ph}}$. Because $Y_{12\text{C}}$ solves equation (4) with $\beta_i = \beta_j = 0$, we know it is of the form $Y_{12\text{C}}(r) = A + B\Xi(r)$, where A and B are constants we determine from knowledge of Ξ and from the boundary conditions,

$$Y_{12\text{C}}(r_1) = 0, \quad (19a)$$

$$Y_{12\text{C}}(r_{\text{ph}}) = Y_T. \quad (19b)$$

Because ^{22}Mg is beta unstable with mean lifetime 5.57 s and is created solely at r_1 after breakout happens there, we can find the function $Y_{22\text{Mg}}$ up to a constant factor by noting that it solves equation (4) with $\beta_j = 0$ and $\beta_i = 1/5.57 \text{ s} = 0.18 \text{ s}^{-1}$ for $r_0 < r < r_1$ and for $r_1 < r < r_{\text{ph}}$. Also

$$Y'_{22\text{Mg}}(r_0) = 0, \quad (20a)$$

$$Y_{22\text{Mg}}(r_{\text{ph}}) = 0. \quad (20b)$$

The function can be integrated in two pieces and will have a discontinuous derivative at r_1 . The final factor we can determine from the boundary condition

$$Y'_{12\text{C}}(r_1) = Y'_{22\text{Mg}}(r_1)_- - Y'_{22\text{Mg}}(r_1)_+, \quad (20c)$$

where the $-$ and $+$ refer to the left-hand- and right-hand-derivative, respectively. This equation expresses the fact that the flux of ^{12}C into r_1 is the same as the flux of ^{22}Mg out since ^{12}C is completely burned to ^{22}Mg at r_1 . Thus we obtain $Y_{12\text{C}}$ and $Y_{22\text{Mg}}$.

We can solve for ^{68}Zn by noting that it is a beta stable species created at r_0 and r_1 , so that it solves equation (4) with $\beta_i = \beta_j = 0$ for $r_0 < r < r_1$ and $r_1 < r < r_{\text{ph}}$. The function $Y_{68\text{Zn}}$ is of the form $A_1 + B_1\Xi(r)$ for $r_0 < r < r_1$ and of the form $A_2 + B_2\Xi(r)$ for $r_1 < r < r_{\text{ph}}$. We may determine the constants from the following boundary conditions:

$$Y_{68\text{Zn}}(r_{\text{ph}}) = 0, \quad (21a)$$

$$Y_{68\text{Zn}}(r_1) = Y_T - Y_{22\text{Mg}}(r_1), \quad (21b)$$

$$Y_{68\text{Zn}}(r_0) = Y_T - Y_{22\text{Mg}}(r_0). \quad (21c)$$

The last two equations are derived from the fact that the following equation holds at all radii:

$$Y_{12\text{C}} + Y_{22\text{Mg}} + Y_{22\text{Na}} + Y_{35\text{Cl}} + Y_{49\text{Ti}} + Y_{68\text{Zn}} = Y_T. \quad (22)$$

Also, of the functions Y_k , only $Y_{22\text{Mg}}$ and $Y_{68\text{Zn}}$ are nonzero at r_0 and r_1 , since the other species are quickly burned at these radii.

Similarly, $Y_{49\text{Ti}}$ solves equation (4) with $\beta_i = \beta_j = 0$ for $r_1 < r < r_2$ and $r_2 < r < r_{\text{ph}}$. (Note that $Y_{49\text{Ti}} = 0$ for $r < r_1$.) It is of the form $A_3 + B_3\Xi(r)$ for $r_1 < r < r_2$ and $A_4 + B_4\Xi(r)$ for $r_2 < r < r_{\text{ph}}$, where we determine the constants from the boundary conditions:

$$Y_{49\text{Ti}}(r_{\text{ph}}) = 0, \quad (23a)$$

$$Y_{49\text{Ti}}(r_2) = Y_T - Y_{68\text{Zn}}(r_2) - Y_{22\text{Mg}}(r_2), \quad (23b)$$

$$Y_{49\text{Ti}}(r_1) = 0. \quad (23c)$$

Similarly, $Y_{35\text{Cl}}$ solves equation (4) with $\beta_i = \beta_j = 0$ for $r_2 < r < r_3$ and $r_3 < r < r_{\text{ph}}$, such that

$$Y_{35\text{Cl}}(r_{\text{ph}}) = 0, \quad (24a)$$

$$Y_{35\text{Cl}}(r_3) = Y_T - Y_{68\text{Zn}}(r_3) - Y_{49\text{Ti}}(r_3) - Y_{22\text{Mg}}(r_3), \quad (24b)$$

$$Y_{35\text{Cl}}(r_2) = 0. \quad (24c)$$

Last, we determine $Y_{22\text{Na}}$ from equation (22).

After we have determined Y_k , we determine the flux of these species into r_n , that is, $4\pi r_n^2 \rho_n D_n Y'_k$, where ρ and D are evaluated at r_n to give ρ_n and D_n . The luminosity produced at r_n is then calculated by a formula similar to equation (10), with L_{nuc} replaced by L_n and $r_0^2 \rho_0 D_0$ replaced by $r_n^2 \rho_n D_n$. Again the energy is

TABLE 5

Some Physical Data and Luminosity Produced at Several Radii^a

n	r_n (cm)	ρ (g cm ⁻³)	v_{turb} (cm s ⁻¹)	l_{pres} (cm)	T (K)	n_+/n_e	L_r^{crit} (L _⊙)	L_n^{b} (L _⊙)
0	1.004(6)	2.74(3)	8.04(6)	2.19(5)	2.11(9)	3.42(1)	2740	13300
1	1.663(6)	4.42(2)	1.06(7)	3.78(5)	1.28(9)	1.34(1)	4830	51900
2	2.548(6)	1.03(2)	1.25(7)	6.30(5)	8.45(8)	2.03(0)	19610	20300
3	3.829(6)	2.97(1)	6.74(6)	9.75(5)	5.66(8)	1.72(-2)	81600	11300

^a This is for a model with $M = 16 M_{\odot}$, $M_{\text{core}} = 1 M_{\odot}$, and $L_{\text{ph}} = 88,600 L_{\odot}$. Here and elsewhere the number in parentheses is the power of ten by which to multiply the preceding number.

^b This is the luminosity produced at radius r_n in the model described in §5.

given by the mass difference between products and reactants, less half the beta decay energy.

5.3. Results

The results are shown in Table 5 and in Figure 6. L_n is the energy per time produced at shell n (not the total luminosity at that radius). Although the sum $\sum_n L_n = 96,800 L_{\odot}$ is somewhat greater than $L_{\text{ph}} = 88,600 L_{\odot}$, it is close enough to L_{ph} for this study. In Figure 6, the curve labeled L_r is the cumulative sum of L_n , normalized by a factor of $88,600/96,800$. Also shown in Figure 6 is an interpolated curve L_r^{int} which is a very rough approximation to our model's L_r . It is given by

$$L_r^{\text{int}} = L_{\text{ph}} \left(1 - \left(\frac{a}{r} \right)^2 \right), \quad (25)$$

where $a = 9.5$ km. This choice of L_r^{int} reflects several considerations. The value of L_r^{int} at r_3 reflects the idea that about half of the energy L_3 is actually produced outside r_3 and half is produced inside. We deduce this half-and-half split by noting that $Y'_{22\text{Na}}(r_3)_+ = -2 \times 10^{-8}$ moles g⁻¹ cm⁻¹ and $Y'_{22\text{Na}}(r_3)_- = 3 \times 10^{-8}$ moles g⁻¹ cm⁻¹ are approximately equal in magnitude, that is, the fluxes of ²²Na

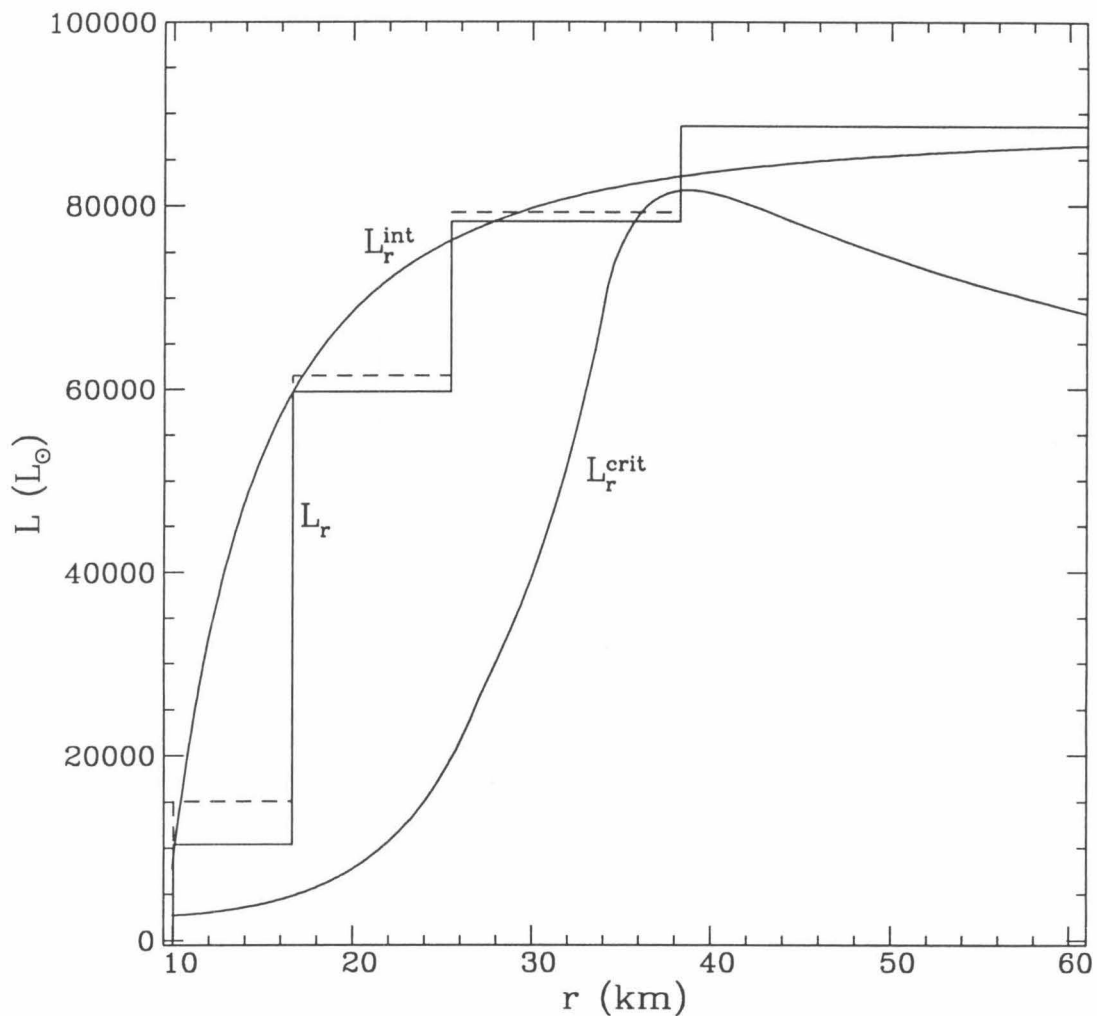


Fig. 6—Local luminosity L_r plotted versus r (solid jagged curve) for the model described in §5 corresponding to a star with total mass $16 M_\odot$ and photospheric luminosity $88,600 L_\odot$, where we are here assuming that nuclear burning occurs throughout the lower portion of the envelope. The quantity L_r^{int} is an interpolation of local luminosity fitted to L_r . It is given by $L_{\text{ph}} (1 - (9.5 \text{ km}/r)^2)$. The critical luminosity L_r^{crit} is also shown. Note that L_r^{int} is greater than L_r^{crit} for r greater than about 10 km, as we would hope in order to have a consistent model. The dashed jagged curve is the second-order-corrected local luminosity versus radius whose calculation is detailed in §6.

from outside and inside of r_3 into r_3 are approximately equal. Also, expression (25) is chosen to make L_r^{int} much steeper near r_0 and r_1 than the curve L_r . This is because the model in §5.1 tends to underestimate the luminosity produced at r_0 , since it does not adequately take into account the smearing of luminosity production by shorter-lived beta-decay parents, which carry energy from r_2 to r_0 (see the fourth paragraph in §5.1). Nevertheless, the final model is insensitive to the exact choice of L_r^{int} , as we shall see in §6.

A viable model requires that $L_r > L_r^{\text{crit}}$ for all $r > r_0$. This is true of L_r^{int} ; however, L_r^{int} gets uncomfortably close to L_r^{crit} at r_3 . Is this a problem? It could be, since inclusion of other effects (general relativity, accretion, proper treatment of convection, and so on) could affect the luminosity curve by, say, 10% in either direction. A more nearly complete model with general relativity, accretion, and inclusion of other nuclear species might clear up the issue.

For stars with greater masses, the margin between L_r and L_r^{crit} is larger. For example, a star of $20 M_\odot$ with a $1 M_\odot$ core and $Z = 0.02$ on the surface gives a consistent model with $L = 103,500 L_\odot$. In this model the shape of Y_i versus r is almost unchanged from that of the model with $M = 16 M_\odot$, and thus L_r versus r is almost unchanged except for a factor of $103,500/88,600$ compared with Figure 6. The quantity L_r^{crit} still has a maximum at $80,000 L_\odot$ and so L_r easily clears it everywhere in the envelope. Thus, although we may be a little insecure about the existence of a consistent model for $M = 16 M_\odot$, we can be sure about the existence of models for greater masses. The small margin by which L_r clears L_r^{int} in this model leads us to believe that the upper limit of the mass gap (mentioned in §1) is around $16 M_\odot$.

6. Iteration and thus a consistent model

6.1. Iteration

Now that equation (25) gives us an idea of the dependence of local luminosity on radius, we will use that equation for L_r in GOB (instead of setting L_r to L_{ph}) and thus modify the physical structure. With this second-order physical

structure we will obtain a second-order nuclear-abundance structure. Table 6 gives some details as to the resulting second-order physical structure of the envelope. (Actually this second-order physical structure looks almost the same as the first-order one, except that the turbulent velocity is less where L_r is smaller, decreasing in some places by about a factor of 3.) Table 7 shows the results of using this physical structure and the methods of §5 to get a second-order nuclear-abundance structure. The values of L_n have changed little from their values in Table 5, so that we may say that the model is insensitive to the exact choice of L_r^{int} . The values of L_n have not changed enough to cause us to re-evaluate our original rough estimate, equation (25). Thus the iteration has converged.

This model still vastly simplifies the physical situation. Besides systematic errors listed in §1, what physics have we omitted? Most important, perhaps, is the fact that in the hottest regions (at $T \gtrsim 1.5 \times 10^9$ K) alpha addition reactions can compete with beta decay (the reaction rates are somewhat uncertain):



(Alpha addition onto nuclei larger than ${}^{30}\text{S}$ is rare, because of the Coulomb barrier.) In models constructed with the first of these reactions included, the main effect is that luminosity is produced at smaller radii, so including the reactions would cause L_r^{int} to exceed L_r^{crit} by a greater margin than that shown in Figure 6.

6.2. Stability against radial adiabatic perturbations

Because the equation of state is very soft for much of the star, especially for the small region where electron-positron pairs are present ($\Gamma \equiv (\partial \ln P / \partial \ln \rho)_S \sim 1.2$) and for the huge radiation dominated envelope ($\Gamma - \frac{4}{3} \approx 2 \times 10^{-3}$), there is some danger that the star might be unstable against radial perturbations. A test for stability was therefore performed under the idealizing assumption that the perturbations are adiabatic. The test used the method outlined in Chapter 27 of Cox and Giuli (1968). The test involves the function

$$\frac{\delta r}{r} = \xi(r)e^{-i\omega t},$$

TABLE 6

Physical Structure (Second Order) of a Modified Envelope^a

$r(\text{cm})$	ρ (g cm^{-3})	v_{turb} (cm s^{-1})	l_{pres}/r	t_{turb} (s)	$T(\text{K})$	n_+/n_e	L_r^{crit} (L_{\odot})	L_r (L_{\odot})
1.004(6)	2.74(3)	3.60(6)	0.221	6.1(-2)	2.11(9)	3.42(1)	2.74(3)	9.27(3)
1.133(6)	1.78(3)	5.62(6)	0.218	4.4(-2)	1.87(9)	2.93(1)	2.92(3)	2.63(4)
1.279(6)	1.15(3)	6.93(6)	0.219	4.0(-2)	1.66(9)	2.42(1)	3.24(3)	3.97(4)
1.443(6)	7.38(2)	8.03(6)	0.222	4.0(-2)	1.48(9)	1.90(1)	3.76(3)	5.02(4)
1.663(6)	4.42(2)	9.22(6)	0.227	4.1(-2)	1.28(9)	1.34(1)	4.83(3)	5.97(4)
1.916(6)	2.67(2)	1.03(7)	0.234	4.3(-2)	1.12(9)	8.36(0)	6.84(3)	6.68(4)
2.208(6)	1.64(2)	1.12(7)	0.241	4.7(-2)	9.71(8)	4.57(0)	1.09(4)	7.22(4)
2.547(6)	1.03(2)	1.17(7)	0.247	5.4(-2)	8.45(8)	2.03(0)	1.96(4)	7.63(4)
2.878(6)	6.99(1)	1.15(7)	0.251	6.3(-2)	7.49(8)	7.39(-1)	3.36(4)	7.89(4)
3.319(6)	4.53(1)	9.20(6)	0.254	9.1(-2)	6.52(8)	1.68(-1)	6.13(4)	8.13(4)
3.828(6)	2.97(1)	4.05(6)	0.255	2.4(-1)	5.66(8)	1.72(-2)	8.16(4)	8.31(4)
4.415(6)	1.95(1)	6.64(6)	0.255	1.7(-1)	4.92(8)	1.30(-3)	7.86(4)	8.45(4)
5.094(6)	1.28(1)	8.76(6)	0.256	1.5(-1)	4.28(8)	5.07(-5)	7.38(4)	8.55(4)
5.879(6)	8.41(0)	1.04(7)	0.256	1.5(-1)	3.72(8)	1.16(-6)	6.93(4)	8.63(4)
6.788(6)	5.53(0)	1.17(7)	0.257	1.5(-1)	3.23(8)	1.41(-8)	6.53(4)	8.69(4)
7.842(6)	3.63(0)	1.30(7)	0.258	1.6(-1)	2.81(8)	8.4(-11)	6.18(4)	8.73(4)
1.347(7)	7.64(-1)	1.71(7)	0.262	2.1(-1)	1.67(8)	0.	5.22(4)	8.82(4)
3.175(7)	6.95(-2)	2.29(7)	0.274	3.8(-1)	7.48(7)	0.	4.46(4)	8.85(4)
7.927(7)	6.40(-3)	2.83(7)	0.298	8.3(-1)	3.35(7)	0.	4.12(4)	8.86(4)
2.210(8)	6.13(-4)	3.16(7)	0.341	2.4(0)	1.49(7)	0.	3.95(4)	8.86(4)
7.442(8)	6.60(-5)	2.97(7)	0.409	1.0(1)	6.59(6)	0.	3.88(4)	8.86(4)
3.291(9)	8.90(-6)	2.16(7)	0.495	7.5(1)	2.88(6)	0.	3.81(4)	8.86(4)
1.964(10)	1.63(-6)	1.17(7)	0.578	9.7(2)	1.25(6)	0.	3.74(4)	8.86(4)
1.487(11)	4.06(-7)	4.92(6)	0.650	2.0(4)	5.35(5)	0.	3.54(4)	8.86(4)
1.226(12)	1.38(-7)	1.88(6)	0.743	4.8(5)	2.28(5)	0.	2.39(4)	8.86(4)
1.005(13)	5.81(-8)	6.80(5)	1.137	1.8(7)	1.02(5)	0.	9.92(3)	8.86(4)
4.860(13)	2.02(-8)	3.34(5)	0.311	4.5(7)	4.82(4)	0.	1.51(4)	8.86(4)
6.801(13)	9.07(-9)	3.74(5)	0.106	1.9(7)	2.20(4)	0.	1.20(4)	8.86(4)
7.607(13)	4.92(-9)	2.66(5)	0.030	8.7(8)	9.97(3)	0.	7.39(3)	8.86(4)
7.722(13)	6.76(-9)	6.80(3)	0.011	1.2(8)	4.57(3)	0.	3.55(7)	8.86(4)

^a This corresponds to a star with $M = 16 M_{\odot}$, $M_{\text{core}} = 1 M_{\odot}$, local luminosity given by equation (25), and $L_{\text{ph}} = 88,600 L_{\odot}$.

TABLE 7

Physical Data and Luminosity Produced at Several Radii(Modified envelope)^a

	r_n	ρ	v_{turb}	l_{pres}	T		L_r^{crit}	L_n^{b}
n	(cm)	(g cm ⁻³)	(cm s ⁻¹)	(cm)	(K)	n_+/n_e	(L _⊙)	(L _⊙)
0	1.004(6)	2.74(3)	3.60(6)	2.19(5)	2.11(9)	3.42(1)	2740	17000
1	1.663(6)	4.42(2)	9.22(6)	3.78(5)	1.28(9)	1.34(1)	4830	52100
2	2.547(6)	1.03(2)	1.17(7)	6.30(5)	8.45(8)	2.03(0)	19610	11900
3	3.828(6)	2.97(1)	4.05(6)	9.75(5)	5.66(8)	1.72(-2)	81600	10500

^a This corresponds to a star with $M = 16M_{\odot}$, $M_{\text{core}} = 1 M_{\odot}$, and local luminosity given by equation (25), $L_{\text{ph}} = 88,600 L_{\odot}$.

^b This is the luminosity produced at radius r_n in the model described in §6.

where δr is the radial displacement of a fluid element from equilibrium. This displacement and its eigenfrequency ω satisfy the following eigenvalue problem:

$$-\frac{1}{\rho r^4} \frac{d}{dr} \left(P \Gamma r^4 \frac{d\xi}{dr} \right) - \frac{1}{\rho r} \frac{d}{dr} \left[(3\Gamma - 4) P \right] \xi = \omega^2 \xi \quad (A)$$

subject to

$$\frac{d\xi}{dr} = 0 \quad \text{at } r = 0, \quad (B)$$

$$\frac{r_{\text{ph}}}{\xi} \frac{d\xi}{dr} = \frac{1}{\Gamma} \left[\frac{\omega^2 r_{\text{ph}}^3}{GM} - (3\Gamma - 4) \right] \quad \text{at } r = r_{\text{ph}} \quad (C)$$

[cf. equations (27.57), (27.59) and (27.62) of Cox and Guili (1968)]. The model is unstable if the smallest eigenvalue ω_0^2 is negative. The radial instability (by contrast with nonradial, convective instabilities) is a global phenomenon. A star can have its adiabatic index Γ much less than the “critical value” of $\frac{4}{3}$ over small regions and still be stable if Γ is sufficiently larger than $\frac{4}{3}$ in adjacent regions. Thus, to test for stability, we must take proper account of the influence of the regions with $\Gamma > \frac{4}{3}$ both below the dangerous electron-positron pair region and above it. Our model envelopes include the region above but not the region below.

Accordingly, to test stability we spliced the envelope with $M_{\text{env}} = 15 M_{\odot}$ and $L = 88,600 L_{\odot}$ onto two models for a neutron star (Arnett and Bowers 1977, models L and B), one with a hard equation of state (Pandharipande and Smith 1975) the other with a soft equation of state (Pandharipande 1971; Baym, Pethick, and Sutherland 1971; Baym, Bethe, and Pethick 1971). (The details of splicing in no way affected the final result.)

The value of ω_0^2 for our envelope plus neutron-star core was then computed by trial and error ("shooting"). We set $\xi(0) = 1$ and $\xi'(0) = 0$, chose a value of ω^2 , and integrated equation (A) from $r = 0$ to r_{ph} . If ξ was positive for all r and the outer boundary condition was satisfied, then $\omega_0^2 = \omega^2$; if ξ was positive for all r and the left hand side of equation (C) exceeded the right hand side, then $\omega_0^2 > \omega^2$; otherwise $\omega_0^2 < \omega^2$. Subsequent integrations allowed us to converge on ω_0^2 . Table 7A displays the results. Models 3-5 are obtained by using the structure of the neutron star derived from the soft equation of state, but with the neutron star's Γ in equation (A) artificially replaced by the shown value (and the correct Γ retained in the envelope). This is included to show just how soft the neutron star must be to allow this sort of instability. The last column is the period $2\pi/\omega_0$ for the longest oscillation.

The entries in the third column of Table 7A are the same not only to three digits shown but to all digits in this eight-byte integration (FORTRAN double precision). This indicates that the core has almost no influence on the oscillations. The reason is the poor impedance match in equation (A) between the dense, high-pressure core and the tenuous, low-pressure envelope with the result that the value of ξ is negligibly small in the core compared to its value in the outer envelope ($r \gtrsim 100$ km). The pressure of a poorly impedance matched core below the region with pairs and a radiative envelope above it with $\Gamma - \frac{4}{3} \approx 2 \times 10^{-3} > 0$ is enough to counteract the destabilizing influence of the pair region.

6.3. Lifetime

[This section is presented as it was originally published. The discussion is superseded by the discussion in Chapter 4 of this thesis.]

TABLE 7A

Fundamental Mode for Radial Adiabatic Oscillation			
model	eos for neutron star ^a	$\omega_0^2(\text{s}^{-2})$	T
1	hard	3.13×10^{-15}	1300 days
2	soft	3.13×10^{-15}	1300 days
3	soft($\Gamma = 1.334$)	3.13×10^{-15}	1300 days
4	soft($\Gamma = 1.3333334$)	3.13×10^{-15}	1300 days
5	soft($\Gamma = 1.333333334$)	-2.25	...

^a See §6.2. for details of these equations of state.

The star should remain in this rp stage until it has exhausted its supply of light metals needed as seed. We can set an upper limit on the time this takes by dividing the total nuclear energy available to the star by a typical luminosity. The number of ^{12}C atoms is approximately $M_{\text{env}}ZL/12$, where M_{env} is the mass of the envelope, Z is the initial metallicity, L is Avogadro's number, and 12 is the atomic weight of carbon. If each ^{12}C atom is burned to ^{68}Se , then it yields about $E_{\text{heat}} = 320$ MeV, and thus (using $Z \sim 0.02$) the total time the star spends in this phase of its life is not longer than

$$T_{\text{life}} \approx 1.4 \times 10^6 \text{ yr.} \quad (26)$$

This is roughly the same as the lifetime of a normal red giant. (Note that one scenario of creation for this star involves the coalescence of a neutron star and a normal star in a close binary system. In this case the normal star might have acquired considerable material from the supernova which created the neutron star, resulting in an enhancement of metallicity. If one solar mass of metals was transferred to the envelope, we might have $Z \sim 1 M_{\odot}/16 M_{\odot} \sim 0.06$. In this case T_{life} would be $\sim 6 \times 10^7$ yr. By this time, however, stellar winds will have blown off much if not all of the envelope.)

The rate at which matter accretes onto the core is also easily estimated. We consider L^{crit} at the edge of the core (call it L_0^{crit}), since it is this luminosity that must be produced by release of gravitational energy in order to splice a core

onto the envelope we have constructed. A parcel of matter of mass Δm releases approximately $E = GM_{\text{core}} \Delta m / r_0$ by accreting onto the core, so that the mass accretion rate is given by

$$\begin{aligned} \dot{M} &= L_0^{\text{crit}} \left(\frac{GM_{\text{core}}}{r_0} \right)^{-1} \\ &\approx 1.3 \times 10^{-9} M_{\odot} \text{ yr}^{-1}, \end{aligned} \quad (27)$$

where we have used $L_0^{\text{crit}} \approx 2700 L_{\odot}$ from Table 1. The time to accrete about $1 M_{\odot}$, at which point the core will exceed the Oppenheimer-Volkoff limit and will be in danger of collapsing, is about 8×10^8 yr, which is a factor of 600 larger than the T_{life} calculated above. Thus, the accretion should not modify T_{life} significantly, and equation (26) is a reasonable estimate.

7. Possible observations

[This section is presented as it was originally published. The discussion is superseded by the discussion in Chapter 4 of this thesis.]

Because our models are convective from the burning region to the photosphere, we may predict that there will be an accumulation of reaction products at the surface of the star. A signature for these stars would be a large quantity of an rp-process isotope which is produced in only small quantities in normal stellar processes. If we can observe on a normal red supergiant absorption lines of a molecule containing a heavy metal atom, then the corresponding absorption lines observed on a supergiant with a degenerate neutron core should be shifted, due to the peculiar presence of the rp-isotope.

The following candidates are rp-process isotopes which are not produced by the r- or an s-process and are not the most prevalent isotope of the element in normal Population I abundances:

$${}^{50}\text{Cr}, {}^{54}\text{Fe}, {}^{74}\text{Se}, {}^{78}\text{Kr}, {}^{84}\text{Sr}, {}^{92}\text{Mo}, {}^{96}\text{Ru}, {}^{102}\text{Pd}, {}^{106}\text{Cd}.$$

Because of the environment at the surface of the star (hydrogen rich, relatively warm for molecules), the best candidates for observation are diatomic hydrides

TABLE 8

Transition for SrH				
electronic transition	vibrational (v', v'')	band	bandhead (\AA)	isotopic shift ^a (\AA)
$A^2\Pi \leftarrow X^2\Sigma$	(0,0)	P ₁	7508	~ 0.0095
	(0,0)	^P Q ₁₂	7505	~ 0.0095
	(0,0)	^Q P ₂₁	7348	~ 0.0094
	(0,0)	Q ₂	7346.7	~ 0.0094

^a This shift is for ^{84}SrH relative to ^{88}SrH . In this column the shift in the line represented by $J' = 9\frac{1}{2} \leftarrow K'' = 10$ is shown. The shift here is entirely due to rotational structure; the vibrational shift in P₁ and ^PQ₁₂ is comparable.

with high dissociation energies. If we narrow the list to those elements which have spectra of diatomic hydrides documented in the literature, then only ^{74}Se , ^{84}Sr , and ^{106}Cd remain (^{74}Se : Bollmark *et al.* 1978, Bollmark, Lindren, and Sassenberg 1980; ^{84}Sr : Rosen 1970, Watson and Fredrickson 1932; ^{106}Cd : Svenson 1929). Of these hydrides, SrH has transitions (see Table 8) in an easily observable portion of the spectrum (without many TiO and VO lines).

Shifts in vibrational and rotational structure of an electronic transition depend on the reduced mass of the molecule (and thus on the isotope of the metal), as described by Herzberg (1950). Current capability includes the ability to resolve rotational lines but not to resolve isotopes, so that a study of absorption line centroids should reveal the ratio $n(^{84}\text{Sr})/n(^{88}\text{Sr})$ on the surface. Currently a study motivated by this work is underway by Jeremy Mould to determine whether SrH can be observed at all on the surfaces of cool stars. If ^{84}Sr were found with far greater abundance than expected through normal stellar processes, then this would be strong evidence for some abnormal rp-process producing the material on the surface of the star and for the presence of a degenerate neutron core.

Another diagnostic would be an overabundance of elements with $32 < Z < 40$

on the surface of the star, since the rp-process will be very efficient in converting C, N, and O into species in this range. This should be easier to observe since it involves measuring the strengths of atomic or ionic lines instead of searching for a small shift in absorption lines of a molecule. Table 2 suggests an overabundance in species with $A = 68, 81, \text{ and } 82$ (i.e., ^{68}Zn , ^{81}Br , and ^{82}Kr), but this prediction could be completely changed by improved information concerning nuclear masses, beta decay lifetimes, and branches in this paper's simplified rp network. However, the qualitative prediction of an overabundance of elements with $32 < Z < 40$ seems rather firm.

8. Conclusion

This study continues a project begun by TŻ and answers in the affirmative the question, can we construct a consistent model for a supergiant which realistically includes a turbulent burning zone? It also provides a prediction for an observational signature for such a star: the presence of rp-process elements on the surface.

Specifically, a one-dimensional equilibrium model has been constructed in which convection transports material and energy from the edge of the core to the surface of the star and in which energy generation occurs through rp burning. This feature provides the most probable avenue for observing these stars. A strong presence of rp-process elements on the surface of the star would indicate the presence of a degenerate neutron core. The molecule ^{84}SrH is presented as a candidate.

The situation is clearly more complicated than that presented in this preliminary study. A more nearly complete treatment would require performing an envelope analysis for each change in core mass as the core accretes, provision for changes in envelope composition as time progresses, and a detailed analysis of the burning region, as well as relativistic effects and effects of envelope accretion. (Cannon *et al.* 1991 addresses many of these issues.) Also not addressed in this study are issues of the stability and uniqueness of the solution, the effects of a

magnetic field associated with the core, and the approach to steady state. Our present simple analysis merely provides some semi-quantitative indication of the features of such a star.

The largest question left unaddressed by this study is, of course, whether a star with a degenerate neutron core can actually form in nature. A full study of this has not been done, but for some insights into it see the references given in §1.

This work would not have been possible without the suggestions and guidance provided by Kip Thorne. The author wishes to thank Jeremy Mould for numerous discussions which formed the substance of §7. The author would also like to thank Stanford Woosley for helpful discussion of the rp-process and other miscellaneous topics. This research was supported in part by National Science Foundation Grant AST-8817792.

Appendix

In this Appendix we shall justify the assumptions made in determining the nuclear-abundance structure, that is, we shall justify the reaction networks used and the choices of nuclear species which we followed. The Appendix is divided into three sections, the first exploring the rp-process used in §4, the second treating the rp-process of §§5 and 6, and the third treating the hot CNO cycle.

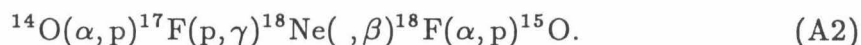
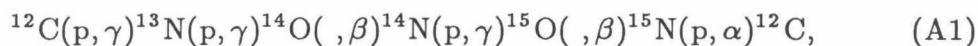
A.1. rp-process in §4

In this section we will consider how to simplify the rp-process for the calculation in §4. We will keep in mind that we can ignore any reaction (besides beta decays) that takes longer than about 0.1 s (the time for turbulent turnover near the edge of the core).

All the rates for the proton addition reactions were obtained from Woosley *et al.* (1978) where available or else from Caughlin and Fowler (1988) or from the Hauser-Feshbach theory (eq. [30] of Woosley *et al.* 1975). Woosley *et al.* (1975) suggest dividing the Hauser-Feshbach rates by 2, and we have done this here, although this is generally a trivial correction for our purpose. The reverse reactions

were calculated from equation (10) in Woosley *et al.* (1978), given as equation (A10) below. The factor REV in their equation (10) was estimated to be 10^{10} when it was not otherwise given. Masses of nuclei were taken from Lederer and Shirley (1978) where available. Otherwise masses were estimated from the semi-empirical mass formula with estimated shell corrections, as explained in Myers and Swiatecki (1966; see especially §7.10). Beta decays were taken from Lederer and Shirley (1978) where available or else from Takahashi, Yamada, and Kondoh (1973).

To gain some understanding of the rp-process in this hot convective region, consider a seed nucleus (^{12}C , although ^{14}N or ^{16}O works similarly) which random walks from the surface of the star toward the burning region. As the density and temperature rise, the initial seed nucleus participates in the reactions (A1) and side reactions (A2) of the hot CNO cycle (Audouze, Truran, and Zimmermann 1973):



[Note that the completed CNO cycle contributes negligibly to the energy of the star. To see this, we can get a quick estimate of the contribution of the hot CNO cycle to the luminosity by assuming the following: The beta decay of ^{15}O is the limiting process for the hot CNO cycle, so all the seed nuclei (those not having undergone breakout) are in the form ^{15}O between r_0 and r_5 , where r_5 is the radius at which $^{14}\text{N}(p, \gamma)^{15}\text{O}$ becomes facile. (At cooler temperatures than those at r_5 the CNO goes hardly at all.) The concentration of ^{15}O is given by $Y_T \Xi(r)$ between r_0 and r_5 , where $\Xi(r)$ is the function defined in equations (12), and the total amount of ^{15}O is given by

$$N_{\text{O15}} = \int_{r_0}^{r_5} Y_T \Xi \rho 4\pi r^2 dr = 1.9 \times 10^{18} \text{ moles.}$$

If the total energy of the hot CNO cycle $E_{\text{CNO}} = 21 \text{ MeV}$ is released upon a decay of ^{15}O , then the total luminosity is given by

$$L_{\text{CNO}} = N_{\text{O15}} E_{\text{CNO}} L / \tau_{\text{O15}} = 56 L_{\odot},$$

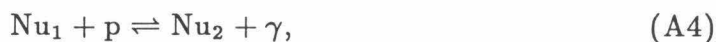
where L is Avogadro's number and τ_{O15} is the mean lifetime of ^{15}O , 176 s. This is negligible.]

As a result of reactions (A1) and (A2), the seed is most likely to be in the form ^{15}O , the major hangup of the CNO cycle. At some radius r_1 near the edge of the core the density and temperature become such that the breakout reaction $^{15}\text{O}(\alpha, \gamma)^{19}\text{Ne}$ occurs in about 0.1 s. In the envelope with $L_{\text{nuc}} = 88,600 L_{\odot}$ that we look at in §4, breakout occurs when $T = 1.3 \times 10^9$ K and $\rho = 440 \text{ g cm}^{-3}$, and we will be using this temperature and density in most of our reaction rate calculations.

Once the seed breaks out of the hot CNO cycle, proton addition and the reverse reaction occur very quickly ($\sim 10^{-8}$ s), bringing the following reactions into equilibrium:



The corresponding reaction rates are given in Table 9 and are defined by the following: If we consider a single equilibrium



then the reaction rates $R_{\pm p}$ are given by

$$\frac{dY_{\text{Nu1}}}{dt} = -R_{+p} Y_{\text{Nu1}} Y_{\text{H}} = -R_{+p} Y_{\text{Nu1}} X \rho \quad (\text{A5})$$

for proton addition (where X is the mass fraction of hydrogen in the burning region, ρ is the density, and $Y_{\text{H}} = X\rho$ since the molecular weight of ^1H is 1 moles g^{-1}) and by

$$\frac{dY_{\text{Nu2}}}{dt} = -R_{-p} Y_{\text{Nu2}} \quad (\text{A6})$$

for proton emission. Later we will estimate characteristic times for these processes given by

$$t_{+p} = -\frac{Y_{\text{Nu1}}}{dY_{\text{Nu1}}/dt} = (R_{+p} X \rho)^{-1}, \quad (\text{A7})$$

$$t_{-p} = -\frac{Y_{\text{Nu2}}}{dY_{\text{Nu2}}/dt} = (R_{-p})^{-1}. \quad (\text{A8})$$

TABLE 9

Reaction Rate Data for First Equilibrium ^a				
equilibrium		R_{+p}	R_{-p}	
Nu_1	$\xrightarrow[+p]{-p} \text{Nu}_2$	(g mole ⁻¹ s ⁻¹)	(s ⁻¹)	$Y_{\text{Nu}_2}/Y_{\text{Nu}_1}$
¹⁹ Ne	$\xrightarrow[+p]{-p} \text{}^{20}\text{Na}$	9×10^4	1.3×10^6	5×10^{-2}
²⁰ Na	$\xrightarrow[+p]{-p} \text{}^{21}\text{Mg}$	4×10^4	1.2×10^2	9×10^{-6}

^a This is the first equilibrium of nuclei connected by proton addition in the rp-process, calculated at radius $r_1 = 16.63$ km, $T = 1.28 \times 10^9$ K, $\rho = 442$ g cm⁻³ inside the envelope of Table 6.

If we assume equilibrium, then the forward and reverse rates are equal and we calculate, from setting equations (A5) and (A6) equal,

$$\frac{Y_{\text{Nu}_2}}{Y_{\text{Nu}_1}} = \frac{R_{+p}}{R_{-p}} X \rho. \quad (\text{A9})$$

This ratio and the accompanying reaction rates are given in Table 9.

By taking all the reactions (A3) into account and setting time derivatives to zero, we can determine the equilibrium concentrations of the species in this little chain. In this way we find that ²¹Mg will be the predominant species. After the beta decay of ²¹Mg (about 0.18 s), a new set of equilibria is established among the next series of isotopes connected by proton addition and terminated by a beta decay. This equilibrium is treated in the same way, and the process is continued until nuclei of large mass are produced. When the nucleus reaches the size of ⁷⁰Br, proton addition takes about as long as turbulent turnover at this radius of the envelope (where breakout occurs). Near the edge of the core where $T = 2.1 \times 10^9$ K and $\rho = 2700$ g cm⁻³, the mass of the nuclei can be pushed up further, up to ¹²⁰Ba, when again the time for proton addition is about as long as turbulent turnover.

Figure 7 summarizes the results of this calculation, showing the rp-process through ⁹⁶Pd. (At this point, as we see in §4, the beta decays have become long

enough to turn off the process.) Notice from this figure that there are four species with $A \leq 39$ which take longer than 1.5 s to decay, species with $40 \leq A \leq 67$ have very short beta decay times (< 0.8 s), and many species with $A \geq 67$ have quite long beta decay times (> 100 s). Species with mean lifetimes greater than 1.5 s were included in the simplified reaction network of §4 (Table 2) if $A \leq 39$, and species with mean lifetimes greater than 10 s were included if $A \geq 67$. (See, however, Chapter 4 of this thesis in which Figure 7 is superseded.)

We have been looking at the rp-process at the radius r_1 where breakout occurs. If we perform the same analysis at different radii in the burning region, we find that we reproduce Figure 7 with very few changes, except that the rp-process terminates sooner at cooler temperatures. This statement is borne out by the similarity even in detail between Figure 7 here and Figure 3 in Wallace and Woosley (1981), calculated at a different temperature and density. (In some envelopes the temperatures and densities are great enough to initiate $^{22}\text{Mg}(\alpha, p)^{25}\text{Al}$ and other alpha addition reactions, but separate calculations including these reactions did not change the results significantly.)

This simplified reaction network should remain more or less valid until the temperature reaches some maximum value at which photon-induced proton emission begins to dominate, that is, the equilibria represented by reaction (A4) (such as reactions [A3]) shift significantly to the left. We can estimate this temperature T_{max} by looking at equation (10) in Woosley *et al.* (1978) for the relationship between the forward and reverse reaction rates in equation (A5) and (A6),

$$R_{-p} = \text{REV} \frac{g_1}{g_2} T_9^{3/2} R_{+p} \exp\left(\frac{-11.605Q}{T_9}\right). \quad (\text{A10})$$

Here g_i is the statistical weight of Nu_i , Q is the energy of the reaction in MeV, and T_9 is $T/10^9\text{K}$. The shift leftward in equation (A3) occurs when $t_{+p} = t_{-p}$, i. e., when $R_{+p}X\rho = R_{-p}$ (cf. eqs. [A7] and [A8]). We can compute the temperature T_9 at which the shift occurs by combining this relation with equation (A10). In so doing, we estimate $g_1 = g_2$ and $\text{REV} = 10^{10}$ for a typical proton addition reaction, and we substitute in typical values $X \sim 0.7$ and $\rho \sim 10^4 \text{ g cm}^{-3}$. For Q we use a typical energy of reaction for proton addition. This can be obtained by adding the

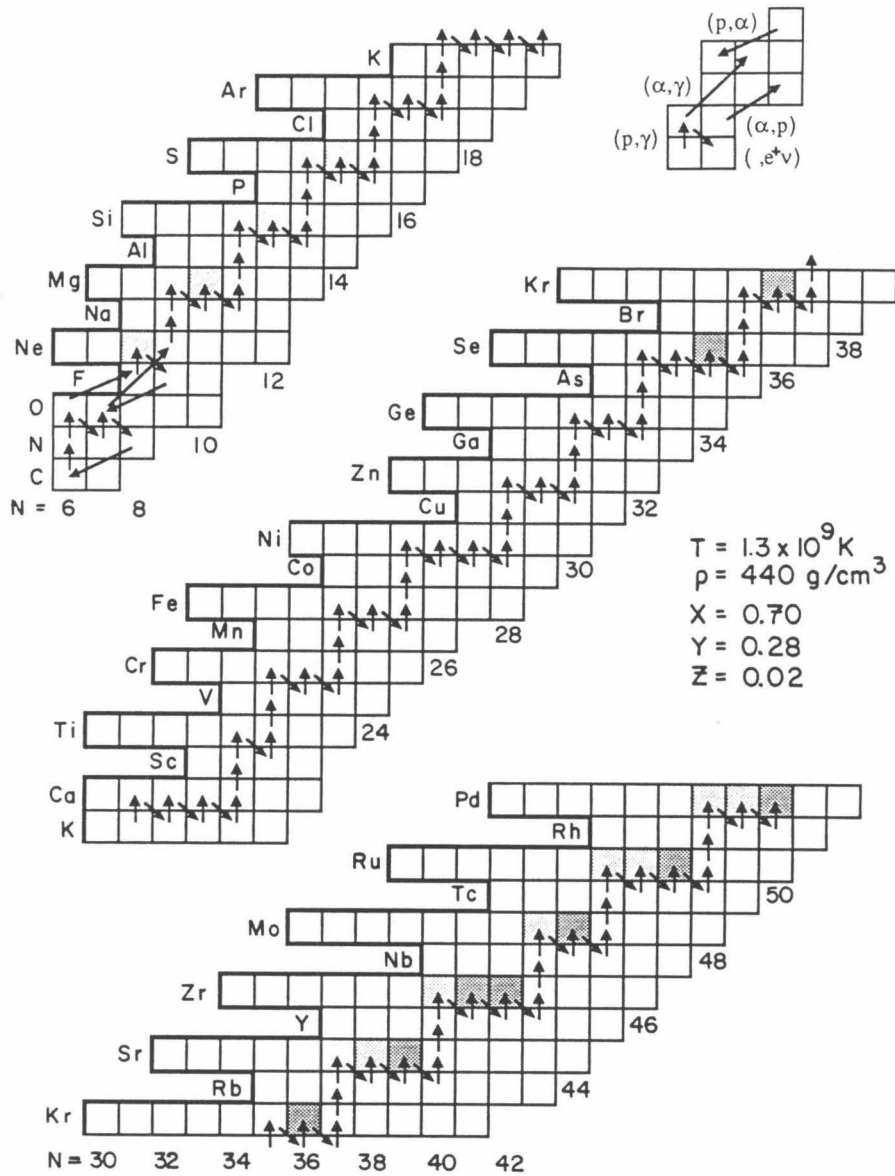


Fig. 7—Simplified rp reaction network as derived in the Appendix, §A.1, and used in §§4, 5, and 6 of the text. The solid dark line along the left border of the diagram is the proton drip line, so that isotopes to the left of the line are subject to protons spontaneously dripping off. The hot CNO cycle is shown (eq. [A1]) along with the side chain (eq. [A2]) and the breakout reaction (connecting ^{15}O and ^{19}Ne). The boxes shaded a light gray correspond to beta-unstable parents which take longer than 1.5 s to decay, while the boxes shaded a dark gray correspond to parents which take longer than 10 s to decay. The latter have the effect of cutting off the rp-process in the star.

energies in column 6 of Table 2, subtracting the energies in column 7, and dividing by the number of protons consumed, i. e., $Q \approx (672 - 354)\text{MeV}/80 \approx 4 \text{ MeV}$. The result of using these estimates in $R_{+p}X\rho = R_{-p}$ and equation (A10) is

$$T_{max} \sim 3 \times 10^9 \text{ K.} \quad (\text{A11})$$

Note that this excludes the first three envelopes of Table 1.

A.2. rp-process in §§5 and 6

In this section we will fill in some of the detail behind the principles spelled out in §5.1. In §1 of this Appendix we presented a simplified rp network for $T = 1.3 \times 10^9 \text{ K}$ and $\rho = 440 \text{ g cm}^{-3}$ (i. e., at r_1). If we perform the same analysis at the radii r_0 , r_2 , and r_3 defined in §5.1, then we get the same network as in Figure 7 except that at cooler temperatures the proton addition does not proceed as far, that is, the proton addition time exceeds $\sim 0.1 \text{ s}$ at a lower atomic number. (By comparison, the turbulent turnover time varies little from 0.1 s for the various radii.) This is the idea behind the first principle in §5.1.

For each radius r_n we need to know approximately at what species the rp-process stops, that is, the first species for which the proton addition time is longer than the turbulent turnover time. The proton addition times at r_3 are shown in Table 10. By comparing with the turbulent turnover time (0.14 s), we deduce that the rp-process stops at about ^{35}Ar (which decays eventually to ^{35}Cl). Similarly, we determine that at r_2 the rp-process stops at about ^{49}Mn (which decays to ^{49}Ti); at r_1 , at about ^{70}Br ; and at r_0 , at about ^{120}Ba . At r_0 and at r_1 , however, we will say that the rp-process stops at ^{68}Se (which decays to ^{68}Zn) because, as we stated in the last paragraph of §4, the long beta decay times prevent the rp-process from going much past ^{68}Se . Thus we have filled in the details behind the first two principles in §5.1.

We also stated in §5 that we needed to look at long-lived beta-decay parents which deposit energy beyond r_3 . We claimed there that the most dangerous species to deposit energy beyond r_3 is ^{22}Mg , and in the remainder of this Appendix we

TABLE 10

Reaction Rate Data for Proton Addition^a

process	time(s)
turbulent turnover	0.14
$^{19}\text{Ne}(p, \gamma)^{20}\text{Na}$	8×10^{-5}
$^{20}\text{Na}(p, \gamma)^{21}\text{Mg}$	2×10^{-4}
$^{21}\text{Na}(p, \gamma)^{22}\text{Mg}$	2×10^{-4}
$^{22}\text{Na}(p, \gamma)^{23}\text{Mg}$	2×10^{-4}
$^{23}\text{Mg}(p, \gamma)^{24}\text{Al}$	6×10^{-4}
$^{24}\text{Al}(p, \gamma)^{25}\text{Si}$	2×10^{-3}
$^{25}\text{Al}(p, \gamma)^{26}\text{Si}$	2×10^{-3}
$^{26}\text{Al}(p, \gamma)^{27}\text{Si}$	4×10^{-3}
$^{27}\text{Si}(p, \gamma)^{28}\text{P}$	4×10^{-3}
$^{28}\text{P}(p, \gamma)^{29}\text{S}$	1×10^{-2}
$^{29}\text{P}(p, \gamma)^{30}\text{S}$	1×10^{-2}
$^{30}\text{P}(p, \gamma)^{31}\text{S}$	1×10^{-2}
$^{31}\text{S}(p, \gamma)^{32}\text{Cl}$	3×10^{-2}
$^{32}\text{Cl}(p, \gamma)^{33}\text{Ar}$	8×10^{-2}
$^{33}\text{Cl}(p, \gamma)^{34}\text{Ar}$	8×10^{-2}
$^{34}\text{Cl}(p, \gamma)^{35}\text{Ar}$	7×10^{-2}
$^{35}\text{Ar}(p, \gamma)^{36}\text{K}$	2×10^{-1}
$^{36}\text{K}(p, \gamma)^{37}\text{Ca}$	5×10^{-1}
$^{37}\text{K}(p, \gamma)^{38}\text{Ca}$	5×10^{-1}
$^{38}\text{K}(p, \gamma)^{39}\text{Ca}$	5×10^{-1}

^a This is the mean time t_{+p} , as defined in equation (A6), for proton addition at radius $r_3 = 38.28$ km, $T = 0.6 \times 10^9$ K, $\rho = 30$ g cm⁻³ inside the envelope of Table 6.

shall substantiate that claim. We shall do so by estimating an upper bound to the luminosity deposited outside r_3 due to several beta-decay parents.

Consider first the beta decay of ^{22}Mg . The nucleus ^{22}Mg is created near r_1 and random walks about 5.57 s before decay. If it decays outside r_3 , the daughter nucleus can undergo further proton addition and burn up to ^{35}Ar (as we noted above), which decays to ^{35}Cl . We can estimate the energy deposited outside r_3 by ^{22}Mg by looking at the flux of ^{22}Mg past r_3 , $4\pi r_3^2 \rho_3 D_3 Y'_{22\text{Mg}}(r_3)$, and multiplying by the energy $E_{22\text{Mg}}$ released upon its decay and further burning to ^{35}Cl . $Y_{22\text{Mg}}$ is the function described in §5. The energy $E_{22\text{Mg}}$ is given by the total energy of burning ^{22}Na to ^{35}Cl less the energy that goes into neutrinos, which we estimate as half the energy of beta decays. Thus $E_{22\text{Mg}} \approx 90$ MeV, so that we have

$$L_{\text{Mg}22} = 4\pi r_3^2 \rho_3 D_3 Y'_{22\text{Mg}}(r_3) E_{22\text{Mg}} = 8600 L_{\odot}, \quad (\text{A12})$$

where $Y'_{22\text{Mg}}(r_3) = 1.77 \times 10^{-11}$ moles $\text{g}^{-1} \text{cm}^{-1}$.

Consider next the beta decay of ^{26}Si . Those ^{22}Mg that decay inside r_3 will quickly burn to ^{26}Si , which then can random walk out past r_3 before decaying and producing subsequent burning. To estimate the amount of energy ^{26}Si thereby deposits outside r_3 , we can consider an imaginary species created at r_0 with mean lifetime $5.57 + 3.17$ s (the sum of the ^{22}Mg and ^{26}Si lifetimes). We determine Y_{imag} subject to $Y_{\text{imag}}(r_{\text{ph}}) = 0$ and $Y'_{\text{imag}}(r_0) = -Y'_{12\text{C}}(r_0)$. Then

$$L_{\text{Si}26} = 4\pi r_3^2 \rho_3 D_3 [Y'_{\text{imag}}(r_3) - Y'_{22\text{Mg}}(r_3)] E_{26\text{Si}} = 230 L_{\odot}, \quad (\text{A13})$$

where $Y'_{\text{imag}}(r_3) = 1.84 \times 10^{-11}$ mol $\text{g}^{-1} \text{cm}^{-1}$ and $E_{26\text{Si}} = 63$ MeV. In this expression we take the difference in brackets in order to avoid twice counting energy taken out by ^{22}Mg .

Last, consider some of the longer-lived beta-unstable isotopes which deposit their beta decay energy outside r_3 , such as ^{68}Se and ^{81}Zr . We use the functions Y_i which were computed in §4, and set the energies released to half the beta decay energy. Then

$$L_{\text{Se}68} = 4\pi r_3^2 \rho_3 D_3 Y'_{68\text{Se}}(r_3) E_{68\text{Se}} = 210 L_{\odot}, \quad (\text{A14})$$

where $Y_{\text{ssSe}}(r_3) = 1.69 \times 10^{-11} \text{ mol g}^{-1} \text{ cm}^{-1}$ and $E_{\text{ssSe}} = 2.3 \text{ MeV}$. Also

$$L_{\text{Zr81}} = 4\pi r_3^2 \rho_3 D_3 Y'_{\text{s1Zr}}(r_3) E_{\text{s1Zr}} = 220 L_{\odot}, \quad (\text{A15})$$

where $Y_{\text{s1Zr}}(r_3) = 9.34 \times 10^{-12} \text{ mol g}^{-1} \text{ cm}^{-1}$ and $E_{\text{s1Zr}} = 5 \text{ MeV}$. Other species are even less dangerous than these. All the other species deposit $\lesssim 10\%$ of the energy that ^{22}Mg deposits beyond r_3 , and so we will use just ^{22}Mg as an indicator of how much luminosity is deposited beyond r_3 . Synthesizing these concepts, we arrive at the set of assumptions spelled out in the second to last paragraph of §5.1.

A.3. Hot CNO cycle

In this subsection we shall give the details of idealizations of the hot CNO cycle which lead to the simplified network in Table 1B. Most of our idealizations will go in the direction of increasing the efficiency of the hot CNO cycle, so that when we find that $L_{\text{nuc}}/L_{\text{ph}}$ is much less than 1, we will know that the full hot CNO cycle would not lead to a consistent model.

The usual summary of the reactions of the hot CNO cycle (Audouze, Truran, and Zimmermann 1973) is given by (A1). For the purpose of determining if the hot CNO network provides enough energy to maintain an extended envelope, we can ignore most of the side reactions. An exception is the branch (A2) occurring at higher temperatures ($T \gtrsim 5 \times 10^8$) which bypasses the long ^{14}O decay (102 s). By comparison, ^{18}Ne has a decay time of 2.41 s.

We will simplify the hot CNO cycle by saying that the strong reactions all occur instantaneously at r_0 (so we will ignore strong reaction intermediates, such as ^{13}N) and, because the ^{18}Ne decay is much faster than the ^{15}O decay, that the ^{18}Ne decay occurs instantaneously. It is enough, therefore, to determine the functions $Y_{12\text{C}}$ (the initial seed), $Y_{15\text{O}}$ (a long-beta-decay parent), and $Y_{15\text{N}}$ (its daughter), with the boundary conditions given in equations (5) and (8). This is the simplified reaction network used in §4 and given in Table 1B.

REFERENCES

- Arnett, W. D. & Bowers, R. L. 1977, *ApJS*, **33**, 415.
- Audouze, J., Truran, J. W., & Zimmermann, B. A. 1973, *ApJ*, **184**, 493.
- Baym, G., Bethe, H. A., & Pethick, C. 1971, *Nucl. Phys.*, **A175**, 225.
- Baym, G., Pethick, C., & Sutherland, P. 1971, *ApJ*, **170**, 299 .
- Bollmark, P., Lindren, B., Rydh, B., & Sassenberg, U. 1978, *Phys. Scripta*, **17**, 561.
- Bollmark, P., Lindren, B., & Sassenberg, U. 1980, *Phys. Scripta*, **21**, 811.
- Cameron, A. G. W., & Iben, I. 1986, *ApJ*, **305**, 228.
- Cannon, R. C., Eggleton, P. P., Żytkow, A. N., & Podsiadlowski, P. 1992, *ApJ*, **386**, 206.
- Caughlin, G. R. & Fowler, W. A. 1988, *Atomic Data Nucl. Data Tables*, **40**, 283.
- Cox, J. P. & Giuli, R. T. 1968, *Principles of Stellar Structure* (New York: Gordon and Breach).
- Despain, K. H. 1976, Ph.D. thesis, California Institute of Technology, Pasadena.
- Eich, C., Zimmermann, M. E., Thorne, K. S., & Żytkow, A. N. 1989, *ApJ*, **346**, 277.
- Gamow, G. 1937, *Structure of Atomic Nuclei and Nuclear Transformations* (Oxford: Oxford Univ. Press), 237.
- Herzberg, G. 1950, *Spectra of Diatomic Molecules* (Princeton: Van Nostrand).
- Hut, P., & Paczyński, B. 1984, *ApJ*, **284**, 675.
- Landau, L. D. 1937, *Dokl. Akad. Nauk SSSR*, **17**, 301 [English transl. in *Nature*, **141**, 333 (1938)].
- Lederer, C. M., & Shirley, V. S. 1978, *Table of Isotopes* (7th ed.; New York: Wiley).

- Myers, W. D., & Swiatecki, W. J. 1966, *Nucl. Phys.*, **81**, 1.
- Paczyński, B. 1969, *Acta Astr.*, **19**, 1.
- Pandharipande, V. 1971, *Nucl. Phys.*, **A178**, 123.
- Pandharipande, V., & Smith, R. A. 1975, *Nucl. Phys.*, **A237**, 507.
- Ray, A., Kembhavi, A. K., & Antia, H. M. 1987, *A&A*, **184**, 164.
- Rosen, B. 1970, in *International Tables of Selected Constants, Vol. 17, Spectroscopic Data relative to Diatomic Molecules* (Oxford: Pergamon).
- Svenson, E. 1929, *Zs. Phys.*, **59**, 333.
- Taam, R. E. 1979, *Ap. Letters*, **20**, 29.
- Taam, R. E., Bodenheimer, P., & Ostriker, J. P. 1978, *ApJ*, **222**, 269.
- Takahashi, K., Yamada, M., & Kondoh, T. 1973, *Atomic Data Nucl. Data Tables*, **12**, 101.
- Thorne, K. S., & Żytkow, A. N. 1977, *ApJ*, **212**, 832.
- Wallace, R. K., & Woosley, S. E. 1981, *ApJS*, **45**, 389.
- Watson, W. W., & Fredrickson, W. R. 1932, *Phys. Rev.*, **39**, 765.
- Woosley, S. E., Fowler, W. A., Holmes, J. A., & Zimmermann, B. A. 1978, *Atomic Data Nucl. Data Tables*, **22**, 371.
- Woosley, S. E., Holmes, J. A., Fowler, W. A., & Zimmermann, B. A. 1975, *Orange Aid Preprint 422* (Pasadena: Kellogg Radiation Laboratory, Caltech).
- Zimmermann, M. E. 1979, Ph.D. thesis, California Institute of Technology, available as *Orange Aid Preprint 586* (Pasadena: Kellogg Radiation Laboratory, Caltech).

Chapter 3

Calculation of Beta-Decay Halflives
of Proton-Rich Nuclei of Intermediate Mass*Garrett T. Biehle and Petr Vogel**Intermezzo*

This chapter originally appeared as *Physical Review C*, 46, 1555 (1992).

Ever since Takahashi *et al.* (1973) calculated estimates for the beta-decay halflives of virtually all beta-unstable nuclei, there has been a large effort to improve these estimates for neutron-rich nuclei because of applications in r-process theory and in the fate of fission products (see Staudt *et al.* 1990). The theoretical effort to improve the estimates of halflives of proton-rich nuclei has not been commensurate, although Hirsch *et al.* (1991) and Muto *et al.* (1991) presented calculations for light nuclei ($Z \leq 30$). (See, however, also Suhonen 1991, Borzov *et al.* 1990, and Staudt *et al.* 1990.) In this report we present the results of an effort to improve the estimates for halflives of several proton-rich nuclei of intermediate mass. These halflives play a role in rp-process theory (Wallace and Woosley 1981), that is, the process in which protons are quickly added onto C, N, O, and other “metals” with intervening fast positron decays resulting in heavy proton-rich nuclei. This process occurs in certain astrophysical contexts in which the temperature is greater than about 5×10^8 K. In particular, this process is predicted to occur in massive stars with degenerate neutron cores (if they exist) (Biehle 1991, i.e., Chapter 2 of this thesis), and information about the longer-lived (> 1 s) beta-unstable nuclei would allow one to predict the nuclear abundances on the surfaces of these stars. For this reason we undertook the calculation of halflives of some proton-rich even-even nuclei of intermediate mass.

We are interested in even-even nuclei which have 0^+ ground states, so that the calculation is relatively simple. The positron-decay half-life $t_{\frac{1}{2}}$ is given by the following formula:

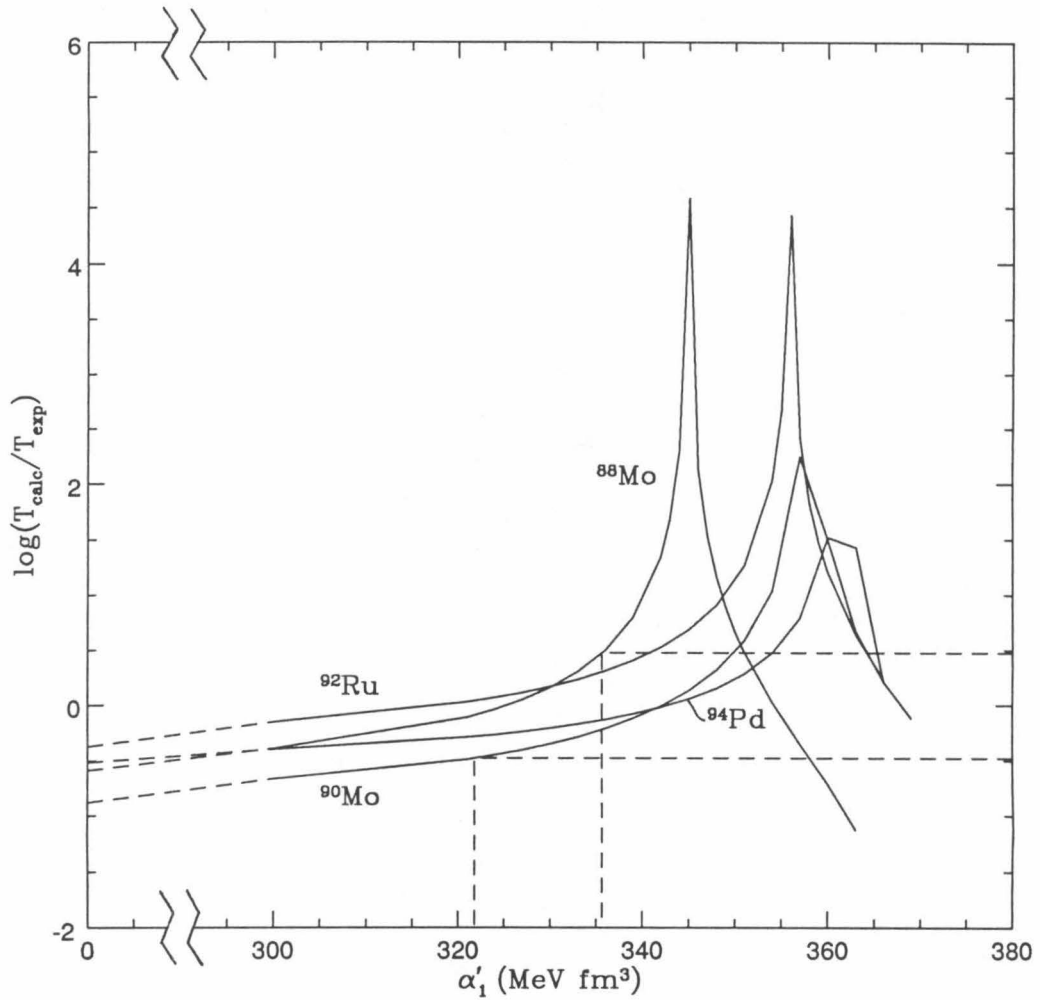
$$\frac{1}{t_{\frac{1}{2}}} = \sum_m \frac{B(GT)_m g_A^2}{6160 \text{ s}} f(\Delta E_m, Z), \quad (1)$$

where m labels the accessible 1^+ states in the daughter nucleus, $B(GT)_m$ is the Gamow-Teller β^+ strength (equivalent to $|\langle m | \sigma \tau^+ | i \rangle|^2$ in this case), g_A is the axial-vector-current coupling constant (which we set to 1.25), and $f(\Delta E_m, Z)$ is the Fermi function (including Coulomb and relativistic corrections), which describes the size of phase space.

We obtain energy levels of the daughter nucleus and evaluate $B(GT)$ using the random phase approximation based on the quasiparticle formalism (QRPA).

(The generalization of the QRPA to charge-changing modes is due to Halbleib and Sorensen 1967. Particle-particle interactions were first included in the QRPA by Cha 1983.) The formalism is described in detail in Vogel and Zirnbauer (1986) and in Engel *et al.* (1988). In these papers the authors use the δ -force as the residual interaction and describe the following four parameters: α_0 , α_1 (the particle-hole interaction constants in the $S = 0$ and $S = 1$ channels, respectively), α'_0 , and α'_1 (the particle-particle interaction constants). Although these constants are theoretically related, the authors present an argument that they can be treated independently in this calculation. Using the values given in Engel *et al.* (1988), we set $g_{\text{pair}} = -270 \text{ MeV fm}^3$ when we solve the BCS equations, and we set $\alpha_0 = -890 \text{ MeV fm}^3$ and $\alpha_1 = -1010 \text{ MeV fm}^3$ for the RPA portion of our calculations. Because we are looking at positron decay of proton-rich nuclei, our results do not depend on α'_0 in the RPA calculations. Our results do, however, depend strongly on the value of α'_1 , so we must take care to choose it carefully.

We divide the nuclei into two categories those with $74 \leq A \leq 80$ and those with $80 < A \leq 96$. For the heavier nuclei in our study, we calibrated α'_1 using the known decay halflives of ^{88}Mo , ^{90}Mo , ^{92}Ru , and ^{94}Pd . In order to calculate these halflives, we identified the lowest lying 1^+ state in the daughter nucleus with the ground state given by the QRPA calculation. (This determines the values of ΔE_m , used in the phase space integrals.) Our calculation is for positron-decay only, i.e., no electron capture. In three of the calibration nuclei positron-decay dominates over electron capture; however, 75% of the decay of ^{90}Mo is due to electron capture. In that case we, therefore, use the proper partial decay rate. In our calculation, almost all ($\gtrsim 90\%$) of the predicted decays occur into the lowest lying 1^+ state. Figure 1 shows the log (base 10) of the ratio of calculated positron-decay half-life to experimental half-life versus α'_1 . From this figure we see that α'_1 may be anywhere within a window from -324 MeV fm^3 to -333 MeV fm^3 and yield values of halflives correct to within a factor of 3. A value of $\alpha'_1 = -329 \text{ MeV fm}^3$ yields a least χ^2_{red} equal to 0.22, where $\chi^2_{\text{red}} = \left[\frac{1}{3} \sum (\log(T_{\text{calc}}/T_{\text{exp}}))^2 \right]^{1/2}$. Thus we predict that our results in Table 1 are accurate to about a factor of



$\log_{10}(T_{\text{calc}}/T_{\text{exp}})$, where T refers to the positron-decay half-life, versus α'_1 the particle-particle interaction strength. The window of values for α'_1 which yield results correct to within a factor of 3 is shown. Note that ignoring the residual particle-particle interaction (i.e., setting α'_1 to 0) results in prediction of half-lives approximately 3 to 10 times too small.

TABLE 1
 Predicted Beta-Decay Halflives

nucleus	$\Delta E_{m=0}^a$ (MeV)	halflife ^b (s)	Takahashi <i>et al.</i> halflife(s)
⁷⁴ Sr	9.6	0.5	0.03
⁷⁶ Sr	4.5	8	3
⁷⁸ Zr	10.5	0.06	0.03
⁸⁰ Zr	5.0	7	3
⁸⁴ Mo	5.2	6	0.8
⁸⁶ Mo	3.9	90	16
⁸⁸ Ru	5.8	1.2	0.8
⁹⁰ Ru	4.7	16	5
⁹² Pd	6.8	0.9	0.4
⁹⁶ Cd	8.0	0.6	0.3

^a This is the maximum total energy of the positron for a transition to the lowest 1^+ daughter state.

^b The estimated accuracy is a factor of 2. See the explanation in the text.

$10^{0.22} = 1.7$. By comparison, the χ^2_{red} for these four nuclei using results from Takahashi *et al.* (1973) is 0.59, yielding an estimated accuracy of a factor of $10^{0.59} = 4$.

In order to calculate halflives of the nuclei listed in Table 1, we need to know the positron-decay energies. Since the masses of the positron-decay parents (and often those of the daughters as well) are not known, we use the predicted masses of Jänecke and Masson (1988). (These seem to reproduce best the known masses of proton-rich nuclei.) We set $\Delta E_{m=0}$, that is, the maximum total energy of the positron, to the difference of parent and daughter masses less 0.2 MeV. The 0.2 MeV represents a typical value for the energy difference between the ground state and the lowest lying 1^+ state of the daughter nucleus. (For these decays, however,

$\Delta E_{m=0}$ is large enough that the correction is trivial.) The results are shown in Table 1. As stated in the previous paragraph, these values are accurate to within a factor of about 2. Electron capture is negligible in these nuclei, contributing less than 3% because of the large decay energies involved. (See Lederer and Shirley 1978.)

Similarly we use the known halflives of ^{70}Se , ^{72}Kr , ^{74}Kr , and ^{80}Sr to calibrate α'_1 and calculate halflives for several nuclei with $A \leq 80$. In this case we obtain $\alpha'_1 = -327 \text{ MeV fm}^3$ for the best fit, yielding a least χ^2_{red} equal to 0.32. The results are also shown in Table 1. We estimate that the results are accurate to within a factor of about $10^{0.32} = 2$, and again electron capture is negligible.

Also shown in Table 1 are the predicted halflives of Takahashi *et al.* (1973). It is encouraging that our results are consistent with theirs, which are calculated by a different method; most of the difference is due to different Q-values (i.e., $\Delta E_{m=0}$), especially in the case of ^{74}Sr .

The authors wish to acknowledge support from National Science Foundation Grant AST-8817792 and U. S. Department of Energy contract no. DE-F603-40397.

REFERENCES

- Biehle, G. T. 1991, *ApJ*, **380**, 167.
- Borzov, I. N., Trykov, E. L., & Tayans, S. A. 1990, *Sov. J. Nuc. P.*, **52**, 627.
- Cha, D. 1983, *Phys. Rev. C*, **27**, 2269; Ph.D. thesis, Michigan State University, 1982.
- Engel, J., Vogel, P., & Zirnbauer, M. R. 1988, *Phys. Rev. C*, **37**, 731.
- Halbleib, J. A., & Sorensen, R. A. 1967, *Nucl. Phys.*, **A98**, 542.
- Hirsch, M., Staudt, A., Muto, K., & Klapdor-Kleingrothaus, H. V. 1991, *Nucl. Phys.*, **A535**, 62.
- Jänecke, J., & Masson, P. J. 1988, *Atomic Data Nucl. Data Tables*, **39**, 265.
- Lederer, C. M., & Shirley, V. S. 1978, *Table of Isotopes* (7th ed.; New York: Wiley); see Appendix 21.
- Muto, K., Bender, E., & Oda, T. 1991, *Phys. Rev. C*, **43**, 1487.
- Staudt, A., Bender, E., Muto, K., Klapdor-Kleingrothaus, H. V. 1990, *Atomic Data Nucl. Data Tables*, **44**, 79.
- Staudt, A., Hirsch, M., Muto, K., & Klapdor-Kleingrothaus, H. V. 1990, *Phys. Rev. Lett.*, **65**, 1543.
- Suhonen, J. 1991, *Phys. Lett. B*, **255**, 159.
- Takahashi, K., Yamada, M., and Kondoh, T. 1973, *Atomic Data Nucl. Data Tables*, **12**, 101.
- Vogel, P., & Zirnbauer, M. R. 1986, *Phys. Rev. Lett.*, **57**, 3148.
- Wallace, R. K., & Woosley, S. E. 1981, *ApJS*, **45**, 389.

Chapter 4

Observational Prospects for Massive Stars
with Degenerate Neutron Cores

Garrett T. Biehle

Allegro

This chapter has been submitted to *Astrophysical Journal*.

1. Introduction and summary

In the 1930s Landau (1937) and Gamow (1937) independently proposed the possibility of stars having degenerate neutron cores; however, forty years would pass before detailed models of such stars were worked out (Thorne and Żytkow 1977, hereafter TŻ; Bisnovatyi-Kogan and Lamzin 1984; Eich *et al.* 1989; Biehle 1991, hereafter Paper I; Cannon *et al.* 1992; Cannon 1992). [Paper I is Chapter 2 in this thesis.] Although these models certainly do not apply to the sun (as Landau and Gamow proposed) or indeed to any stage in single star evolution, it is possible that stars with degenerate neutron cores (or Thorne-Żytkow objects, or TŻOs) form in other contexts. Three scenarios have been proposed: In the first scenario TŻOs may result from the collision of a neutron star and a normal star in a globular cluster (see Ray, Kembhavi, and Antia 1987). This would form light TŻOs. In the other two scenarios the TŻO is a stage in the evolution of a close binary system. In the second, the initially more massive star evolves first, transferring much of its envelope onto the companion and eventually becoming a neutron star in a supernova. When the companion exhausts its hydrogen fuel and begins to expand, it swallows up the neutron star, which then spirals to the center, forming a TŻO. (See §3 of this paper and §1 of Cannon *et al.* 1992 for a more detailed discussion.) In the third scenario, a supernova in a binary system “kicks” the forming neutron star into its companion (Leonard, Hills, and Dewey 1993). In addition, TŻOs have been invoked to describe a creation scenario for low-mass X-ray binaries (Eggleton and Verbunt 1986). And recently they have been proposed as a source of p-process nuclei (Cannon 1992).

To date, however, no star has been identified as a TŻO. This is because TŻOs look much like normal red giants or red supergiants, only slightly redder. In this paper we develop the idea that such a star might be identifiable by peculiar nuclear abundances on its surface (TŻ). We present predictions for the surface abundances (Tables 1 and 2) of the more massive TŻOs and list some spectral lines for determining abundances in candidate stars (Table 3).

In their paper TŻ constructed spherically symmetric, nonrotating, nonmag-

netic, fully general relativistic models which naturally fall into two classes: T \dot{Z} giants and T \dot{Z} supergiants. The models for the former class describe stars with a core mass of $1 M_{\odot}$ and total mass less than $9 M_{\odot}$. Gradual, steady accretion of the envelope onto the core accounts for almost all the luminosity, while nuclear burning makes a small contribution.

The models for T \dot{Z} supergiants describe stars with core mass $1 M_{\odot}$ and total mass greater than $12 M_{\odot}$. (Cannon 1992 argues that this lower bound should be $14 M_{\odot}$.) These stars have the following properties: Nuclear burning provides most of the luminosity ($\sim 90\%$). The envelope is almost entirely convective, so that the convection includes the nuclear burning region and extends to the surface of the star. From the outside this star would look like a spectral type M I star, i.e., a red supergiant.

These properties of the T \dot{Z} supergiant model imply that products from the nuclear burning region are convected to the surface of the star. In Paper I we showed that the nuclear burning in T \dot{Z} supergiants proceeds by the rp-process (i.e., rapid-proton-process, see Wallace and Woosley 1981), in which a nuclear seed (initially C, N, and O) undergoes alternately proton addition and positron decay until heavy elements are produced ($Z \gtrsim 26$). The scene near the burning region looks like the following: Convection carries a seed nucleus down into the burning region at the base of the envelope. The seed quickly burns (mainly by proton addition) to a proton-rich species at the effective proton drip line (at $T \sim 10^9$ K). Since no further proton addition can occur, convection sweeps the seed back out into the envelope where it random-walks around (because of convection) until it undergoes positron decay. If the decay time is short, not many times the timescale of convective turnover, then the seed decays at a small radius and is likely to be carried back down to the burning region to be burned again. If the decay time is long, then the seed decays at a large radius and is likely to be carried to the surface of the star where its daughter endproduct can be seen. This endproduct is the stable or long-lived (> 1000 yr) daughter after a series of positron decays.

In §2 we make this description quantitative by modifying the formalism which

was presented in Paper I. The reaction network in that paper, although sufficiently accurate to predict the energetics of the star, was not accurate enough to predict surface abundances. We remedy this deficiency in §2.1, producing a simplified rp reaction network which is good enough to predict the abundances of the major species on the surface. (See Cannon 1992 for a calculation which includes time dependence and a full rp reaction network.) In §2.2 we present the formalism which yields the fluxes of peculiar species (rp products) to the surface. We thus predict surface abundances in Tables 1 and 2 of §2.3. Not surprisingly, the species which are most represented are those associated with the rp-process “waiting points”, particularly the semi-magic and nearly semi-magic nuclei with $Z \approx 50$. The rp-process slows down at this point and the resulting decay products are carried to the surface of the star. In particular the abundances of Br, Rb, Y, and Nb are enhanced by a factor of 200 over solar abundances; and that of Mo (and perhaps of Ru, Rh, Pd, and Ag), by a factor of 1000. This provides a strong distinction between “normal” red supergiants and those with degenerate neutron cores.

In §3 we briefly discuss the problems involved in determining surface abundances from absorption spectra in red supergiants and present a list of lines which should prove useful in obtaining abundances of several elements. In §4 we estimate the number of $T\dot{Z}$ supergiants in the solar neighborhood. This we do in several ways because the lifetimes of the progenitors (high-mass X-ray binaries) are uncertain. We find that of the ~ 100 red supergiants within 5 kpc, perhaps several are $T\dot{Z}$ supergiants. §5 contains a brief conclusion.

2. Surface nuclear abundances

2.1. Reaction network

In order to obtain predictions for surface abundances of $T\dot{Z}$ supergiants, we first obtain a more nearly accurate reaction network than that used in Paper I. To do this we use more accurate atomic masses in the formalism presented in the Appendix of Paper I. We obtain atomic mass estimates from the NNDC

(National Nuclear Data Center) where available. We especially note the mass of ^{57}Cu (Gagliardi *et al.* 1986) and that of ^{58}Zn (Seth *et al.* 1986). Where experimental masses are not available we use semi-empirical mass estimates of Jänecke and Masson (1988), since these are accurate to ± 0.15 MeV for nearby known proton-rich intermediate-mass nuclei.

As in Paper I proton-addition rates are taken from Woosley *et al.* (1978) where available, or else from Caughlin and Fowler (1988) or from the Hauser-Feshbach theory (eq. [30] of Woosley *et al.* 1975). The reaction rates for nuclei with $Z < 44$ are calculated assuming $T = 1.3 \times 10^9$ K and $\rho = 440$ g cm $^{-3}$ (the conditions in the envelope at which breakout from the hot CNO cycle becomes fast compared to the convective turnover timescale). Those for nuclei with $44 \leq Z < 50$ are calculated assuming $T = 1.7 \times 10^9$ K and $\rho = 1200$ g cm $^{-3}$, and those for nuclei with $Z \geq 50$ are calculated assuming $T = 2.1 \times 10^9$ K and $\rho = 2700$ g cm $^{-3}$. We do this because the reactions involving more highly charged nuclei turn on only in the hotter regions of the envelope.

We take positron-decay halflives from the NNDC where available. For ^{102}Sn , we refer to Barden *et al.* (1988). For ^{76}Sr , ^{80}Zr , ^{84}Mo , ^{88}Ru , and ^{92}Pd , we refer to Biehle and Vogel (1992). For ^{50}Fe , ^{54}Ni , ^{63}Ge , ^{67}Se , ^{75}Sr , ^{78}Y , ^{85}Mo , ^{89}Ru , and ^{93}Pd , we refer to Takahashi *et al.* (1973), except that we use Q-values calculated from Jänecke and Masson (1988), in accordance with the method given in Takahashi *et al.* (1973).

The resulting reaction network is shown in Figure 1, which supersedes the reaction network in the Appendix of Paper I. We especially note that, because of shell effects, Ni and Sn stand out as waiting points in Figure 1. Also, the isotopes of Sn have comparatively long halflives, so that we expect there to be large abundances on the stellar surface of endproducts from the positron decays of these isotopes.

Because of uncertainties in the nuclear masses, this prescription is not sufficient, however, to decide the dominant species in two of the equilibria (Appendix

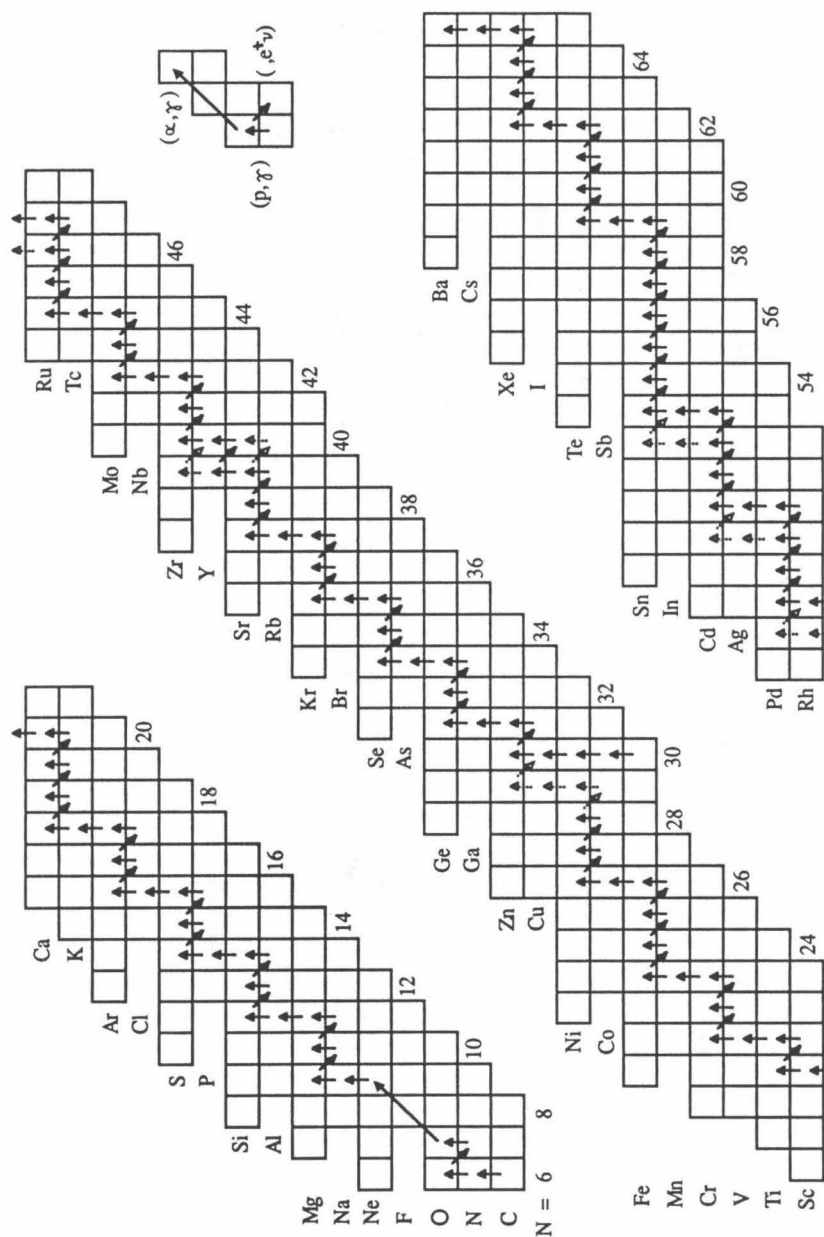
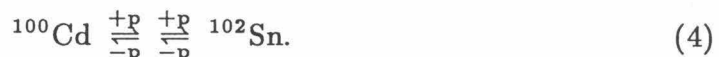


Fig. 1—Simplified rp-network used in §2. The CNO network and breakout into the rp-process are shown schematically by a few representative reactions. In §2 they are idealized as happening quickly. Note the waiting points due to shell effects for $Z \approx 28$ and especially $Z \approx 50$. The rp-process comes virtually to a halt at ^{56}Ni since this nucleus is double magic (two closed shells), so that a dashed arrow shows the reaction $^{56}\text{Ni}(p, \gamma)^{57}\text{Cu}$ (see §2.2). About half of the seed which continues the rp-process comes from “primordial” Fe, as shown. In other places in the diagram where there are dashed arrows, the nuclear data is insufficient to determine definitely the correct reaction pathway, and so both possibilities are worked out in Tables 1 and 2.

of Paper I). The equilibrium involving nuclei with $N = 39$:



is very sensitive to the temperature at which it is established. We will assume that ${}^{78}\text{Y}$ predominates, although Tables 1 and 2 contain also results obtained by assuming that either ${}^{77}\text{Sr}$ or ${}^{79}\text{Zr}$ predominates. We treat the following equilibria involving nuclei with $N = 46, 49$, and 52 , respectively, in the same way:



Generally, however, we will assume that ${}^{90}\text{Ru}$, ${}^{95}\text{Pd}$, and ${}^{100}\text{Cd}$, respectively, dominate these equilibrium. We include results which come from different assumptions about the nuclear physics in order to show how sensitive our predictions are to the uncertainties in the input nuclear physics. The equilibrium involving ${}^{56}\text{Ni}$ (i.e., the equilibrium among species with $N = 28$) deserves special consideration, as discussed at the end of §2.2.

2.2. Formalism

As a first step in predicting the surface abundances of nuclear species, we construct a steady-state model in which the abundances on the surface are constant and equal to their Population I abundances. In the context of this model we determine the distribution of nuclear species throughout the envelope, and in particular we determine the flux of various exotic nuclear species toward the surface of the star from the burning region. In §2.3 we will relax the assumption of constant surface abundances and present predictions based on the fluxes calculated in this section.

A steady-state model for the distribution of nuclear species in the envelope was worked out in §4 of Paper I, so in this section we will briefly discuss the assumptions made in that model and present the modifications necessary to obtain

the results in §2.3. We make an approximation investigated by Despain (1976) which is based on the mixing length theory of diffusion. In particular, the nuclear abundances Y_i (in moles g^{-1}) of species i are given by the following modified diffusion equation:

$$0 = \frac{\partial Y_i}{\partial t} = \frac{1}{\rho r^2} \frac{\partial}{\partial r} \left(r^2 \rho D \frac{\partial Y_i}{\partial r} \right) - \beta_i Y_i + \beta_j Y_j, \quad (5)$$

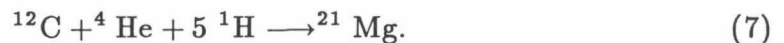
where D is a generalized diffusion coefficient which is set to $v_{\text{turb}} l_{\text{pres}}$, v_{turb} is the large-scale turbulent (convective) velocity, and l_{pres} is the pressure scale height. We are assuming that species j decays into species i with time constant β_j and that species i decays with time constant β_i .

Equation (5), with i running over the various species, is a set of coupled ordinary differential equations which must be augmented with boundary conditions. The boundary conditions at the base of the envelope are determined by the reaction network, as described in §4.1 (eq. [9]) of Paper I. In the steady-state approximation we assume that the abundances on the surface of the star are constant and equal to their Population I abundances, except that we lump C, N, and O into ^{12}C :

$$Y_{^{12}\text{C}}(r_{\text{ph}}) = (Y_{^{12}\text{C}} + Y_{^{14}\text{N}} + Y_{^{16}\text{O}})_{\text{Pop I}} \equiv Y_{\text{seed}}, \quad (6a)$$

$$Y_i(r_{\text{ph}}) = (Y_i)_{\text{Pop I}}, \quad (6b)$$

where r_{ph} is the radius of the photosphere, and abundances are taken from Anders and Grevesse (1989). The model in this section differs from that in §4 of Paper I in three ways: 1) We do not lump all the “metals” into ^{12}C but use equation (6). 2) We consider beta decays of all nuclei more massive than ^{21}Mg , not just the decays of those with long halflives. 3) We idealize the breakout reaction (responsible for breakout from the CNO cycle) and subsequent proton-addition as happening quickly:



As in Paper I, all of the strong reactions are idealized as occurring at the base of the envelope, whereas the beta decays occur anywhere in the envelope. These

assumptions are sufficient to specify the boundary conditions at the base of the envelope for equation (5).

We calculate the fluxes of species out of the burning region as follows: Consider first the burning products from burning only C, N, and O. From §4.3 of Paper I, we know that the flux of C, N, and O (which we lump into ^{12}C) into the burning region is given by

$$F_{^{12}\text{C}}(r_0) = 4\pi r_0^2 \rho_0 D_0 Y_{\text{seed}} \eta_s, \quad (8)$$

where ρ_0 and D_0 are the values of ρ and D at r_0 , the radius at the base of the envelope (i.e., the radius of the core), and $\eta_s (\approx 1.25 \times 10^{-8} \text{ cm}^{-1})$ is a constant defined in Paper I, of no importance in this paper. This flux in equation (8) is also equal to the flux of ^{21}Mg out of the burning region, since we are idealizing the breakout reaction (7) as occurring quickly. After ^{21}Mg convects into the envelope and decays to ^{21}Na , the flux of ^{21}Na into the burning region is given by

$$F_{^{21}\text{Na}}(r_0) = 4\pi r_0^2 \rho_0 D_0 Y_{\text{seed}} \eta_s \zeta_{^{21}\text{Mg}}, \quad (9)$$

where $\zeta_{^{21}\text{Mg}}$, defined in §4 of Paper I, depends only on the halflife of ^{21}Mg (and on the physical parameters of the envelope) and is called the “hindrance factor”. It can be thought of as the amount of “damage” done by the required decay of ^{21}Mg , since $\zeta_{^{21}\text{Mg}}$ gives the fraction of the daughter species ^{21}Na which makes it back to the burning region. Conversely, the flux of ^{21}Na outward to the surface of the star is given by

$$F_{^{21}\text{Na}}(r) = 4\pi r^2 \rho D Y_{\text{seed}} \eta_s (1 - \zeta_{^{21}\text{Mg}}), \quad (10)$$

where $r_0 \ll r \ll r_{\text{ph}}$ and r_{ph} is the radius of the photosphere. Here ρ and D are functions of r , but $F_{^{21}\text{Na}}$ is nearly constant if $r \gg r_0$ (so that the positron decays are completed). (However, ^{21}Na is not stable but decays to ^{21}Ne , so that eq. [7] actually gives the flux of ^{21}Ne toward the surface of the star.)

After ^{21}Na is burned to ^{22}Mg in the burning region, and that ^{22}Mg decays to ^{22}Na in the envelope, the flux of ^{22}Na back into the burning region is given by

$$F_{^{22}\text{Na}}(r_0) = 4\pi r_0^2 \rho_0 D_0 Y_{\text{seed}} \eta_s \zeta_{^{21}\text{Mg}} \zeta_{^{22}\text{Mg}}, \quad (11)$$

and the flux of ^{22}Na (or rather ^{22}Ne) toward the surface of the star is given by

$$F_{22\text{Na}}(r) = 4\pi r^2 \rho D Y_{\text{seed}} \eta_s \zeta_{21\text{Mg}} (1 - \zeta_{22\text{Mg}}), \quad (12)$$

where $r_0 \ll r \ll r_{\text{ph}}$. In general the flux of any positron-decay daughter to the surface is given by

$$F_{\text{D},k} = 4\pi r^2 \rho D Y_{\text{seed}} \eta_s \left[\prod_{i=0}^{k-1} \zeta_i \right] (1 - \zeta_k), \quad (13)$$

where $r_0 \ll r \ll r_{\text{ph}}$, and we set ζ_0 to 1 (*cf.* eq. [18] in Paper I). The subscript k refers to the value in column (1) of Table 1.

So far we have only been considering the original C, N, and O which gets convected to the burning region, i.e., equation (6a). Addition of the other species in equation (6b) does not complicate the formalism, in that all the new stable species are treated in the same way as ^{12}C in the previous two paragraphs, except that they are injected later in the rp-process. The fluxes of the burning products from all these “fuels” are added together, and these sums of outward fluxes are used in §2.3.

The equilibrium involving ^{56}Ni ,



deserves special attention. The halflife of ^{56}Ni is so long (6.10 d) that, after its decay, very little ($\zeta_{56\text{Ni}} \sim 0.002$) gets convected back to the burning region. Also the above equilibrium is shifted far to the left, so that

$$\frac{Y_{57\text{Cu}}}{Y_{56\text{Ni}}} \approx 2 \times 10^{-4}, \quad (15)$$

where we used $\rho = 270 \text{ g cm}^{-3}$ and $T = 1.12 \times 10^9 \text{ K}$ (see Appendix of Paper I). Nevertheless the small amount of ^{57}Cu that is in the burning region has such a short halflife (233 ms, or mean lifetime 0.34 s) that some of it has time to decay before it is swept into the cooler portions of the envelope, where the rp-process cannot continue. After the decay of ^{57}Cu , the equilibrium (14) shifts again to

the right to produce more ^{57}Cu . The result of this is that about 5% of the ^{56}Ni which gets created at the burning region gets further processed to ^{57}Ni (from the decay of ^{57}Cu) and continues the rp-process. We can set the hindrance factor $\zeta_{^{56}\text{Ni}}$ to an effective value of $\zeta_{\text{eff}} = 0.05$. Thus about 95% of the ^{56}Ni which gets created escapes to the surface of the star. Much of the seed which gets processed to elements heavier than Fe comes from primordial ^{56}Fe .

[To get $\zeta_{\text{eff}} = 0.05$, we need to compare the rate (in moles/s) that ^{57}Cu decays to ^{57}Ni , $dN_{^{57}\text{Ni}}/dt$, to the rate that ^{56}Ni is convected out of the burning region

$$F_{^{56}\text{Ni}} = 4\pi r_0^2 \rho_0 D_0 Y'_{^{56}\text{Ni}}(r_0), \quad (16)$$

using notation from §4 of Paper I. We note that

$$\frac{dN_{^{57}\text{Ni}}}{dt} \approx M_{\text{hot}} Y_{^{56}\text{Ni}} \frac{Y_{^{56}\text{Ni}}}{Y_{^{56}\text{Ni}}} \frac{1}{\tau_{^{57}\text{Cu}}}, \quad (17)$$

where M_{hot} is the mass of that portion of the envelope which is hot and dense enough to maintain the equilibrium (14), and $\tau_{^{57}\text{Cu}}$ is the mean lifetime of ^{57}Cu , which is 0.34 s. Using Hauser-Feshbach reaction rates (Woosley *et al.* 1975) we obtain that the radius at which the envelope becomes too cool to maintain the equilibrium is about $r_{\text{hot}} \approx 22$ km. Thus we obtain

$$M_{\text{hot}} \approx 4\pi \rho_0 r_0^3 \ln(r_{\text{hot}}/r_0), \quad (18)$$

where we have used the approximation $\rho = \rho_0 (r_0/r)^3$. According to the definition of $\eta_{^{56}\text{Ni}}$, we have

$$Y_{^{56}\text{Ni}}(r_0) = -\eta_{^{56}\text{Ni}}^{-1} Y'_{^{56}\text{Ni}}(r_0) \approx -\eta_s^{-1} Y'_{^{56}\text{Ni}}(r_0), \quad (19)$$

where the approximation holds because of the long lifetime of ^{56}Ni . Combining equations (15), (16), (17), (18), and (19) yields

$$\frac{dN_{^{57}\text{Ni}}/dt}{F_{^{56}\text{Ni}}} \approx \frac{r_0 \ln(r_{\text{hot}}/r_0) (Y_{^{57}\text{Cu}}/Y_{^{56}\text{Ni}})}{\rho_0 D_0 \eta_s} \approx 0.05. \quad (20)$$

Thus we obtain $\zeta_{\text{eff}} \approx 0.05$.]

The beta decay parents which hinder the rp-process are shown in column (1) of Table 1. Their daughters are shown in column (3), their halflives in column (4), and corresponding hindrance factors in column (5). The eventual decay products are shown in column (6). These are the products which are convected to the surface with a flux proportional to the value in column (7) (which will be further explained in §2.3).

2.3. Results

In §2.2 we assumed that the nuclear abundances on the surface of the star were constant, and we derived the fluxes of various products (column 6 of Table 1) out of the burning region. In a real star the surface abundances are of course not constant, but instead the original fuels become depleted and the burning products become enhanced, depending on the age of the star in its rp burning phase. In this section we assume that the surface abundances of the burning products are proportional to the outward fluxes (eq. [13] calculated in §2.2. (See §2.4 for further discussion of this assumption.) When a T^Z supergiant is about one third way through its rp burning stage, it has burned about one sixth of its CNO fuel and processed it to exotic products. (See §4 for a discussion of this statement.) Note that at the time when one sixth of the original CNO has been burned, one sixth of all the other original species (including Fe) has been burned as well. This is because the flux of the original seed into the burning region is always proportional to the abundance of that seed in the outer envelope. See, for example, equation (8), in which we could replace F_{12C} with F_{56Fe} and Y_{seed} with $Y_{Fe\ seed}$. At this time the nuclear species shown in column (6) of Table 1 have the abundances shown in column (7), denoted by $N_{1/3}$. That is to say, the abundances in column (7) are proportional to the fluxes in equation (13) with an overall factor corresponding to the assumption that one sixth of the original species have been burned.

(continued page 98)

TABLE 1
Surface Abundances for rp-isotopes

k	Parent	Daughter	half-life (s)	ζ	Final Product	$N_{1/3}$ ^a (10^6 Si)
(1)	(2)	(3)	(4)	(5)	(6)	(7)
1	²¹ Mg	²¹ Na	0.123	0.991	²¹ Ne	5.5×10^4
2	²² Mg	²² Na	3.86	0.920	²² Ne	5.3×10^5
3	²⁵ Si	²⁵ Al	0.22	0.988	²⁵ Mg	7.3×10^4
4	²⁶ Si	²⁶ Al	2.21	0.945	²⁶ Mg	3.5×10^5
5	²⁹ S	²⁹ P	0.19	0.989	²⁹ Si	6.5×10^4
6	³⁰ S	³⁰ P	1.2	0.963	³⁰ Si	2.2×10^5
7	³³ Ar	³³ Cl	0.18	0.989	³³ S	6.3×10^4
8	³⁴ Ar	³⁴ Cl	0.844	0.971	³⁴ S	1.7×10^5
9	³⁷ Ca	³⁷ K	0.173	0.989	³⁷ Cl	6.2×10^4
10	³⁸ Ca	³⁸ K	0.44	0.981	³⁸ Ar	1.1×10^5
11	³⁹ Ca	³⁹ K	0.86	0.971	³⁹ Ca	1.6×10^5
12	⁴² Ti	⁴² Sc	0.20	0.988	⁴² Ca	6.5×10^4
13	⁴⁵ Cr	⁴⁵ V	0.05	0.979	⁴⁵ Sc	1.1×10^5
14	⁴⁶ Cr	⁴⁶ V	0.26	0.986	⁴⁶ Ti	7.3×10^4
15	⁴⁹ Fe	⁴⁹ Mn	0.075	0.994	⁴⁹ Ti	3.1×10^4
16	⁵⁰ Fe	⁵⁰ Mn	0.16	0.991	⁵⁰ Cr	4.5×10^4
17	⁵¹ Fe	⁵¹ Mn	0.305	0.985	⁵¹ V	7.5×10^4
18	⁵⁴ Ni	⁵⁴ Co	0.08	0.994	⁵⁴ Fe	3.0×10^4
19	⁵⁵ Ni	⁵⁵ Co	0.212	0.988	⁵⁵ Mn	6.0×10^4
20	⁵⁶ Ni	⁵⁶ Co	5.3×10^5	0.0026	⁵⁶ Fe	4.6×10^6
21	⁵⁹ Zn	⁵⁹ Cu	0.184	0.989	⁵⁹ Co	2700
22	⁶⁰ Zn	⁶⁰ Cu	143	0.416	⁶⁰ Ni	2.3×10^5
23	⁶³ Ge	⁶³ Ga	0.32	0.984	⁶³ Cu	2700
24	⁶⁴ Ge	⁶⁴ Ga	63.7	0.579	⁶⁴ Zn	7.0×10^4
25	⁶⁷ Se	⁶⁷ As	0.16	0.991	⁶⁷ Zn	860
26	⁶⁸ Se	⁶⁸ As	96	0.494	⁶⁸ Zn	4.8×10^4

Surface Abundances for rp-isotopes (continued)

k	Parent	Daughter	half-life (s)	ζ	Final Product	$N_{1/3}^a$ (10^6 Si)
(1)	(2)	(3)	(4)	(5)	(6)	(7)
27	^{71}Kr	^{71}Br	0.097	0.993	^{71}Ga	330
28	^{72}Kr	^{72}Br	17.2	0.793	^{72}Ge	9700
29	^{75}Sr	^{75}Rb	0.16	0.991	^{75}As	340
30	^{76}Sr	^{76}Rb	8	0.869	^{76}Se	4900
31	$^{77}\text{Sr}^b$	^{76}Rb	13	0.862	^{77}Se	4400
31	$^{78}\text{Y}^b$	^{78}Sr	1	0.968	^{78}Kr	1000
31	$^{79}\text{Zr}^b$	^{79}Y	0.4	0.986	^{79}Br	450
32	^{80}Zr	^{80}Y	7	0.883	^{80}Kr	3700
33	^{81}Zr	^{81}Y	15	0.808	$^{81}\text{Br}^c$	5300
34	^{84}Mo	^{84}Nb	6	0.891	^{84}Sr	2400
35	^{85}Mo	^{85}Nb	3.2	0.926	^{85}Rb	1500
36	^{88}Ru	^{88}Tc	1.2	0.964	^{88}Sr	660
37	^{89}Ru	^{89}Tc	2.0	0.947	^{89}Y	940
38	$^{90}\text{Ru}^d$	^{90}Tc	23	0.802	^{90}Zr	3300
38	$^{92}\text{Pd}^d$	^{92}Rh	0.9	0.970	^{92}Mo	500
39	^{93}Pd	^{93}Rh	1.0	0.968	^{93}Nb	430
40	^{94}Pd	^{94}Rh	9.0	0.862	^{94}Mo	1800
41	$^{95}\text{Pd}^e$	^{95}Rh	13.3	0.823	^{95}Mo	2000
41	$^{97}\text{Cd}^e$	^{97}Ag	3	0.936	^{97}Tc	720
42	^{98}Cd	^{98}Ag	8	0.869	^{98}Ru	1200
43	^{99}Cd	^{99}Ag	16	0.802	^{99}Ru	1600
44	$^{100}\text{Cd}^d$	^{100}Ag	49.1	0.629	^{100}Ru	2400
44	$^{102}\text{Sn}^d$	^{102}In	2	0.947	^{102}Pd	340
45	^{103}Sn	^{103}In	7	0.883	^{103}Rh	470
46	^{104}Sn	^{104}In	20.8	0.768	^{104}Pd	830
47	^{105}Sn	^{105}In	31	0.708	^{105}Pd	800
48	^{106}Sn	^{106}In	126	0.441	^{106}Cd	1100

Surface Abundances for rp-isotopes (continued)

k	Parent	Daughter	half-life (s)	ζ	Final Product	$N_{1/3}$ ^a (10^6 Si)
(1)	(2)	(3)	(4)	(5)	(6)	(7)
49	^{107}Sn	^{107}In	174	0.377	^{107}Ag	530
50	^{108}Sn	^{108}In	618	0.174	^{108}Cd	270
51	^{111}Te	^{111}Sb	19.3	0.778	^{111}Cd	13
52	^{112}Te	^{112}Sb	120	0.455	^{112}Sn	24
53	^{113}Te	^{113}Sb	102	0.480	^{113}In	10
54	^{116}Xe	^{116}I	56	0.603	^{116}Sn	3.9
55	^{117}Xe	^{117}I	61	0.587	^{117}Sn	2.4
56	^{118}Xe	^{118}I	228	0.325	^{118}Sn	2.4

^a Formally these abundances are relative to 10^6 original Si atoms. Since Si is slightly depleted from the envelope, whereas H is hardly depleted, it may be more helpful to think of these numbers as relative to 2.8×10^{10} H atoms.

^b The interaction among the species ^{77}Sr , ^{78}Y , and ^{79}Zr is uncertain. See the discussion in §2.1 (eq. [1]).

^c The half-life for ^{81}Kr to decay to ^{81}Br is 2.1×10^5 yr.

^d The equilibrium involving ^{90}Ru and ^{92}Pd is uncertain. See the discussion in the last paragraph of §2.1 (eq. [2]).

^e The equilibrium involving ^{95}Pd and ^{97}Cd is uncertain. See the discussion in the last paragraph of §2.1 (eq. [3]).

^f The equilibrium involving ^{100}Cd and ^{102}Sn is uncertain. See the discussion in the last paragraph of §2.1 (eq. [4]).

In Table 2 we sum the contributions of various isotopes in Table 1 to yield elemental surface abundances. The third column, $\log N_{1/3} - \log N_{\odot}$, gives the comparison to solar system abundances (i.e., Population I abundances). In Table 2 we include only the elements which are produced in large quantities, so that we do not list any elements with $Z < 26$. Notice that Fe has an abundance greater

than solar by a factor of 5, and for Mo, Ru, Rh, Pd, and Ag the factors are over 1000.

Some of these abundances depend rather sensitively on the details of the reaction network and thus on the details of the (semi-empirically determined) nuclear masses and reaction rates. For instance, the presence of Tc depends on the position of the equilibrium given in equation (3), and the presence of Ar depends on the position of the equilibrium in equation (2). These uncertainties are indicated by a range of values in parentheses. In addition, the abundances of elements with $Z > 42$ (i.e., heavier than Mo) may be lower than indicated in Table 2. Cannon (1992) has presented models of TZO with lower temperatures ($T \sim 1.6 \times 10^9$ K) at the base (“knee”) of the envelope (*cf.* $T \sim 2.1 \times 10^9$ K in Paper I), so that the burning region would produce less of the heavier elements than shown in Table 2. Nevertheless, the abundances of elements with $26 \leq Z \leq 42$ should depend only weakly on the temperature at the base (as long as it is greater than 1.6×10^9 K), so these abundance estimates in Table 2 should be reliable.

2.4. Timescale for establishing steady-state

In §2.2 we used a steady-state model in order to calculate the outward flux of burning products. In §2.3 we relaxed the assumptions of §2.2 and assigned surface abundances proportional to the fluxes by the methods in §2.2. This reasoning is appropriate if the following conditions hold: 1) The timescale for setting up a steady state T_{ss} is long compared to the halflives of the species shown in column (2) of Table 1. 2) This steady-state timescale is short compared to the lifetime of the TZO supergiant. 3) And the “hindrance factors” ζ_k are of order 1.

Let us look at the first two conditions. The timescale for setting up a steady state is approximately the same as the timescale for convecting a species from the burning region to the surface, T_{diff} . One way to calculate this quantity is to assume there is an imaginary species with mean lifetime τ_{imag} , which is produced at the burning region. We assume a steady-state model, so that the abundances

TABLE 2
SURFACE ABUNDANCES OF HEAVY ELEMENTS

Z	species	$N_{1/3}$ ^{a,b} (10^6 Si)	N_{\odot} ^c (10^6 Si)	$\log_{10} \left(\frac{N_{1/3}}{N_{\odot}} \right)$ ^b
26	Fe	4.6×10^6	9.0×10^5	0.71
28	Ni	2.3×10^5	4.9×10^4	0.67
29	Cu	2700	522	0.71
30	Zn	1.2×10^5	1260	1.98
31	Ga	330	37.8	0.94
32	Ge	9700	119	1.91
33	As	340	6.56	1.71
34	Se	4900(9300) ^d	62.2	1.90(2.17) ^d
35	Br	5300(5800) ^e	11.8	2.65(2.69) ^e
36	Kr	4700(3700) ^f	45	2.02(1.91) ^f
37	Rb	1500	7.09	2.28
38	Sr	3100	23.5	2.12
39	Y	940	4.64	2.31
40	Zr	3300(0) ^g	11.4	2.46(≥ 0) ^g
41	Nb	430	0.698	2.79
42	Mo	3800(1800-4300) ^h	2.55	3.17(2.85-3.23) ^h
43	Tc	0(720) ⁱ
44	Ru	5200(2800) ^j	1.86	3.45(3.18) ^j
45	Rh	470(710) ^j	0.344	3.14(3.31) ^j
46	Pd	1600(2800) ^j	1.39	3.07(3.30) ^j
47	Ag	530(800) ^j	0.486	3.04(3.22) ^j
48	Cd	280(2100) ^j	1.61	2.57(2.74) ^j
49	In	10(16) ^j	0.184	1.74(1.94) ^j
50	Sn	33(49) ^j	3.82	0.93(1.11) ^j

^a See explanation in Table 1.

^b These estimates may be high for elements heavier than Mo. See the last paragraph in §2.3.

^c These are from Anders & Grevesse (1989).

^d This is the result if ⁷⁷Sr dominates the equilibrium in equation (1).

^e This is the result if ⁷⁹Zr dominates the equilibrium in equation (1).

^f This is the result if ⁷⁸Y does not dominate the equilibrium in equation (1).

^g This is the result if ⁹²Pd dominates the equilibrium in equation (2).

^h The abundance of Mo lies in this range depending on the equilibria (2) and (3).

ⁱ The presence of ⁹⁷Tc depends on equilibrium (3).

^j This is the result if ¹⁰²Sn dominates the equilibrium in equation (4).

of the parent and daughter at the photosphere are zero,

$$Y_P(r_{\text{ph}}) = Y_D(r_{\text{ph}}) = 0, \quad (21a)$$

but the fluxes at r_{ph} are nonzero. At the burning region we have a finite $Y_P(r_0)$, so that we have

$$Y'_P(r_0) = \text{constant} \quad Y'_D(r_0) = 0. \quad (21b)$$

We ask, what is the value of τ_{imag} such that

$$Y'_P(r_{\text{ph}}) = Y'_D(r_{\text{ph}}), \quad (21c)$$

that is, such that half the unstable parent species remains when it arrives at the photosphere. A simple application of the formalism of §4.2 of Paper I yields the result $\tau_{\text{imag}} = 1900$ yr, so that we estimate $T_{\text{diff}} \sim 1000$ yr.

Another way to calculate T_{diff} is to consider the random walk which brings nuclei from the burning zone to the surface. The outermost 10 pressure scale heights have turnover timescales on the order of 1 yr, so we may estimate $T_{\text{diff}} \sim 10^2(1 \text{ yr}) = 100$ yr. We obtain the same answer if we consider all the pressure scale heights and turnover times given in Table 6 of Paper I. That is, if we perform a time-dependent simulation in which an imaginary species is injected into the burning region and determine how long it takes before a substantial amount builds up on the surface, then again we obtain about 100 yr. The similarity of these results is convincing that the time for setting up a steady state is about 100-1000 yr.

We note that $T_{\text{diff}} \sim 1000$ yr is much longer than the positron-decay half-life of the longest-lived parent in column (2) of Table 1, that is, the 6.1 d half-life of ^{56}Ni . We also compare T_{diff} to the lifetime of the TŻ supergiant, which is calculated in §4 to be 6×10^5 yr.

Now for the decay of ^{56}Ni and for several other entries in Table 1 with $A \geq 60$ we no longer satisfy the condition 3) above, that is, we have $\zeta_k \ll 1$. The result of this is that Tables 1 and 2 may underestimate the production of very heavy metals ($Z \geq 48$), especially at late times in the star's lifetime (*cf.* Cannon 1992).

For the elements in which we are interested ($26 \leq Z \leq 42$) this effect is much smaller than the uncertainties due to the nuclear physics (*cf.* Table 2 and §2.1).

3. Absorption spectroscopy

In §2 we demonstrated that T \dot{Z} supergiants produce a flux toward the surface of metals heavier than Fe, especially Br, Rb, Y, Nb, and Mo (Table 2). Identification of T \dot{Z} supergiants involves detecting these abundances (relative to solar) through absorption spectroscopy. This project is complicated by the presence of a preponderance of neutral metal lines and TiO molecular bands in the spectra of these cool stars. It is impossible to find absorption lines for the elements in Table 2 which are not blended to some degree with other lines, but it is possible to find absorption lines from which approximate abundances can be determined.

The lines in Table 3 are chosen so that they do not occur near to (and to the red of) the band heads of TiO and do not appear strongly blended with other metal lines. The three optical Sr lines and the lines of Rb (7800 Å), Y, Zr, and Mo are distinguishable in the solar spectrum (Delbouille, Roland, and Neven 1973) and in the spectrum of Arcturus (Griffin 1968). They are also distinguishable in a spectrum of BS 6039, a M4 III star, taken at resolution 15000 by M. Rich (1990, private communication) with a coudé spectrograph (built by J. McCarthy) at Palomar Mountain. The Ru line is not visible in the solar spectrum, but it seems to be weakly visible in Arcturus and in BS 6039. Again, if the Ru abundance is enhanced, then this line should be strongly visible.

R. Kurucz (private communication) has produced synthetic spectra which indicate that a resolution of $\gtrsim 15000$ is sufficient to distinguish a factor of 10 in abundances of those elements showing lines in the optical spectrum (all those shown in Table 3 except for Sr). This is illustrated in Figure 2, which displays superimposed synthetic spectra (resolution 15000) with the abundance of Mo equal to solar and equal to 10 times solar.

For the three Sr lines in the infrared we need enough resolution to distinguish the metal lines from the “noise” of TiO bands all of which shade to the red. The

TABLE 3
Lines of Heavy Elements

Z	Line	λ (Å)	χ (ev)	remarks
37	Rb I	7947.63	0.00	1
	Rb I	7800.23	0.00	
38	Sr I	4607.34	0.00	2
	Sr II	4077.72	0.00	
	Sr II	4215.54	0.00	2
	Sr II	10036.66	1.80	
	Sr II	10327.31	1.83	
	Sr II	10914.88	1.80	
39	Y II	4883.69	1.08	
40	Zr I	6172.48	0.15	
	Zr I	6143.18	0.07	
42	Mo I	5570.40	1.33	
44	Ru I	5309.27	0.92	3

REMARKS:

1. This may be obscured by atmospheric H₂O.
2. Line is distinct from, but blended with, nearby Fe I line.
3. Line is not visible in the solar spectrum but is perhaps visible in the spectra of Arcturus and BS 6039. It should be clearly visible in a T \dot{Z} supergiant.

synthetic spectra of R. Kurucz indicate that a resolution of $\gtrsim 20000$ is needed to determine Sr abundance to about a factor of 10.

Although it may be possible to identify a candidate list of T \dot{Z} supergiants by simple inspection of the line strengths in the spectra of red supergiants, a full analysis would involve comparing observed spectra with realistic synthetic spectra. Otherwise it could involve comparing the spectrum of a candidate T \dot{Z} supergiant with a star with similar surface conditions (temperature and surface gravity) (*cf.* Tomkin and Lambert 1983).

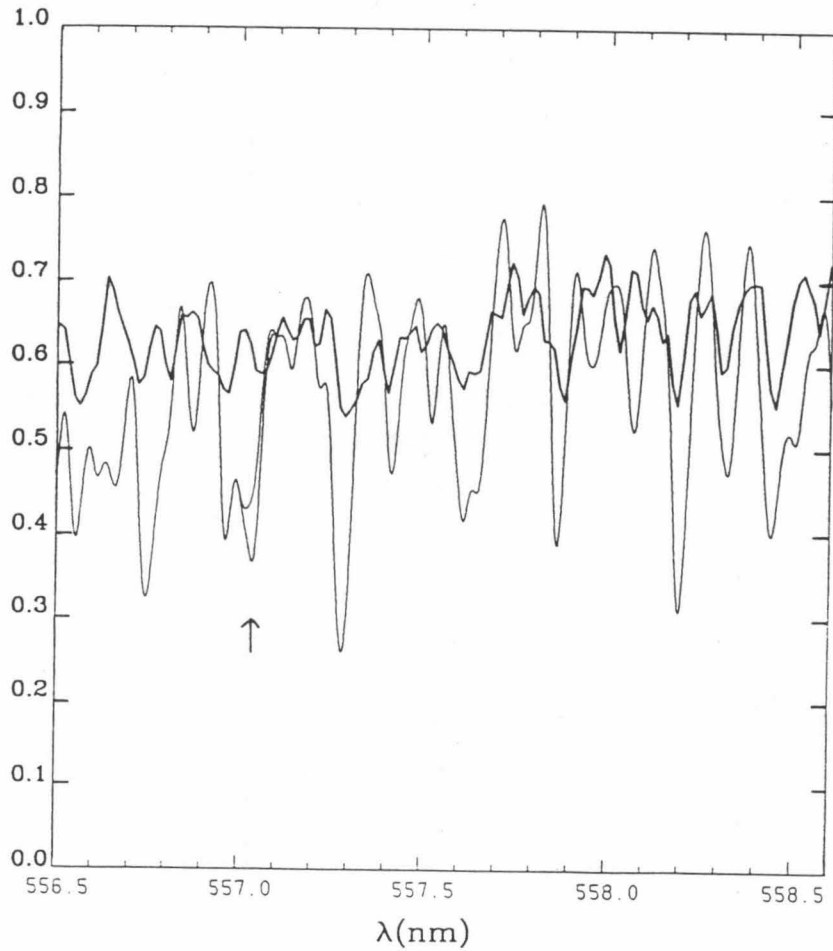


Fig. 2—Portion of a synthesized spectrum (light lines) for a red supergiant with Population I abundances and with Mo abundance times 10, respectively. The arrow points to a Mo line. Shown for rough comparison is a portion of the spectrum of BS 6039 (J. McCarthy, private communication), a red giant.

4. Number of T \dot{Z} supergiants in the solar neighborhood

T \dot{Z} supergiants are spectral type M I stars, that is, red supergiants. Jura and Kleinmann (1990) report about 21 stars within 2.5 kpc which are red supergiants, that is, with luminosity $\gtrsim 10^5 L_{\odot}$. There are on the order of 100 red supergiants within 5 kpc of the sun (M. Jura 1993, private communication). In this section we will obtain an estimate for the fraction of these stars which are T \dot{Z} supergiants based on a counting of likely progenitors. We assume the progenitor of a T \dot{Z} supergiant is a binary system of a massive star and a neutron star which are close enough to each other that, once the neutron star is engulfed, it spirals in to the center without envelope ejection.

Taam, Bodenheimer, and Ostriker (1978) calculate critical binary periods such that a binary system with a shorter period undergoes coalescence without envelope disruption. In these binaries the neutron star is engulfed during core hydrogen burning, during shell hydrogen burning, or shortly after the onset of core helium burning. Most of the energy of the spiral in is deposited at the base of the envelope; however, the convective energy transport in this relatively tightly bound envelope is efficient enough to transport this energy to the surface where it is radiated away. A binary system which has a period greater than the critical period has a less tightly bound envelope after the onset of spiral in. More importantly, the density of the envelope at its base is less than that in the former case and convection is inefficient. The envelope is therefore ejected. These critical periods are reproduced in Table 4.

These binaries of a massive star and a neutron star appear in the sky as high-mass X-ray binaries (HMXBs) of which there are two categories: those with a Be star companion (called Be systems) and those with a supergiant (OB star) companion (called MB, or massive binary, systems). Whereas the Be systems derive X-rays from a stellar wind falling on the neutron star, the MB systems may be wind fed or fed by Roche lobe overflow (also called disk fed). The lifetimes for all three kinds of systems are rather uncertain, and for this reason we work out an estimate of the number of T \dot{Z} supergiants in several ways.

TABLE 4
Critical Orbital Periods
for Spiral in

Companion Mass (M_{\odot})	Approximate Spectral Type ^a	$P_{b,crit}$ ^b (d)
8	B5	48
16	B0	117
24.24	O7	171

^a This is the spectral type of the companion before spiral in. ^b Systems with smaller period than the critical period will coalesce without envelope disruption, assuming a $1 M_{\odot}$ neutron star (Taam *et al.* 1978).

The lifetime of a TŻ supergiant is calculable by considering the time it takes for the star to exhaust its fuel, that is, the C, N, and O which act as seeds for the rp-process. It turns out that the star will cease its rp-burning stage when about half its fuel is burned. This is true for the following reason: A TŻ supergiant begins its existence with $Z_{fuel} = 0.02$ (although this may be larger if the supernova which produced the neutron star enhanced the metallicity of the companion). By the time Z_{fuel} becomes 0.01, the temperature at the base of the envelope is about 3×10^9 K (see the fourth entries of Tables 1 and 4 of Paper I) and the rp-process becomes inefficient (see §1 of the Appendix of Paper I). Thus we estimate the lifetime of the TŻ supergiant to be the time needed to burn half its fuel. The number of seed atoms is given by $M_{env} Z L_{Av} / 12$, where M_{env} is the mass of the envelope, Z is the metallicity, L_{Av} is Avogadro's number, and 12 is the atomic weight of carbon. The heat energy liberated from burning ^{12}C to ^{56}Ni is $\Delta E_{heat} = 263$ MeV (the energy of reaction less half the beta decay energy to neutrinos). The lifetime is given by

$$T_{T\check{Z}} \sim \frac{1}{2} \frac{M_{env} Z L_{Av} \Delta E_{heat}}{12L} = 6 \times 10^5 \text{ yr.} \quad (22)$$

If we assume that the rate of star formation in the solar neighborhood has

been approximately constant (Schmidt 1959), then we may write

$$N_{\text{T}\dot{Z}} \approx N_{\text{prog}} \frac{T_{\text{T}\dot{Z}}}{T_{\text{prog}}}, \quad (23)$$

where $N_{\text{T}\dot{Z}}$ and N_{prog} are the numbers of $\text{T}\dot{Z}$ supergiants and progenitors, respectively, within 5 kpc, and $T_{\text{T}\dot{Z}}$ and T_{prog} are respective lifetimes. Table 5 shows the observed nontransient HMXBs which have sufficiently short orbital period to preclude envelope disruption during spiral in (Nagese 1989). (Questions of completeness are controversial, so we may be underestimating their number.)

Consider first the suitable Be systems known to be within 5 kpc, of which there are 5. We estimate the lifetime of these systems to be less than but on the order of the main sequence lifetime of the Be star, that is, 3×10^6 yr. Thus we obtain

$$N_{\text{T}\dot{Z}} \approx N_{\text{Be}} \frac{T_{\text{T}\dot{Z}}}{T_{\text{Be}}} = 5 \frac{6 \times 10^5 \text{ yr}}{3 \times 10^6 \text{ yr}} = 1 \quad (24)$$

$\text{T}\dot{Z}$ supergiant within 5 kpc. Note, however, that Rathnasree and Ray (1992) estimate a lifetime of 3×10^5 yr for these Be systems, assuming that the star creating the wind is somewhat evolved, leading to $N_{\text{T}\dot{Z}} \approx 10$.

Consider all the suitable MB systems which have been found, of which there are 7. The orbits of two MB systems are decaying at a known rate, that is, $\dot{P}_b/P_b = -1.8 \times 10^{-6} \text{ yr}^{-1}$ for Cen X-3 (Kelley *et al.* 1983) and $\dot{P}_b/P_b = -3.36 \times 10^{-6} \text{ yr}^{-1}$ for SMC X-1 (Levine *et al.* 1992). Levine *et al.* (1992) make the case that the orbital decay is due to tidal interaction. If this is true (their conclusion is controversial), then we can apply the derived lifetime of 4×10^5 yr to all the MB systems. In this case we have

$$N_{\text{T}\dot{Z}} \approx N_{\text{MB}} \frac{T_{\text{T}\dot{Z}}}{T_{\text{MB}}} \gtrsim 8 \left(\frac{5 \text{ kpc}}{13 \text{ kpc}} \right)^2 \frac{6 \times 10^5 \text{ yr}}{4 \times 10^5 \text{ yr}} \quad (25)$$

$$N_{\text{T}\dot{Z}} \gtrsim 2$$

$\text{T}\dot{Z}$ supergiants within 5 kpc. We have used 13 kpc for the radius of the Galaxy, and we use an inequality because our list of MB systems is probably not complete.

Consider the MB binary systems in which the X-ray source is fed by Roche lobe overflow. Although there is only one (Cen X-3) that is definitely so identified

TABLE 5
Possible TŻ Supergiant Progenitors

Source	Companion	T_{pulse} (s)	P_b (d)	D (kpc)	remarks ^a
4U 0115+634	O-Be	3.61	24.31	3.5	Be
V 0331+530	Be	4.37	34.25	2-4	Be
(Cen X-3) 1119-603	O6-8f	4.84	2.087	8	MB(RLO)
1E 1048-593	Be	6.44	$\sim 30^b$	3	Be
2S 1553-542	Be	9.29	31	...	Be
2S 1417-624	Be?	17.6	~ 15	...	Be?
OA0 1657-41	OB	38.2	10.4 ^c	1-5	MB
EXO 2030+375	Be	41.8	~ 46	~ 5	Be
A 0535+262	B0 III-Ve	104	111	2.4	Be
(Vela X-1) 4U 0900-403	B0.5 Ib	283	8.965	2.0	MB
E 1145.1-614	B2 I-IIa	297	5.648	8	MB
4U 1907+097	OB I	438	8.38	7	MB
4U 1538-522	B0 I	529	3.730	7	MB
GX 301-2	B1.5 Ia	696	41.50	1.8	MB

^a Here Be refers to a Be star companion. MB refers to a massive binary, i.e., with OB star companion. RLO refers to Roche lobe overflow.

^b This is an estimate based on the correlation of pulsar spin period and orbital period in wind-fed systems. See Waters and van Kerkwijk (1989) and references therein.

^c This comes from Finger *et al.* (1992).

in this Galaxy, there is also one in the LMC (X-4) and one in the SMC (X-1). The lifetime for such a system is estimated to be $\sim 10^4$ yr (Levine *et al.* 1992, Verbunt and Rappaport 1988; see however also Savonije 1979, 1980). If we assume there

is one RLO system in the Galaxy, on average, then

$$N_{\text{T}\dot{Z}} \approx N_{\text{RLO}} \frac{T_{\text{T}\dot{Z}}}{T_{\text{RLO}}} \sim 1 \left(\frac{5 \text{ kpc}}{13 \text{ kpc}} \right)^2 \frac{6 \times 10^5 \text{ yr}}{1 \times 10^4 \text{ yr}} = 9 \quad (26)$$

T \dot{Z} supergiants within 5 kpc.

On the other hand, Meurs and van den Heuvel (1989) estimate the Galactic number of quiescent close binary systems containing a neutron star and a massive companion ($M > 16 M_{\odot}$) to be ~ 3000 (see also Rappaport and van den Heuvel 1982). If this is so, and we estimate the lifetime of the main sequence companion as 10^7 yr, then we obtain

$$N_{\text{T}\dot{Z}} \approx N_{\text{prog}} \frac{T_{\text{T}\dot{Z}}}{T_{\text{prog}}} \lesssim 3000 \left(\frac{5 \text{ kpc}}{13 \text{ kpc}} \right)^2 \frac{6 \times 10^5 \text{ yr}}{1 \times 10^7 \text{ yr}} = 27 \quad (27)$$

T \dot{Z} supergiants within 5 kpc. This is an overestimate because we have not excluded all the systems with periods which are too long to allow coalescence without envelope disruption. Correction for this might revise the estimate downwards by a factor of several or perhaps 10 (see Meuers and van den Heuvel 1989).

Thus we estimate that out of the 400 nearest red supergiants, i.e., those within 5 kpc, several are probably T \dot{Z} supergiants.

5. Conclusion

A star with a degenerate neutron core and mass greater than about $14 M_{\odot}$, that is, a T \dot{Z} supergiant, would appear spectroscopically like a red supergiant, that is, spectral type M I. In this paper we have shown that a T \dot{Z} supergiant can be distinguished from a “normal” supergiant by the large surface abundances of Mo (1000 times solar) and of Br, Rb, Y, and Nb (greater than 200 times solar), as shown in Table 2. In particular the large abundances of Rb, Y, and Mo can be detected using the absorption lines shown in Table 3. The abundances in Table 2 should be sufficient to distinguish a T \dot{Z} supergiant not only from an ordinary red supergiant but also from two other possibilities: 1) an AGB star (misclassified as supergiant) dredging up s-process elements and 2) a supergiant with s-process element dumped on by a companion (*cf.* a Ba star, Tomkin & Lambert 1983).

Although TŻ supergiants are likely to be rare, nevertheless there should be several, perhaps as many as 10 (see eq. [26]), within 5 kpc of the sun. In this case there would be several TŻ supergiants near enough that one could take a spectrum and determine surface abundances. We conclude that the prospects for identifying a TŻ supergiant with present technology are good.

Future avenues of possible research include topics mentioned in Paper I. Cannon (1992) has addressed some of these issues by producing a time-dependent model with a full rp reaction network. In addition he has explored the effect of varying some of the assumptions involved in convective mixing, and he obtains $14 M_{\odot}$ for lower limit of the mass of a TŻ supergiant, so that there is still a mass gap in which there are no steady-state models. It has been suggested (E. Salpeter 1990, private communication) that there might be solutions for the structure of a TŻO in the mass gap involving relaxation oscillations at the base of the envelope, tapping into the store of gravitational energy, but the nature of such a solution remains to be worked out.

The author thanks David Goldberg and Petr Vogel for helpful discussions in nuclear physics, Jeremy Mould for discussions of spectroscopy, and Saul Rappaport, Lars Bildsten, and Ed van den Heuvel for discussions of HMXBs. The author thanks Mike Rich for his spectrum of BS 6039, Jim McCarthy for helpful explanations of the calibration software, and Robert Cannon for a critical reading of this manuscript. The author especially thanks Robert Kurucz for his patient work in generating synthetic spectra of these stars. Support through NSF Grant AST-9114925 is gratefully acknowledged.

REFERENCES

- Anders, E., & Grevesse, N. 1989, *Geochimica et Cosmochimica Acta*, 53, 197.
- Barden, R., Kirchner, R., Klepper, O., Plochocki, A., Rathke, G.-E., Roeckl, E., Rykaczewski, K., Schardt, D., & Żylicz, J. 1988, *Z. Phys. A*, 329, 319.
- Biehle, G. T. 1991, *ApJ*, 380, 167 (Paper I).
- Biehle, G. T., & Vogel, P. 1992, *Phys. Rev. C*, 46, 1555.
- Bisnovatyi-Kogan, G. S., & Lamzin, S. A. 1984, *Astron. Zh.* 61, 323 [English transl. in *Soviet Astr.-AJ*, 28, 187].
- Caughlin, G. R., & Fowler, W. A. 1988, *Atomic Data Nucl. Data Tables*, 40, 283.
- Cannon, R. C., Eggleton, P. P., Żytkow, A. N., & Podsiadlowski, P. 1992, *ApJ*, 386, 206.
- Cannon, R. C. 1992, *MNRAS*, in press.
- Delbouille, L., Roland, G., & Neven, L. 1973 *Photometric Atlas of the Solar Spectrum from λ 3000 to λ 10000* (Cointe-Ougrée, Belgium: Institut d'Astrophysique de l'Université de Liège).
- Despain, K. H. 1976, Ph.D. thesis, California Institute of Technology, Pasadena.
- Eggleton, P. P., & Verbunt, F. 1986, *MNRAS*, 220, P13.
- Eich, C., Zimmermann, M. E., Thorne, K. S., & Żytkow, A. N. 1989, *ApJ*, 346, 277.
- Finger, M. H., Chakrabarty, D., Grunsfeld, J. M., Prince, T. A., Wilson, R. B., Fishman, G. J., Meegan, C. A., Paciesas, W. S. 1992, *International Astronomical Union Circular* 5430.
- Gagliardi, C. A., Semon, D. R., Tribble, R.E., & Van Ausdeln, L. A. 1986, *Phys. Rev. C*, 34, 1663.
- Gamow, G. 1937, *Structure of Atomic Nuclei and Nuclear Transformations* (Oxford: Oxford Univ. Press), 237.

- Griffin, R. F. 1986 *A Photometric Atlas of the Spectrum of Arcturus $\lambda\lambda$ 3600-8825 Å* (Cambridge, England: University Printing House).
- Jänecke, J., & Masson, P. J. 1988, *Atomic Data Nucl. Data Tables*, 39, 265; see also pp. 289ff.
- Jura, M., & Kleinmann, S. G. 1990, *ApJS*, 73, 769.
- Kelley, R. L., Rappaport, S., Clark, G. W., & Petro, L. D. 1983, *ApJ*, 268, 790.
- Landau, L. D. 1937, *Dokl. Akad. Nauk SSSR*, 17, 301 [English transl. in *Nature*, 141, 333 (1938)].
- Leonard, P. J. T., Hills, J. G., & Dewey, R. J. 1993, preprint.
- Levine, A., Rappaport, S., Boynton, P., Deeter, J., & Nagase, F. 1992, preprint, submitted to *ApJ*.
- Meurs, E. J. A., & van den Heuvel, E. P. J. 1989, *A&A*, 226, 88.
- Nagase, F. 1989 *Publ. Astron. Soc. Japan*, 41, 1.
- Rappaport, S. A., & van den Heuvel, E. P. J. 1982, in *Be Stars*, eds. M. Jaschek and H. G. Groth (Dordrecht, Holland: Reidel), p. 327.
- Rathnasree, N., & Ray, A. 1992 *Journal of Astrophysics and Astronomy*, 13, 3.
- Ray, A., Kembhavi, A. K., & Antia, H. M. 1987, *A&A*, 184, 164.
- Savonije, G. J. 1979, *A&A*, 71, 352.
- Schmidt, M. 1959, *ApJ*, 129, 243.
- Seth, Kamal K., Iversen, S., Kaletka, M., Barlow, D., Saha, A., & Soundranayagam, R. 1986, *Phys. Lett. B*, 173, 397.
- Taam, R. E., Bodenheimer, P., & Ostriker, J. P. 1978, *ApJ*, 222, 269.
- Takahashi, K., Yamada, M., & Kondoh, T. 1973, *Atomic Data Nucl. Data Tables*, 12, 101.
- Thorne, K. S., & Żytkow, A. N. 1977, *ApJ*, 212, 832 (TŻ).

Tomkin, J., & Lambert, D. L. 1983, *ApJ*, 273, 722.

Verbunt, F., & Rappaport, S. 1988, *ApJ*, 332, 193.

Wallace, R. K., & Woosley, S. E., 1981, *ApJS*, 45, 389.

Waters, L. B. F. M., & van Kerkwijk, M. H. 1989, *A&A*, 223, 196.

Woosley, S. E., Fowler, W. A., Holmes, J. A., & Zimmermann, B. A. 1978, *Atomic Data Nucl. Data Tables*, 22, 371.

Woosley, S. E., Holmes, J. A., Fowler, W. A., & Zimmermann, B. A. 1975, *Orange Aid Preprint 422* (Pasadena: Kellogg Radiation Laboratory, Caltech).

Chapter 5

Hard Apex Transition in Quasi-Periodic Oscillators—
Closing of the Accretion Gap

Garrett T. Biehle and Roger D. Blandford

Finale

This chapter will appear in the *Astrophysical Journal*.

1. Introduction

It is generally accepted that the phenomenon of Quasi-Periodic Oscillations (QPO), first reported by van der Klis *et al.* (1985), contains important clues about the mode of accretion in Low Mass X-ray Binary sources (LMXBs). QPO are the ~ 10 Hz broad peaks observed in the power spectra of these X-ray sources. In the six years since this discovery, a detailed phenomenological understanding of QPO and of the sources' spectra has emerged (van der Klis 1989). In the six so-called Z-sources, the X-ray fluxes from individual sources can be plotted on a two-color diagram and are found to trace a one-parameter, Z-shaped curve, varying on a timescale $\sim 1 - 10$ hr (Hasinger 1987). (See Figure 1.) We will be concerned exclusively with these sources in this paper. Schulz & Wijers (1991) introduced the parameter α , called the spectral rank, which measures distance along the curve. The parameter α increases in the direction that one would normally draw a Z, such that we have $0 < \alpha < \frac{1}{3}$ along the upper stroke, called the Horizontal Branch (HB), we have $\frac{1}{3} < \alpha < \frac{2}{3}$ along the diagonal, called the Normal Branch (NB), and we have $\frac{2}{3} < \alpha < 1$ along the lower stroke, called the Flaring Branch (FB). It is generally believed that mass accretion rate increases monotonically with α (Hasinger 1988), and good evidence for this has been given by Vrtilik *et al.* (1991) for Sco X-1. (However, see Tan *et al.* 1992.)

The low Q pulsations, by which QPO sources are distinguished, are strongly correlated with α . As α increases on the HB, the primary frequency increases over a range $\sim 20 - 50$ Hz. In several sources, a characteristic frequency $\sim 6 \pm 1$ Hz, is measured on the NB. The primary frequency then increases again to $\sim 10 - 20$ Hz along the FB, increasing also in width and prominence. The transition from the HB to the NB is also marked by a cutoff of low frequency noise (LFN) associated with the HB. In Cyg X-2 the strength of the LFN increases with α on the HB and rapidly decreases with α on the NB (Hasinger 1991, see also Hasinger *et al.* 1990). This cutoff and on of LFN has been observed to occur in less than about 200 s and has been likened to a phase transition (Hasinger 1988). It is the purpose of this paper to interpret the "hard apex", the transition from the HB to the NB, in

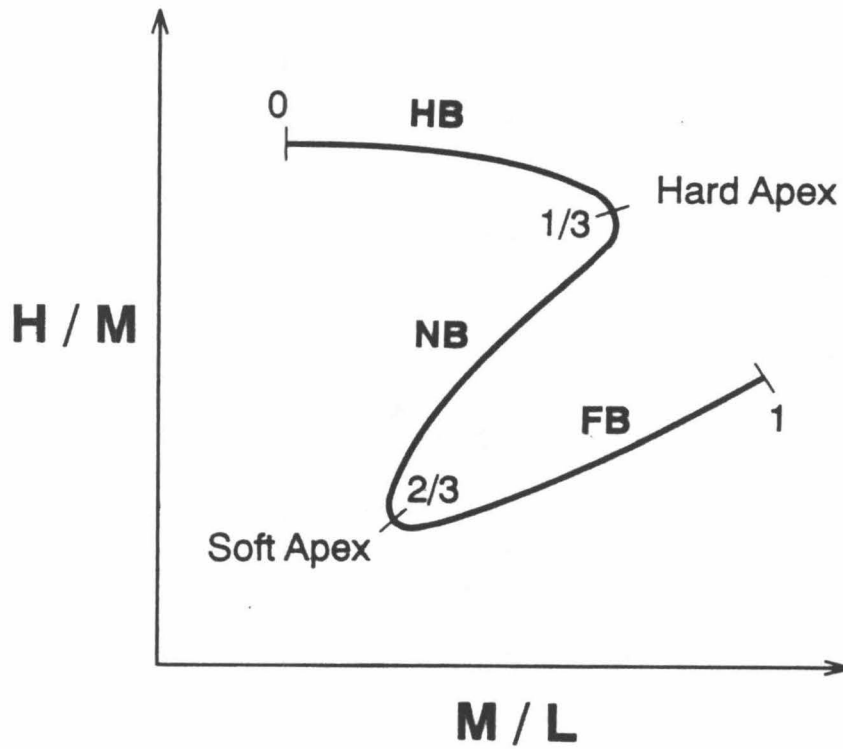


Fig. 1—QPO Z-diagram, with H representing the high energy band 6-20 keV; M , the medium band 3-6 keV; and L , the low band 1-3 keV. An individual object traverses this locus on timescales of about hours. The parameter α , introduced by Schulz and Wijers (1991), is believed to increase monotonically with mass accretion rate. The point $\alpha = \frac{1}{3}$ represents the Hard Apex, while $\alpha = \frac{2}{3}$ represents the Soft Apex.

terms of a particular model of neutron star accretion.

Almost immediately after the first reports of this phenomenology, an ingenious model was devised to account for QPO (Alpar & Shaham 1985). In this model, the observed HB oscillation is associated with a beat between the spin frequency of a pulsar magnetosphere and the orbital angular frequency of a Keplerian disk. The correlation of primary frequency with accretion rate then reflects a motion of the Alfvén surface. A concern with the “beat frequency model” is that the fundamental rotation frequency of the star has never been observed. This is usually explained by appealing to electron scattering in an optically thick cloud of plasma surrounding the source, and, indeed there is evidence for Comptonization in the delay of the arrival of hard photons, known as the “hard lag”, and in the width of the 6.7 keV Fe line. (White *et al.* 1986) The ~ 6 Hz oscillation on the NB is associated with a non-linear oscillation of a radial accretion flow driven by radiation pressure (Fortner *et al.* 1989, Miller & Lamb 1992).

In this paper, we explore some aspects of an alternative model of accretion in Z-sources, wherein an accretion disk extends close to the surface of an unmagnetized neutron star, and the three branches are associated with changes in the disk-star interface. The neutron star must be compact enough to lie within the marginally stable circular orbit of an accretion disk, so that an “accretion gap” exists (Kluźniak & Wagoner 1985, Sunyaev & Shakura 1986) during the low accretion rate of the HB. The gas then drips from the inner edge of the disk and hits the star with mildly relativistic speed at grazing incidence. More than half the total power is released in the surface layer of the star in a relatively hard spectrum (Kluźniak & Wilson 1991). As the accretion rate increases, the disk inner edge shrinks until it touches the star surface. The closing of the accretion gap and forming of a boundary layer marks the transition from the HB to the NB. As the accretion rate further increases, the boundary layer thickens until it covers the whole surface of the neutron star. This marks the transition to the FB, where the accretion rate is super-Eddington and radiation escapes primarily through large-scale convective instabilities. Although we shall defer discussion of these matters to

a subsequent paper, we tentatively associate the HB oscillation with disk modes (*cf.* Nowak & Wagoner 1991, 1992) and the NB and FB oscillation with non-radial normal modes in the star.

In §2 we outline simple thick accretion disk models and show how the inner radius, that is, the inner-cusp radius, varies with accretion rate \dot{M} . These models represent accretion on the horizontal branch. We use the cusp radius as an estimate of the location of the disk inner edge in a real accreting system. (This estimate is discussed in §4.) We conclude that it is possible that a neutron star lie within the inner edge of an accretion disk with nearly critical (Eddington) accretion rate and that this accretion gap close with increasing \dot{M} .

In §3, we speculate upon the changing character of the boundary layer as an object moves along the Z in a two-color diagram, and we relate the changing boundary layer to the changing spectral phenomenology. In §4, we consider the constraints on the neutron star mass-radius relation and, by extension, on the equation of state of nuclear matter, if the hard apex transition is, as we hypothesize, identifiable with closing the accretion gap. We discuss some observational ramifications in the concluding section.

2. Slender accretion disks

Some neutron star equations of state allow the star radius to lie within the marginally stable orbit, that is, the inner radius of a thin accretion disk, at $r = 6m$ (see, e.g., Kluźniak & Wagoner 1985). In this section we consider slender accretion disks of the type believed to form around LMXB's which produce QPO.

For illustration purposes, we consider an axisymmetric disk composed of a perfect fluid with negligible self-gravity. We assume that the fluid is in hydrostatic equilibrium and is radiation-pressure dominated. [If we naively apply α -disk theory (Novikov & Thorne 1973) to a $1.45 M_{\odot}$ star accreting at $0.1 L_{\text{Edd}}$, then $p_{\text{gas}}/p_{\text{rad}} \sim 0.02$ at $r = 12m$, the radius within which most of the luminosity is produced.] If dynamical instabilities interchange rings of constant specific angular momentum l ($\equiv -u_{\phi}/u_0$) in the inner disk, then we expect both l and s (entropy per baryon) to be roughly constant in the inner disk. (Compare with Seguin 1975

in which s is argued to be roughly constant in a deep convective zone.) In addition, it is easy to derive that the equation of state of radiation-dominated matter with constant s is barotropic. We will neglect the radial component of velocity u_r , where u is the 4-velocity of the fluid. (This idealization is discussed in §5.) Near the star our model resembles a slender accretion disk, while far from the star it resembles a thin disk. In particular, the specific angular momentum $l \equiv -u_\phi/u_0$ is approximately constant near the star, while far from the star the angular velocity becomes Keplerian. We then estimate the disk luminosity an observer would observe as a function of disk model and the angle ζ she makes with the disk polar direction. Here and throughout we use units in which $G = c = 1$, and we use the standard Schwarzschild coordinates t, r, θ, ϕ .

By a model, we simply mean the function relating $\varpi \equiv r \sin \theta$ to the “height” above the equatorial plane of the zero-pressure isobar $z_{\text{surf}} \equiv r \cos \theta$, plus the functions relating ϖ to the values of the specific energy $e \equiv -u_0$, the specific angular momentum l , and the components of acceleration a_r and a_θ at the surface of the disk. For purposes of finding how the luminosity varies with the inner radius of the disk, we need not be concerned with the internal structure of the disk. The disks are parameterized by r_{in} , the inner radius of the disk. For a given r_{in} we find l_0 , the fluid specific angular momentum near the star and calculate the observed luminosity $L_{\text{disk}}^\infty \equiv 4\pi D^2 F_{\text{disk}}^\infty$, where F_{disk}^∞ is the flux from the disk observed at distance D . Eventually we determine (§4) that, even when L_{disk}^∞ approaches the luminosity of bright X-ray sources, some neutron star equations of state allow the neutron star radius to lie within r_{in} .

2.1. Slender accretion disk models

We construct a one-parameter family of disks by modifying standard models of slender disks with constant l . As documented elsewhere (Abramowicz *et al.* 1978, Jaroszyński *et al.* 1980, Chakrabarti 1985), these disks of constant l are toroids with a cusp at inner radius r_{in} . The surface can be described as the function $z_{\text{surf}}(\varpi)$ which attains a maximum z_{max} at ϖ_{max} . The disks we construct have a surface coinciding with the surface of these slender toroids for $\varpi < \varpi_{\text{max}}$;

for $\varpi > \varpi_{\max}$ our disks have a surface given by $z_{\text{surf}}(\varpi) = z_{\max}$. (See Figure 2.) This prescription is equivalent to choosing a function $l(\Omega)$ which satisfies

$$\begin{cases} l = l_0, & \text{near the star;} \\ \Omega \sim r^{-3/2}, & \text{far from the star,} \end{cases} \quad (1)$$

that is, asymptotically Keplerian. A convenient parameter to choose is the cusp radius r_{in} which lies in the interval $[4m, 6m]$. We discuss this prescription further below.

Following Abramowicz *et al.* (1978), we define

$$e \equiv -u_0, \quad l \equiv -u_\phi/u_0, \quad \Omega \equiv u^\phi/u^0. \quad (2)$$

The invariant length $u_\alpha u^\alpha = -1$ implies that e , l , and Ω are related by

$$e = \left(\frac{1 - 2m/r}{1 - \Omega l} \right)^{1/2}. \quad (3)$$

The equation of motion can be written as follows:

$$a_\beta = -\frac{p_{,\beta}}{\rho + p} = (\ln e)_{,\beta} - \frac{\Omega l_{,\beta}}{1 - \Omega l}, \quad (4)$$

where β is r or θ , ρ is density, p is pressure, and a is acceleration. This equation, together with our assumptions about the disk, governs the dynamics of the disk. In particular, the term $(\ln e)_{,\beta}$ is an exact differential, and the term $p_{,\beta}/(\rho + p)$ is an exact differential for a barotropic equation of state, so that the final term is an exact differential and surfaces of constant Ω coincide with surfaces of constant l (Abramowicz 1971). Usually l is a single-valued function of Ω , and we can derive that function from equation (4) given the shape of an isobar of the disk. Or else we can derive the shape of the disk given the function $l(\Omega)$.

In the inner region, where $l = l_0 \equiv \text{const}$, we find from equation (4) that e is constant on the disk surface and equal to its value at the inner cusp r_{in} . The location of the cusp corresponds to the unstable circular orbit, so that we readily obtain

$$l_0 = m^{1/2} r_{\text{in}}^{3/2} (r_{\text{in}} - 2m)^{-1} \quad (5a)$$

$$e_0 = e(r_{\text{in}}) = (r_{\text{in}} - 2m) r_{\text{in}}^{-1/2} (r_{\text{in}} - 3m)^{-1/2} \quad (5b)$$

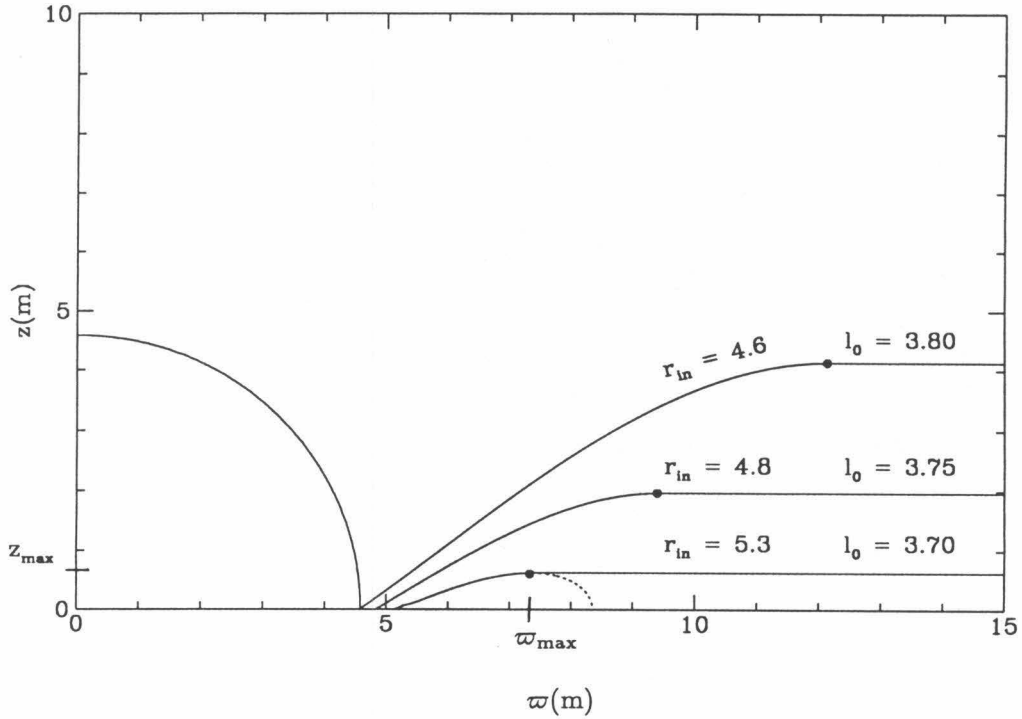


Fig. 2—The dotted line shows the zero-pressure isobar of a toroid with $l = \text{const} = 3.70m$, where m is the mass of the star. The solid line shows how this isobar is extended in §2.1 to form a more nearly realistic accretion disk model. The other two solid lines show accretion disks whose specific angular momenta near the star are $3.75m$ and $3.80m$, respectively. The neutron star surface shown corresponds to a $1.45 M_{\odot}$ star calculated with one of the softer equations of state (Moszkowski). In this case of $l_0 = 3.80m$, the luminosity from the star exceeds the Eddington limit (see Table 2). In this case the luminosity may drive an outgoing wind, so that the observed luminosity is less.

(see, e.g., Shapiro & Teukolsky 1983, p. 346, where their \tilde{l} and \tilde{E} correspond to our le and e). Now, by definition, we have in general

$$\varpi^2 = r^2 - z^2 = \frac{(1 - 2m/r)l}{\Omega} = \frac{e^2 l^2 (r - 2m)}{r e^2 - r + 2m}. \quad (6)$$

The equation of the disk surface in the constant angular momentum region can then be computed from equations (3), (5), and (6), so that we have

$$z_{\text{surf}}(r) = \left(\frac{4mr + 2mr_{\text{in}} - rr_{\text{in}}}{4mr + 2r_{\text{in}}^2 - rr_{\text{in}} - 6mr_{\text{in}}} \right)^{1/2} (r - r_{\text{in}}), \quad r_{\text{in}} \leq r \leq r_{\text{max}}. \quad (7)$$

We obtain ϖ_{max} and z_{max} by setting $\frac{\partial z}{\partial r} = 0$. After some algebra, we obtain

$$\begin{aligned} \varpi_{\text{max}} &= r_{\text{in}} \left[\frac{3r_{\text{in}}^2 - 12mr_{\text{in}} + 16m^2 - r_{\text{in}}d}{(r_{\text{in}} - 4m)(r_{\text{in}} - 4m + d)} \right]^{1/2} \\ z_{\text{max}} &= \frac{r_{\text{in}}(r_{\text{in}} - d)}{2(r_{\text{in}} - 4m)} \left[\frac{12m + d - 3r_{\text{in}}}{r_{\text{in}} - 4m + d} \right]^{1/2}, \end{aligned} \quad (8)$$

where $d = [(5r_{\text{in}} - 12m)(r_{\text{in}} - 4m)]^{1/2}$ and $4m < r_{\text{in}} < 6m$.

In the outer region, both the specific energy e and the specific angular momentum l will vary along the disk surface. By definition we suppose that $z = z_{\text{max}}$. Combining equations (3), (4), and (6), we obtain

$$\left(\frac{\partial l^2}{\partial e^{-2}} \right)_p = -\varpi^2, \quad (9)$$

where the p subscript denotes a derivative along an isobar. Eliminating Ω from equations (3) and (6), we obtain in general

$$l^2 = \varpi^2 [(1 - 2m/r)^{-1} - e^{-2}], \quad (10)$$

and combining with equation (9) yields

$$\begin{aligned} e^{-2} &= \left[\frac{\partial}{\partial \varpi^2} \left(\frac{\varpi^2}{1 - 2m/r} \right) \right]_p = \frac{r^2(r - 3m) + mz_{\text{max}}^2}{r(r - 2m)^2}, \\ \Omega &= m^{1/2} r^{-3/2}, \end{aligned} \quad (11)$$

where we have used $\left(\frac{\partial r^2}{\partial \varpi^2} \right)_p = 1$ for a disk of constant thickness. Equations (11) furnish the specific energy and angular velocity variation over the disk surface in the outer region, and equation (10) gives the specific angular momentum.

We need the components of acceleration on the disk surface for both the inner and outer region. This is obtained by substituting $\Omega/(1 - \Omega l) = e^2 l / \varpi^2$ (obtained from eqs. 3 and 6) into equation (4), so that

$$a_\beta = -\frac{e^2}{2} \left[\left(\frac{1}{e^2} \right)_{,\beta} + \frac{1}{\varpi^2} (l^2)_{,\beta} \right]. \quad (12)$$

To obtain the surface acceleration, we differentiate equation (10) and substitute $\varpi = r \sin \theta$ to obtain

$$\begin{aligned} a_r &= \frac{1}{r} - \frac{(r - 3m)e^2}{(r - 2m)^2}, \\ a_\theta &= -\frac{z}{\varpi} \left[1 - \frac{e^2 r}{r - 2m} \right]. \end{aligned} \quad (13)$$

Note that these equations obtain for both the inner and outer regions. Now we know how to calculate l , e , a_r , and a_θ on the accretion disk surface.

2.2. Disk luminosity

In the previous subsection we constructed a family of disks parameterized by r_{in} . In §2.2 we calculate the *apparent* luminosity observed far away at an angle ζ with respect to the polar axis of the disk, that is, the luminosity she would calculate $L_{\text{disk}}^\infty = 4\pi D^2 F_{\text{disk}}^\infty$. We do this by tracing geodesics from the observer to the disk surface and relating the intensity at the observer to the intensity in a frame co-moving with the disk. Since the disk is radiation-dominated, a co-moving observer near the disk surface would observe an isotropic radiation field in the outgoing direction with flux equal to the local Eddington flux. By integrating intensity over impact parameter, we calculate numerically the quantity L_{disk}^∞ as a function of r_{in} .

Let us say the observer is located at $(r, \theta, \phi) = (D, \zeta, 0)$, where $D \gg m$. We introduce a second system of coordinates (r, χ, ψ) rotated relative to the coordinates (r, θ, ϕ) , such that χ and ψ are the azimuthal and polar angles defined relative to the axis connecting the origin and the observer. (In equations (19) and (20) we will refer to the new coordinate basis as the “primed” basis, so no confusion will result.) See Figure 3.

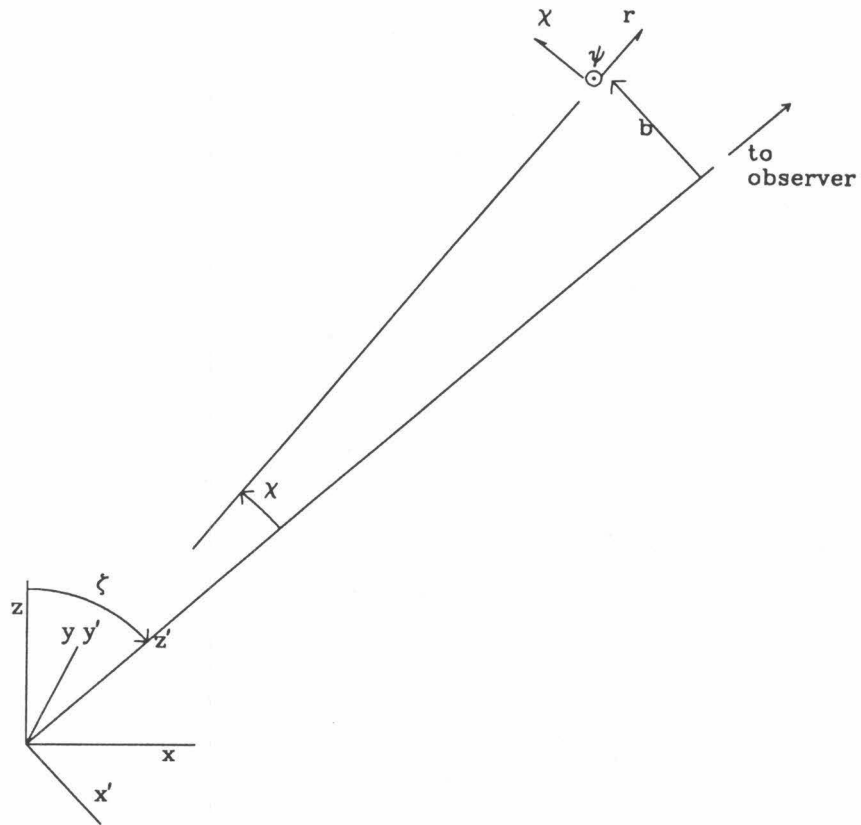


Fig. 3—Geometry for calculating null geodesics in §2.2. The z -axis is the symmetry axis for the accretion disk, and the observer is located far away along the z' -axis at an angle ζ from z . The integration to obtain flux in §2.2 is over impact parameter b and angle ψ .

Photons arrive at the observer's telescope parallel to the z' -axis and are characterized by an impact parameter $b = D \sin \chi$ and angle ψ . We can write the apparent luminosity as follows:

$$L_{\text{disk}}^{\infty} = 4\pi D^2 F_{\text{disk}}^{\infty} = 4\pi \int \int I^{\infty}(b, \psi) b \, db \, d\psi. \quad (14)$$

where F_{disk}^{∞} is the observed flux from the disk and $I^{\infty}(b, \psi)$ is the frequency-integrated intensity of photons in the z' direction characterized by impact parameter b and angle ψ .

In order to relate $I^{\infty}(b, \psi)$ to the conditions on the disk, we first trace a null geodesic with impact parameter b back to the accretion disk. The tracing along a geodesic is accomplished by numerically integrating the equations (see, e.g., Misner *et al.* 1973, hereafter MTW, pp. 672-673)

$$\begin{aligned} \frac{d^2 u}{d\chi^2} &= (3mu - 1)u, \\ u(\chi = 0) &= 0, \\ \frac{du}{d\chi}(\chi = 0) &= \frac{1}{b}, \end{aligned} \quad (15)$$

where $u \equiv 1/r$. At each integration step we convert (r, χ, ψ) to coordinates (r, θ, ϕ) and check if we entered the disk, that is, we have entered the disk if

$$r^2 \sin^2 \theta > \frac{e_0^2 l_0^2 (r - 2m)}{r e_0^2 - r + 2m} \quad (16)$$

(see eq. 6) or if

$$r \cos \theta < z_{\text{max}} \quad \text{and} \quad r \sin \theta > \varpi_{\text{max}}. \quad (17)$$

Thus each ordered pair (b, ψ) is related to a point on the disk (r, θ, ϕ) by a single geodesic, and from §2.1 we know the values of l , e , a_r , and a_{θ} there. For the rest of this section r , θ , and ϕ will be functions of b and ψ corresponding to the point where the null geodesic labeled by b, ψ intersects the surface of the disk.

We can now relate $I^{\infty}(b, \psi)$ to known parameters on the disk as follows: We know that I_{ν}/ν^3 is a Lorentz invariant and a constant along a null geodesic

(Liouville theorem, see, e.g., MTW, pp. 583-588). Thus we have

$$I^\infty(b, \psi) \equiv \int d\nu^\infty I_{\nu^\infty}^\infty(b, \psi) = \left(\frac{\nu^\infty}{\nu^{\text{co}}}\right)^4 \int d\nu^{\text{co}} I_{\nu^{\text{co}}}^{\text{co}}(b, \psi) \equiv \left(\frac{\nu^\infty}{\nu^{\text{co}}}\right)^4 I^{\text{co}}(b, \psi), \quad (18)$$

where ν^∞ is the frequency of a photon observed by the observer at infinity, ν^{co} is the frequency of that photon observed by a person co-moving with the disk and I^{co} is the corresponding integrated intensity. Next we derive an expression for the ratio $\nu^{\text{co}}/\nu^\infty$. We note that, since $\frac{\partial}{\partial t}$ and $\frac{\partial}{\partial \phi}$ are Killing vector fields and k (the photons' wave vector) satisfies the geodesic equation $\nabla_k k = 0$, k_0 and k_ϕ must be constant along the geodesics (see, e.g., MTW, pp. 650-651). Thus, we evaluate

$$\nu^\infty = -u^\infty \cdot k^\infty = -k_0, \quad (19)$$

where we have used $u^\infty \equiv (1, 0, 0, 0)$, and

$$\nu^{\text{co}} = -u^{\text{co}} \cdot k^{\text{co}} = -\frac{er}{r-2m}k_0 - \frac{le}{\varpi^2}k_\phi, \quad (20)$$

where we have used $u_\alpha \equiv (-e, 0, 0, le)$.

We find a relationship between k_ϕ and ν^∞ by making a transformation from the coordinates (t, r, θ, ϕ) to the coordinates (t, r, χ, ψ) which we will call the "primed" coordinates. Thus we have

$$k_\phi = L_\phi^{\mu'} k_{\mu'}. \quad (21)$$

Now $L_\phi^{t'} = L_\phi^{r'} = 0$ and $k_{\psi'} = 0$ and $k_{\chi'} = b\nu^\infty$, as can be seen from Figure 3. We evaluate $L_\phi^{\chi'}$ by taking the partial derivative of χ with respect to ϕ and evaluating at the location of the observer, so that

$$L_\phi^{\chi'} = \sin \zeta \sin \psi. \quad (22)$$

Combining with equations (19), (20), and (21) yields

$$\frac{\nu^{\text{co}}}{\nu^\infty} = \frac{er}{r-2m} - \frac{leb \sin \zeta \sin \psi}{\varpi^2}. \quad (23)$$

Because the disk is radiation-pressure dominated, we assume an observer co-moving with the fluid sees an isotropic radiation field whose flux provides the

force required to maintain stationary orbits at the surface of the disk. (This is analogous to a local Eddington limit.) Thus

$$I^{\text{co}}(b, \psi) = \frac{F^{\text{co}}(b, \psi)}{\pi} = \frac{|\mathbf{a}|}{\pi \kappa_{\text{T}}} = \frac{(a \cdot a)^{1/2}}{\pi \kappa_{\text{T}}}, \quad (24)$$

where $F^{\text{co}}(b, \psi)$ is the total flux observed by a co-moving observer near the surface of the disk, κ_{T} is the opacity due to Thomson scattering, and $|\mathbf{a}|$ is the magnitude of the acceleration 3-vector in the co-moving frame, which in this case is equivalent to $(a \cdot a)^{1/2}$, since a is orthogonal to u . [Again, α -disk theory (Novikov & Thorne 1971) indicates that Thomson scattering dominates the opacity.]

We evaluate $L_{\text{disk}}^{\infty}(\zeta, r_{\text{in}})$ by numerically integrating the expression in equation (14). We obtain $I^{\infty}(b, \psi)$ by combining equation (18) with equations (23) and (24). For the resulting expression we need r , θ , l , e , a_r , and a_{θ} evaluated at the point where the geodesic corresponding to (b, ψ) touches the disk. These are obtained by the procedure described in the fourth paragraph of this subsection and from the procedures outlined in §2.1.

2.3. Results for disk luminosity

The results of these calculations are shown in Tables 1 and 2. Table 1 shows the quantity $L_{\text{disk}}^{\infty}/L_{\text{Edd}}$ as a function of r_{in} and ζ , where $L_{\text{Edd}} = 4\pi m \kappa_{\text{T}}^{-1}$. The first 6 columns of Table 2 show parameters discussed in §2.1 (column 4 shows the position of the pressure maximum), while column 7 contains the value of $L_{\text{disk}}^{\infty}/L_{\text{Edd}}$ which is a weighted average over ζ of the values in Table 1. (Columns 8 and 9 will be discussed in §2.4.) Especially note the relationship between r_{in} and $L_{\text{disk}}^{\infty}/L_{\text{Edd}}$, that r_{in} decreases as L_{disk}^{∞} and L_{tot}^{∞} (column 9, calculated in §2.4) increase. This is a general feature of any family of disks in which the specific angular momentum is constant near the neutron star, which we expect if the inner region has rapid mixing of rings of fluid without strong viscous torques.

This feature is preserved even if we perturb the inner region somewhat from the condition $l = \text{constant}$. We used the relation

$$l - l_0 = \epsilon(\Omega - \Omega_0) \quad (25)$$

TABLE 1

Apparent Disk Luminosity^a

ζ	r_{in}/m						
	5.63	5.51	5.27	5.15	4.97	4.84	4.58
0°	0.021	0.037	0.089	0.128	0.216	0.317	0.648
30°	0.018	0.033	0.080	0.115	0.195	0.288	0.593
45°	0.018	0.033	0.080	0.115	0.193	0.284	0.568
60°	0.017	0.031	0.075	0.108	0.179	0.261	0.513
88°	0.004	0.008	0.031	0.046	0.066	0.109	0.177

^a This is equivalent to $L_{\text{disk}}^{\infty}(\zeta, r_{\text{in}}) = 4\pi D^2 F_{\text{disk}}^{\infty}(\zeta, r_{\text{in}})$, where F_{disk}^{∞} is the flux at infinity coming from the disk, ζ is the angle the observer makes with the axis of the disk, and r_{in} is the inner radius of the disk.

TABLE 2

Parameters and Luminosities Associated with Disk Models

$\frac{r_{\text{in}}}{m}$	$\frac{l_0}{m}$	e_0	$\frac{r_{\text{pres}}}{m}$	$\frac{z_{\text{max}}}{m}$	$\frac{\omega_{\text{max}}}{m}$	$\frac{L_{\text{disk}}^{\infty}}{L_{\text{Edd}}}$	$\frac{L_{\text{star}}^{\infty}}{L_{\text{Edd}}}$	$\frac{L_{\text{tot}}^{\infty}}{L_{\text{Edd}}}$
(1)	(2)	(3)	(4)	(5)	(6)	(7)	(8)	(9)
5.63	3.68	0.9434	6.41	0.16	6.49	0.014	0.042	0.056
5.51	3.685	0.9439	6.57	0.27	6.72	0.026	0.079	0.105
5.27	3.70	0.9455	6.92	0.60	7.33	0.066	0.209	0.275
5.15	3.71	0.9466	7.11	0.84	7.72	0.095	0.309	0.404
4.97	3.73	0.9491	7.43	1.35	8.52	0.156	0.540	0.696
4.84	3.75	0.9518	7.72	1.96	9.40	0.232	0.861	1.093
4.58	3.80	0.9592	8.35	8.09	16.33	0.454	2.07	2.53

TABLE 3

Observed Disk Luminosity
for Perturbed Models^a

	r_{in}/m			
	ϵ	5.63	4.84	4.58
0	0.017	0.261	0.513	
0.01	0.014	0.251	0.477	
0.1	0.013	0.241	0.471	

^a These disk luminosities L_{disk}^{∞} are calculated for $\zeta = 60^\circ$. (See eq. 25 in §2.3.)

to build the initial toroids which were then extended to infinity in the same way as before. In equation (25) l_0 and Ω_0 are the values of l and Ω at the inner radius of the disk, and ϵ is a small perturbation parameter. We calculated the disk luminosity $L_{\text{disk}}^{\infty}(\zeta = 60^\circ)$, and the results are shown in Table 3. Variations in ϵ are seen not to cause large variations in $L_{\text{disk}}^{\infty}/L_{\text{Edd}}$.

2.4. Neutron star luminosity

We can obtain an estimate for the luminosity coming from the star if we make some simple idealizations. We assume that material drips from the inner radius of the disk onto the nonrotating star, and we assume the internal energy advected by the material onto the star is negligible, since most of this energy is in the photon field and is released before the material contacts the star. Then the specific energy of the material at the inner radius is e_0 (see Table 2), and that of the material at the surface of the star is $e_{\text{star}} = (1 - 2m/R)^{1/2}$, so that $e_0 - e_{\text{star}}$ is the energy released per mass after the material is dripped from the disk. If we ignore reprocessing by the disk of photons from the star, we may simply write

$$\frac{L_{\text{star}}}{L_{\text{disk}}} = \frac{e_0 - e_{\text{star}}}{1 - e_0}, \quad (26)$$

where we will use L_{disk}^{∞} from column 7 of Table 2 as an average value of flux from the disk. For the calculation of e_{star} , we use $m = 1.45 M_{\odot}$ and a radius given by

Arnett & Bowers (1977) for the Bethe-Johnson V equation of state (that is, D, in their paper) $R = 10.6$ km. We tabulate the resulting estimates of $L_{\text{star}}^{\infty}/L_{\text{Edd}}$ and $L_{\text{tot}}^{\infty}/L_{\text{Edd}}$ in columns 8 and 9 of Table 2.

The thing to note in Table 2 is that r_{in} decreases as L_{tot}^{∞} increases, so that, for example, the decrease between the first and fourth entries of the table is on the order of $0.48m \approx 1$ km for a $1.45 M_{\odot}$ neutron star. This feature, that the inner edge of the accretion disk moves inwards as luminosity increases, is a feature also of some α -disk models with low Shakura-Sunyaev parameter α (see Matsumoto *et al.* 1984 and Abramowicz *et al.* 1988). In these latter studies it is the sonic point which moves inward as the luminosity increases.

3. Boundary layer formation

In the previous section, we showed that the inner radius of the accretion disk is a decreasing function of mass accretion rate for a star and an accretion disk with an accretion gap. We now consider what happens when the disk touches the star and a boundary layer forms and speculate upon the implications for the two-color diagram.

The published two-color diagrams are the result of convolving the X-ray spectrum arriving at earth with the variable instrumental responses in the different energy channels. It is not possible to infer the emitted spectra unambiguously (van der Klis 1991, private communication; see, however, Hasinger *et al.* 1990). Furthermore, there is variation in the Z-diagrams from source to source. For this reason we shall make a very simple model in which there are three spectral components, of low, medium and high characteristic X-ray energy, and describe qualitatively their expected variation. The low energy component (~ 1 -3 keV), which we call L , we associate with the accretion disk. We can calculate an approximate upper bound for temperature on the surface of the disks by finding the maximum flux in equation (24) and assuming approximate local thermodynamic equilibrium. For the disk with $r_{\text{in}} = 5.27m$ in Table 2, using $m = 1.45 M_{\odot}$, we obtain $T_{\text{max}} \sim 12 \times 10^6$ K, so that typical photon energies are $\lesssim 3$ keV. The medium energy component (~ 3 -6 keV), which we call M , we associate with the stellar

surface. The high energy component ($\sim 6\text{-}20$ keV), H , we presume to originate from either the impact of falling material or from the boundary layer. (Compare with Sunyaev & Shakura 1986.)

When the source is on the HB, and the accretion rate is low enough for an accretion gap to form, we envisage that instabilities in the inner disk allow irregular, non-axisymmetric radial flow in the vicinity of the marginally stable orbit. Short streams of gas are accelerated toward the stellar surface. Since the accretion gap is likely to be quite small, the tangential velocity greatly exceeds the radial velocity, and the gas therefore strikes the stellar surface with near grazing incidence. A hard component arises when the accreting matter is decelerated through Coulomb collisions with the atmospheric electrons. In this case, a hot (~ 20 keV), optically thin layer is formed at the top of the atmosphere, which Comptonizes the softer X-ray flux emerging from below (*cf.* Zel'dovich & Shakura 1969, Fig. 1, Alme & Wilson 1973). This effect is amplified when the infalling matter enters at an oblique angle (*cf.* Kluźniak & Wilson 1991). Hot electrons may also be produced through shocks in the infalling matter. (See, however, also Walker 1992.) The resulting hard photons make up the H component. We propose that a fixed fraction, of order half, of the hard radiation is partially thermalized and re-emitted by the star as the M component. (The relative fluxes observed will depend upon the orientation.) On the HB, the M and H components therefore both increase with α relative to the L disk component. (See Figure 4.)

A boundary layer forms on the NB. The structure of accretion disk boundary layers is a difficult and controversial issue. Early analyses appropriate to white dwarf interfaces in cataclysmic variables (e.g., Pringle 1977, Pringle & Savonije 1979, Tytenda 1981) led to the estimate $\Delta \sim h^2/R$ for the boundary layer thickness, where h is the disk thickness. This estimate comes about from balancing the centrifugal force with the pressure gradient. If the viscous stress scales linearly with the density and has a coefficient of kinematic viscosity ν , then the radial velocity through the boundary layer adjusts to a value $\sim \nu/\Delta$.

The structure of the boundary layer above a critically accreting neutron star

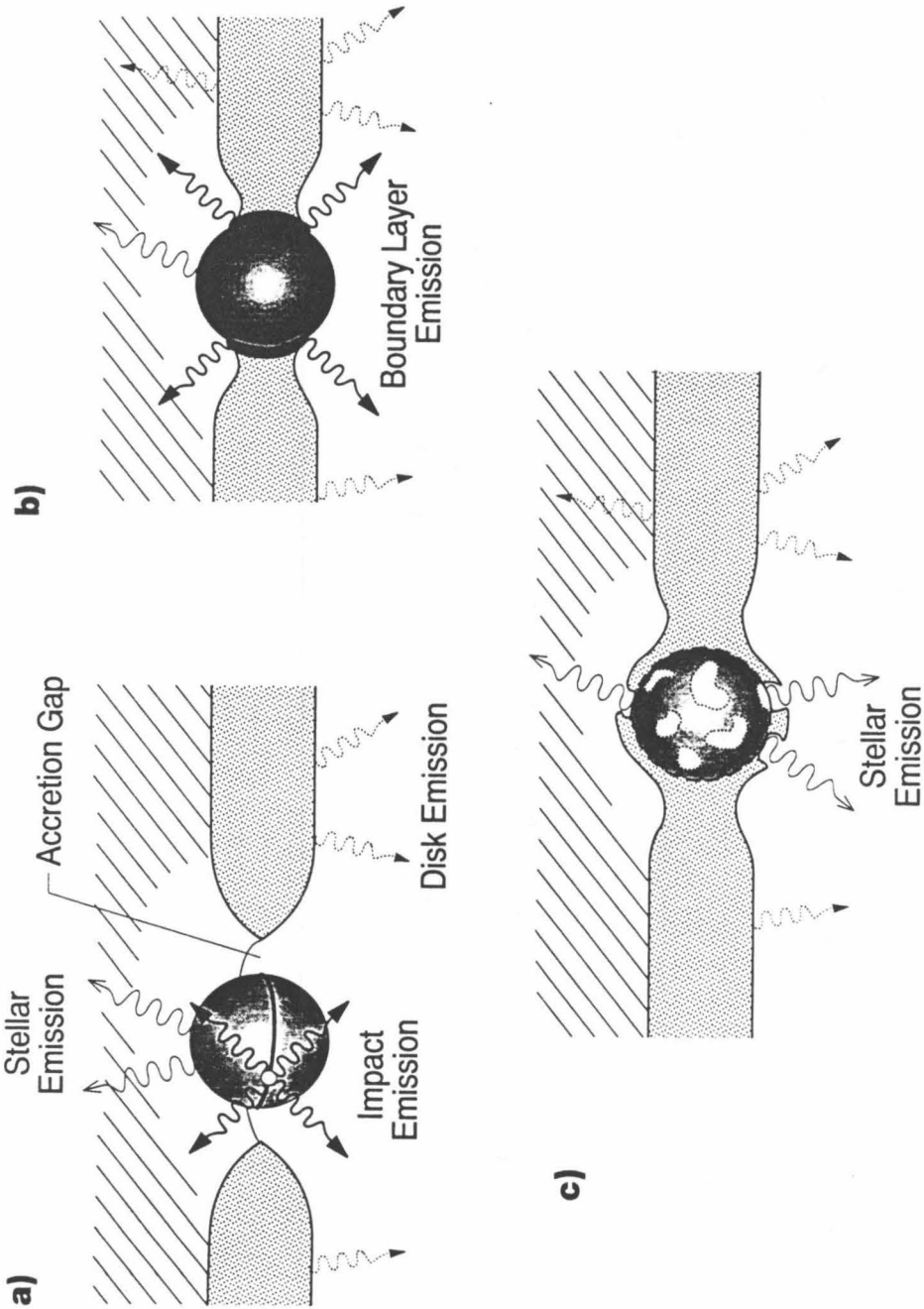


Fig. 4—Three modes of accretion onto a neutron star: a) Horizontal branch: Parcels of gas fall at irregular intervals through a narrow accretion gap onto the surface of the star emitting hard X-rays. b) Normal branch: The inner edge of the disk touches the star and forms a boundary layer. As the accretion rate increases, the disk thickens, the X-rays soften, and the proportion of stellar thermal radiation decreases. c) Flaring branch: The accreting gas envelops the star, supported by radiation pressure in a thick, convectively unstable atmosphere. The radial flux at the stellar surface may exceed the Eddington limit and drive a stellar wind.

is even more complex. As mentioned in §2, the fluid will be radiation pressure dominated and quite optically thick to Thomson scattering. (Fujimoto & Hoshi 1985, Shakura & Sunyaev 1988). The transport of radiation will be largely responsible for determining the thickness. We suspect that the boundary layer will be turbulent with a laminar viscous sublayer close to the neutron star in which radiative viscosity is responsible for lateral momentum transport. On dimensional grounds, we propose that

$$\Delta \sim h \sim \left(\frac{L}{L_{\text{Edd}}} \right) R, \quad (27)$$

where L_{Edd} is the Eddington luminosity. Therefore, the boundary layer covers an increasing fraction of the stellar surface, as the spectral parameter α increases. The energy released within the boundary layer will propagate outward through the disk by either radiative transport or the application of viscous torque. The radiation is likely to be softened by repeated Compton scattering. Much of the energy released by the boundary layer will therefore emerge in the M and even the L band instead of the H band. This can account for the abrupt decline in H/M , and the slight decline in M/L . The NB presumably ends at the soft apex when the star is mostly covered.

Finally, on the FB, H band radiation produced close to the stellar surface in the strong shear flow may be able to escape directly via convective overturn. The L component decreases as the accretion rate increases and the effective temperature increases. Again, qualitatively, these two effects can account for the FB portion of the Z-diagram (*cf.* van der Klis 1989 and references cited therein).

4. Mass-radius relationship for a neutron star

Kluźniak and Wagoner (1985) catalogued equations of state which would allow a $1.4 M_{\odot}$ neutron star to have a radius less than $6m$. They concluded that indeed neutron stars may lie within the marginally stable Keplerian orbit and that a theory of LMXB's involving an accretion gap would then be appropriate. Alternatively, they argued that, if we find evidence for the existence of an accretion gap, then we can draw definite conclusions about the softness of the equation of

state for neutron star material. In this study we take into consideration the fact that for the luminous LMXB's which exhibit QPO's we expect the accretion disk to be a slender disk (not thin), so that the inner radius of the disk is smaller than $6m$. This is a more restrictive criterion for determining what equations of state may allow an accretion gap to exist. This is illustrated in Figure 5, in which is shown neutron star mass versus radius for several equations of state from Arnett & Bowers (1977). Also shown are the lines representing $m = 1.45 M_{\odot}$, $r = 4m$, and $r = 6m$, as well as lines of constant L_{tot}^{∞} for several entries in Table 2. If we make the reasonable assumption that the accretion disk has a luminosity at least $0.4 L_{\text{Edd}}$ at the hard apex, and if the neutron star has a mass on the order of $1.45 M_{\odot}$, then the equations of state which allow an accretion gap are Arp, Pandn, Mos, and BJV, i.e., those softer than BJI.

There are several effects which we have not considered which make us cautious about the preceding result, and we discuss these effects in the remaining paragraphs of this section. The former two effects tend to decrease our estimate of r_{in} , while the latter two tend to increase it.

First we consider the effect of rotation of the neutron star. To date, no Z-source has exhibited a neutron star rotational frequency. If rotation is ever detected, then rotational flattening may further restrict the conditions for the existence of an accretion gap. We use the calculation in Hartle & Thorne (1968) to estimate the marginal increase of equatorial radius as

$$\frac{\delta R}{R} \approx 6 \times 10^{-4} \left(\frac{P}{10 \text{ ms}} \right)^{-2}, \quad (28)$$

assuming a Bethe-Johnson V equation and $m = 1.45 M_{\odot}$. Also the position of the (co-rotating) marginally stable circular orbit is less than $6m$ in the Kerr geometry, so that

$$r_{\text{ms}} - 6m = -0.28 \text{ km} \left(\frac{P}{10 \text{ ms}} \right)^{-1}. \quad (29)$$

(See Kluźniak & Wagoner 1985 and also Hartle & Thorne 1968 for the calculation of a .)

A second effect is the displacement of the cusp from our calculated value due to the presence of central radiation. In Appendix 1 we estimate the size of

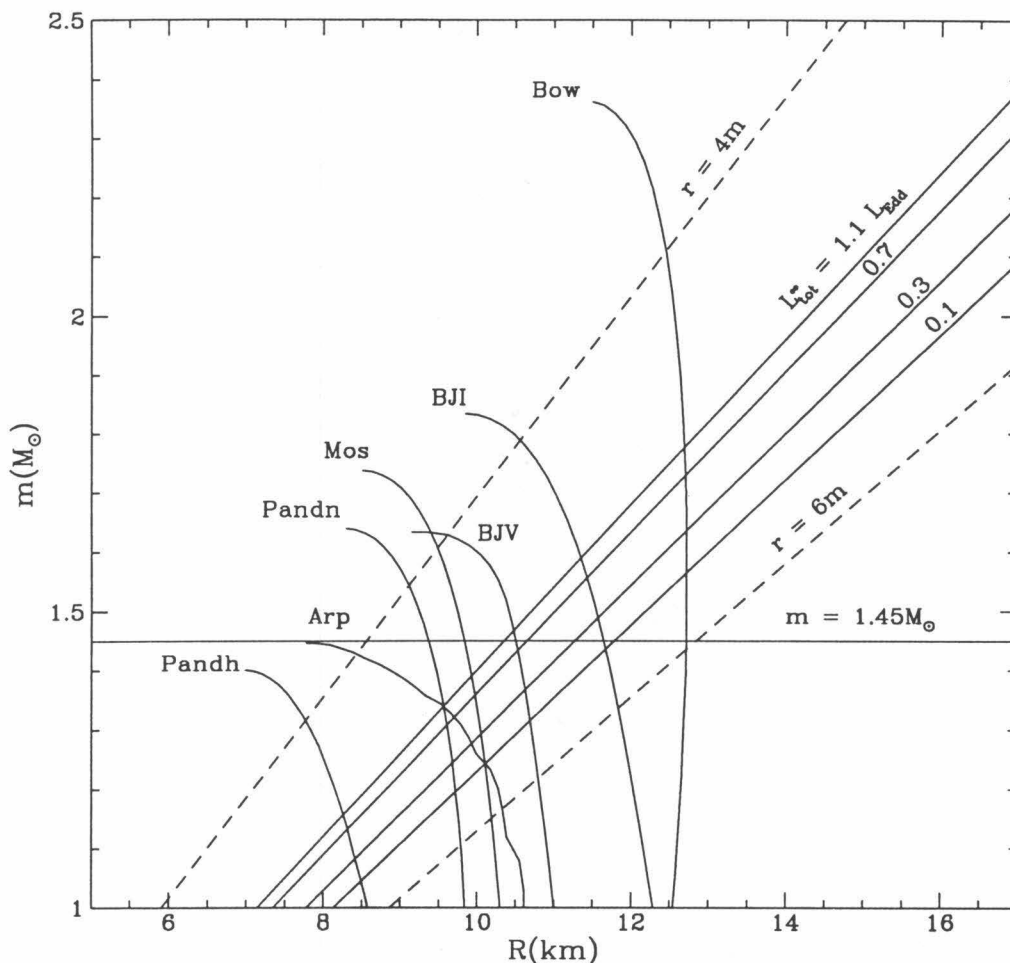


Fig. 5—Mass versus radius for a neutron star calculated from various softer equations of state. The mass $m = 1.45 M_{\odot}$, (i.e., 2.2 km) is shown, as well as the radius of the marginally stable circular orbit $r = 6m$, the radius of the marginally bound orbit $r = 4m$, and lines of constant r_{in}/m for several entries in Table 1. These last lines are labeled by the total apparent luminosity from the system L_{tot}^{∞} . Mass accretion rate \dot{M} is related to L_{tot}^{∞} by $L_{\text{tot}}^{\infty} = \dot{M}(1 - e_{\text{star}})$, where e_{star} is the specific energy of material on the surface of the star. The key for the equations of state (with Arnett-Bowers notation in parentheses) is as follows: Pandh (B): Pandharipande (1971b), Reid soft core, hyperons included; Arp (F): Arponen (1972), Thomas Fermi interaction; Pandn (A): Pandharipande (1971a), Reid soft core, neutrons only; Mos (E): Moszkowski *et al.* (1974), Reid soft core; BJI (C): Bethe, Johnson I (1974), Reid soft core; BJV (D): Bethe, Johnson V (1974), Reid soft core; Bow (O): Bowers, Gleeson, Pedigo (1975), relativistic.

this effect by determining the location of the marginally stable circular orbit in an optically thin regime with central isotropic radiation. We find that the marginally stable circular orbit moves to smaller radii, such that

$$r_{\text{ms}} \sim 6m - 2.1\xi m, \quad (30)$$

where r_{ms} is the radius of the marginally stable circular orbit and $\xi \equiv \kappa_{\text{T}} L^{\infty} / 4\pi m$ is the coefficient in column (9) of Table 2. For a $1.4 M_{\odot}$ star and $\xi = 0.275$ (third entry of Table 2), we obtain $\Delta r \sim 1.2$ km.

Thus far we have been idealizing the inner radius of the accretion disk to lie at the location of the cusp. Unlike the surface of the star, the surface of the disk is somewhat fuzzy, especially since the effective potential near the cusp is soft. Thus we suspect that the actual inner edge of the disk is displaced from the cusp. It is difficult to model when true contact is made at the hard apex, since this depends sensitively on the structure of the accretion disk. We present here two effects which would result in the displacement of the inner edge from the cusp.

The third effect, this also due to central radiation, has the effect of moving the inner edge of the accretion disk outside the cusp radius. The central radiation will scatter off the material on the inner edge of the disk, producing a radiation drag and an inspiral of material at the cusp (*cf.* the Poynting-Robertson effect in, e.g., Rybicki & Lightman 1979). We can estimate the effect this has on the inner edge of the disk by looking at the Thomson penetration depth into the disk. This gives an idea as to where the disk is “thick” enough to be unaffected by radiation. Inside the inner edge of the disk particles will be spiraling inward and transferring angular momentum to the radiation field, so that radiation reaching the disk will no longer be isotropic. Appendix 2 gives an estimate of the penetration depth, so that for $m = 1.45 M_{\odot}$,

$$r_{\text{T}} - r_{\text{in}} \sim 0.6 \text{ km}, \quad (31)$$

where r_{T} is the equatorial radius at which the scattering optical depth approaches 1 and r_{in} is the cusp radius. This difference does not change our conclusion that a neutron star may lie inside of a thick accretion disk, although it will alter slightly our prediction as to which equations of state are allowable if our model is correct.

Also, as for the fourth effect, it is possible that these slender accretion disks do not fill equipotentials up to the equipotential which contains the cusp. If the star accretes not by material dripping over the cusp but by material being slung into the star from the inner disk due to some instability, then again the inner radius of the disk may lie at a greater radius than we have been using.

So far we have been referring to the Newtonian Eddington limit $L_{\text{Edd}} = 4\pi m \kappa_{\text{T}}^{-1}$. The general relativistic Eddington limit can be calculated for a given radius r by setting the local luminosity to the local acceleration of a stationary observer multiplied by $4\pi r^2 \kappa_{\text{T}}^{-1}$. The resulting luminosity at infinity is given by

$$L_{\text{GR,Edd}}^{\infty} = 4\pi m (1 - 2m/r)^{1/2} \kappa_{\text{T}}^{-1} \sim 0.8 L_{\text{Edd}} \quad (32)$$

for r on the order of the neutron star radius for the softer equations of state. If the star luminosity L_{star}^{∞} gets much larger than this, then the neutron star surface can no longer be said to be at the Arnett-Bowers value, so that we have restricted the entries in Table 2 to having $L_{\text{star}}^{\infty} \lesssim 0.8 L_{\text{Edd}}$.

5. Discussion

In this paper, we considered the hypothesis that QPO sources be identified with slowly rotating, weakly magnetized ($B \lesssim 10^7$ G) neutron stars undergoing near critical accretion. We proposed that the hard apex is associated with closing of the accretion gap. This proposal requires that a neutron star lie within the inner edge of a slender accretion disk radiating at a substantial fraction of the Eddington limit. We showed that for a typical stellar mass of $1.45 M_{\odot}$ and a system radiating at $0.7 L_{\text{Edd}}$, the star will lie within the inner edge of the accretion disk if the equation of state is not significantly harder than the Bethe-Johnson V equation of state. Substantially harder equations of state would not be consistent with this model. By specifying a simple analytical prescription for the disk angular momentum and calculating the luminosity of the system as a function of inner disk radius, we established that the inner edge of the disk moves inward as mass accretion increases. Thus it is reasonable that the accretion gap would close as mass accretion increases from the HB to the NB. To account for the

gross phenomenology of the two color diagram, we proposed a three component model for the spectrum involving the star, the disk and the impact emission from gas falling through the accretion gap.

This physical description of the accretion flow is simplistic and ignores many complications which may be features of real flows. Specifically, in creating disk models we assumed that the specific angular momentum l is roughly constant in the inner disk. This assumption is valid if dynamical instabilities interchange rings of constant l in the inner disk, thus rendering l roughly constant (see discussion at the beginning of §2.) In §2.3 we perturbed the distribution of l in the disk and found that the calculated luminosity was surprisingly robust. These models depend on only one parameter, r_{in} , which can be directly related to the mass accretion rate. One could construct a more general class of models having independent parameters r_{pres} (the radius of the pressure maximum) and z_{max} (the height) in addition to r_{in} . It may be possible to contrive models in which r_{in} increases with \dot{M} , which would be incompatible with our picture of the various modes of accretion. We propose, however, that physical disks have the qualitative property that r_{in} decreases with increasing \dot{M} .

Another concern is that we have neglected the magnetic stress associated with a magnetosphere. A surface field strength of less than $\sim 3 \times 10^8$ G will ensure that the Reynolds' stress associated with orbiting disk overwhelms magnetic stress. The Low-Mass X-ray Binaries, from which QPOs are drawn, are an old population and there is no physical difficulty with supposing that any primordial dipole moment will have long decayed. The observational position, however, remains quite ambiguous. Some millisecond pulsars have estimated surface dipole magnetic field as small as $\sim 3 \times 10^8$ G (e.g., Bhattacharya & van den Heuvel 1991), whereas fields greater than 10^{12} G are reported for some γ -ray bursters (Murukami *et al.* 1988) (that is, if these are indeed old Galactic neutron stars at all, Meegan *et al.* 1992). If our model is verified, this would place a strong limit on the stellar magnetic fields in QPO sources.

In computing our disk models and locating the disk cusp, we have supposed

that the gas is accelerated by radiation escaping solely from the disk, ignoring the influence of the radiation originating from the star. We have sought to estimate the size of the effect of radiation from the neutron star on the location of the inner radius of the disk. In Appendix 1 we estimate that radiation drag reduces the radius of the effectively marginally stable orbit, by ~ 1 km, which will probably bring the optically thin portion of the disk closer to the star. In Appendix 2 we estimate the effect of radiation stripping away the inner surface of the disk by radiation drag, so that the "hard" surface of the disk lies ~ 0.6 km outside the cusp radius. This enlarges slightly the class of neutron star equations of state which would allow an accretion gap to form. These effects are not large enough to change the qualitative aspects of our discussion, although they do change somewhat the class of neutron star equations of state which will allow for an accretion gap.

We have not addressed the topic of instabilities in these models. Thick disks have been shown to be subject to instability of global nonaxisymmetric modes (Papaloizou & Pringle 1984, Goldreich, Goodman & Narayan 1989). We found that our disks are surprisingly thin. The extent to which these instabilities are relevant to thin disks is unclear (Hawley 1991). This is certainly an issue which deserves more attention.

Neither have we discussed the phenomenology of low-frequency oscillation and noise which is associated with these objects. Our model provides a natural site for the production of low-frequency noise observed on the HB. It is natural to associate the noise with the impact emission, reflecting the stochastic dripping of gas through the accretion gap. This is replaced by a steadier inflow as the boundary layer forms and thickens on the NB.

The constancy of the frequency of the NB oscillation (6-8 Hz) among several sources and its relative stability with respect to changes in mass accretion rate make it natural to associate the NB oscillation with stellar modes, since the properties of the disk and of the accretion gap depend more sensitively on \dot{M} . The frequencies of most stellar modes are ~ 1 kHz, far in excess of the observed oscillation frequency, although the oscillation may be associated with some lower

frequency g-modes or with some nonadiabatic dynamical process, such as the progress of a nuclear burning front or the breaking of a wave of material over the stellar surface. In either case there are two major considerations: the excitation and damping of the mode and the coupling of that mode to the production of luminosity so that it can be observed. The excitation of stellar modes may be strongly connected to the presence of a boundary layer, and so this may explain why the NB oscillation is not observed on the HB. The coupling of the mode to the production of luminosity is necessary because the energy contained in the modes themselves is far too small to account for the $\sim 2\%$ oscillation of X-ray flux. It may be that the mode acts as a kind of clock which modulates some process which creates or amplifies photons. For instance, the pulsation may involve a radial displacement which perturbs the boundary layer. The emission from the boundary layer is probably enhanced by the Doppler shift of photons emitted from gas moving at mildly relativistic speeds, particularly if the object is observed at low latitude. Modulations of the Doppler factor may give rise to $\sim 2\%$ oscillation in the observed flux.

The most striking characteristic of HB oscillation is the correlation of frequency with the magnitude of the flux (and thus mass accretion rate). In our model, this translates into requiring that the preferred frequency increase in a reproducible manner as the inner edge of the disk approaches the star. One possibility is that the HB oscillation is attributable to orbital Lense-Thirring or Newtonian precession in the nonspherical spacetime around a rapidly spinning neutron star. Modulation of the Doppler factor again may provide a natural amplifier. It is difficult, however, to account for the full variation in HB QPO frequency in this manner.

Perhaps the best hope for testing this assignment of QPO sites observationally lies with characterising the oscillatory components at different X-ray wavelengths. In principle, this should be a good diagnostic since, if we associate the HB oscillation with the gap and the NB oscillation with the star, then we expect that the former should have a harder spectrum than the latter. If, further, the softest

X-rays originate from the star, then they should be relatively unmodulated. However, electron scattering may blur some of these distinctions. We plan to assess the relative merits of different explanations for the HB and NB oscillations in a more general manner in a forthcoming paper.

The authors would like to acknowledge Peter Mészáros, Fred Lamb, Günther Hasinger, and Michiel van der Klis for much helpful discussion. They also wish to thank Lars Bildsten, Curt Cutler, and Alice Quillen for discussion and critical reading of this manuscript. We also wish to thank the anonymous referee for his comments, which resulted in some revision of this manuscript. Support under NSF grant AST 89-17765 and NASA grant NAGW 2372 is gratefully acknowledged.

Appendix 1

To obtain a measure of the size of the effect which radiation pressure from the star may have on the location of the inner radius of the accretion disk, we will consider a parcel of plasma moving in a Schwarzschild geometry and introduce radiation pressure as a perturbation. Then we will look for the marginally stable orbit.

If the luminosity of the central object at infinity is L^∞ , then a stationary observer at radius r observes flux

$$F^{\text{st}} = \frac{L^\infty}{4\pi r^2} \left(1 - \frac{2m}{r}\right)^{-1}, \quad (A1)$$

where one factor of $(1 - 2m/r)^{-1/2}$ comes from the time dilation factor and the other from the gravitational redshift. The parcel moves with velocity $u_\alpha \equiv (-e, 0, 0, le)$ in t, r, θ, ϕ coordinates. If we boost into the frame of the parcel of plasma, we obtain the flux

$$F^{\text{plas}} = \left(1 + \frac{l^2 e^2}{r^2}\right)^{1/2} e \left(1 - \frac{2m}{r}\right)^{-1/2} F^{\text{st}}, \quad (A2)$$

where the factor $e \left(1 - \frac{2m}{r}\right)^{-1/2}$ comes from the relativistic Doppler shift of the photon energy and the factor $\left(1 + \frac{l^2 e^2}{r^2}\right)^{1/2}$ comes from the geometry. Given the

magnitude and direction of the flux, we may calculate an acceleration vector and derive the following equations of motion:

$$\frac{de}{d\tau} = -\xi m (le)^2 e r^{-4} \left(1 - \frac{2m}{r}\right)^{-1}, \quad (A3)$$

$$\frac{d(le)}{d\tau} = -\xi m (le) e^2 r^{-2} \left(1 - \frac{2m}{r}\right)^{-2}, \quad (A4)$$

$$\frac{d^2 r}{d\tau^2} + \frac{m}{r^2} \left(1 + \frac{l^2 e^2}{r^2}\right) - \left(1 - \frac{2m}{r}\right) \frac{l^2 e^2}{r^3} = \xi m e r^{-2} \left(1 - \frac{2m}{r}\right)^{-2}, \quad (A5)$$

where $\xi \equiv \kappa_{\text{T}} L^\infty / 4\pi m$ is a dimensionless parameter.

The first two equations express the Poynting-Robertson effect, which we will not consider in this calculation, assuming l and e are constant on timescales long compared to an orbit time. This assumption will break down when $\xi \lesssim 1$. We multiply equation (A5) by $2\frac{dr}{d\tau}$, add equation (A4) multiplied by $2le\left(1 - \frac{2m}{r}\right)r^{-2}$, and add equation (A3) multiplied by -2 to obtain

$$\frac{d}{d\tau} \left[\left(\frac{dr}{d\tau}\right)^2 - e^2 + \left(1 - \frac{2m}{r}\right) \left(1 + \frac{l^2 e^2}{r^2}\right) \right] = \xi \frac{d}{d\tau} \left[e \log \left(1 - \frac{2m}{r}\right) \right], \quad (A6)$$

where the term $-\xi \frac{de}{d\tau} \log \left(1 - \frac{2m}{r}\right)$ (which is second order in ξ) has been dropped from the right hand side. We obtain an energy equation by integrating, so that

$$\left(\frac{dr}{d\tau}\right)^2 = e^2 - \left(1 - \frac{2m}{r}\right) \left(1 + \frac{l^2 e^2}{r^2}\right) + \xi e \log \left(1 - \frac{2m}{r}\right). \quad (A7)$$

For a marginally stable orbit, we set to zero the first and second derivatives of the right hand side with respect to r . This yields

$$r_{\text{ms}} - 6m = -\xi \frac{2m^2 r}{l^2 e} \left(1 - \frac{2m}{r}\right)^{-2} \approx -2.1 m \xi. \quad (A8)$$

In this case the presence of central radiation decreases the marginally stable radius, so that, for instance, at $L^\infty = 0.1 L_{\text{Edd}}$ we have $r_{\text{ms}} = 5.8m$.

Appendix 2

We may estimate the extent to which the central radiation modifies the inner radius of the accretion disk by estimating the penetration depth of radiation from the star, that is, by estimating the radius r_T at which the optical depth for Thomson scattering becomes 1, calculated radially from the cusp radius. In order to do this, we consider some of the details of the interior of the disk (treating l and s as constant). In the following discussion ρ , p , and e are their equatorial values as a function of r . Consider the third entry of Table 2, and assume the density of material at the pressure maximum is about

$$\rho_{\max} \sim 10^{-1} \text{ g cm}^{-3}. \quad (\text{A9})$$

(This density can be determined accurately only by knowing the details of the mechanism for angular momentum transport. We have chosen a density to be compatible with our assumption that the disk is optically thick, that is, so that $\rho_{\max} \kappa_T z_{\max} \gg 1$.) The pressure at pressure maximum can be obtained by setting $l_{,\beta} = 0$ and $\rho c^2 + p \approx \rho c^2$ in equation (4). After using the equation of state

$$p = p_0 \rho^{4/3} \quad (\text{A10})$$

and integrating, we obtain

$$4p_0^{3/4} p^{1/4} = c^2 \ln(e_0/e), \quad (\text{A11})$$

where we have restored c^2 for this calculation only. (In order to obtain e at the pressure maximum, we note that the pressure maximum coincides with the stable circular orbit with $l = l_0$. Thus e can be obtained by standard methods; see, e.g., Shapiro & Teukolsky 1983, p. 346.) Combining $e(p = p_{\max}) = 0.9447$ with equations (A9), (A10), and (A11) yields $p_0 \sim 4 \times 10^{17} \text{ g}^{-1/3} \text{ cm}^3 \text{ s}^{-2}$ and $p_{\max} \sim 2 \times 10^{16} \text{ erg cm}^{-3}$.

We obtain the radius r_T by setting $\tau \sim 1$, so that

$$1 \sim \tau \sim \kappa_T \int_{r_{\text{in}}}^{r_T} \rho dr \sim \kappa_T \int_{r_{\text{in}}}^{r_T} \left(\frac{p}{p_0} \right)^{3/4} dr \sim \frac{\kappa_T c^6}{64 p_0^3} \int_{r_{\text{in}}}^{r_T} \left[\ln \left(\frac{e_0}{e} \right) \right]^3 dr, \quad (\text{A12})$$

where the integration is radially outward from the cusp, and we have used equations (A10) and (A11). At the equator, the invariant interval $-1 = u \cdot u$ becomes

$$e^{-1} = \left((1 - 2m/r)^{-1} - l_0^2/r^2 \right)^{1/2}. \quad (\text{A13})$$

We integrate equation (A12) numerically using equation (A13) to obtain $r_T = 5.57m$. Thus for $m = 1.45M_\odot$ we obtain

$$r_T - r_{\text{in}} \sim 0.6 \text{ km}. \quad (\text{A14})$$

This calculation also allows us to perform a consistency check for this model of the accretion disk. We idealized the radial component of the velocity in the disk u_r to be negligible. This idealization is reasonable as long as the velocity u_r is much less than the other velocities in the disk, especially the speed of sound v_s . Consider the third entry in Table 2 with $\rho \sim 10^{-1} \text{ g cm}^{-3}$ (*cf.* eq. A9). Then

$$\begin{aligned} u_r &\sim \frac{\dot{M}}{2\pi r h \rho} \\ &\approx 1.5 \times 10^5 \frac{\text{cm}}{\text{s}} \left(\frac{\dot{M}}{9 \times 10^{15} \text{ g s}^{-1}} \right) \left(\frac{10^6 \text{ cm}}{r} \right) \left(\frac{10^5 \text{ cm}}{h} \right) \left(\frac{10^{-1} \text{ g cm}^{-3}}{\rho} \right). \end{aligned} \quad (\text{A15})$$

We can compare this to the sound speed $v_s \sim [(4/3)p_{\text{max}}/\rho_{\text{max}}]^{1/2} \sim 5 \times 10^8 \text{ cm s}^{-1}$. As long as $h \gg 5 \times 10^3 \text{ cm}$ we have $u_r \ll v_s$. If material is slung from a point on the disk outside the radius where $h \sim 5 \times 10^3 \text{ cm}$, then the radial velocities should remain small compared to the velocity of sound, and we are justified in ignoring u_r .

REFERENCES

- Abramowicz, M. A. 1971, *Acta Astr.*, 21, 81.
- Abramowicz, M. A., Czerny, B., Lasota, J. P., & Szuszkiewicz, E. 1988, *ApJ*, 332, 646.
- Abramowicz, M. A., Jaroszyński, M., & Sikura, M. 1978, *A&A*, 63, 221.
- Alme, M., & Wilson, J. 1973, *ApJ*, 186, 1015.
- Alpar, M. A., & Shaham, J. 1985, *Nature*, 316, 239.
- Arnett, W. D., & Bowers, R. L. 1977, *ApJS*, 33, 415.
- Arponen, J. 1972, *Nucl. Phys.*, A191, 257.
- Bethe, H. A., & Johnson, M. 1974, *Nucl. Phys.*, A230, 1.
- Bhattacharya, D., & van den Heuvel, E. P. J. 1991, *Phys. Reports*, 203, 1.
- Bowers, R. L., Gleeson, A. M., & Pedigo, R. D. 1975, *Phys. Rev.*, D12, 3043.
- Chakrabarti, S. K. 1985, *ApJ*, 288, 1.
- Fortner, B., Lamb, F. K., & Miller, G. S. 1989, *Nature*, 342, 775.
- Fujimoto, M. Y., & Hoshi, R. 1985, *ApJ*, 293, 268.
- Goodman, J., Narayan, R., Goldreich, P. 1987, *MNRAS*, 225, 695.
- Hartle, J. B., & Thorne, K. S. 1968, *ApJ*, 153, 807.
- Hasinger, G. 1988, "Status of Observation and Understanding of QPO" in *Physics of Neutron Stars and Black Holes*, ed. Y. Tanaka (Universal Academy Press: Tokyo), p. 97.
- Hasinger, G. 1991, "X-ray Diagnostics of Accretion Disks", in *Rev. of Mod. Astron.*, 3, 60.
- Hasinger, G., van der Klis, M., Ebisawa, K., Dotani, T., & Mitsuda, K. 1990, *A&A*, 235, 131.

- Hawley, F. J. 1991, ApJ, 381, 496.
- Jaroszyński, M., Abramowicz, M. A., & Paczyński, B. 1980, Acta Astr., 30, 1.
- Kluźniak, W., & Wagoner, R. V. 1985, ApJ, 297, 548.
- Kluźniak, W., & Wilson, J. R. 1991, ApJ, 372, L87.
- Matsumoto, R., Kato, S., Fukue, J., & Okazaki, A. T. 1984, Publ. Astron. Soc. Japan, 36, 71.
- Meegan, C. A., Fishman, G. J., Wilson, R. B., Paciesas, W. S., Pendleton, G. N., Horack, J. M., Brock, M. N., & Kouveliotou, C. 1992, Nature, 355, 143.
- Miller, G. S., & Lamb, F. K. 1992, ApJ, 388, 541.
- Misner, C. W., Thorne, K. S., & Wheeler, J. A. 1973, *Gravitation* (W. H. Freeman and Company, New York) (MTW).
- Moszkowski, S. 1974, Phys. Rev., D9, 1613.
- Murakami, T., Fujii, M., Hayashida, K., Itoh, M., Nishimura, J., Yamagami, T., Conner, J. P., Evans, W. D., Fenimore, E. E., Klebesadel, R. W., Yoshida, A., Kondo, I., & Kawai, N. 1988, Nature, 335, 234.
- Novikov, I. D., & Thorne, K. S. 1973, "Black Hole Astrophysics" in *Black Holes*, ed. C. DeWitt & B. DeWitt (Gordon and Breach: New York), p. 343.
- Nowak, M. A., & Wagoner, R. V. 1991, ApJ, 378, 656.
- Nowak, M. A., & Wagoner, R. V. 1992, ApJ, 393, 697.
- Pandharipande, V. 1971a, Nucl. Phys., A174, 641.
- Pandharipande, V. 1971b, Nucl. Phys., A178, 123.
- Papaloizou, J., & Pringle, J. E. 1984, MNRAS, 208, 721.
- Pringle, J. E. 1977, MNRAS, 178, 19.
- Pringle, J. E., & Savonije, G. J. 1978, MNRAS, 187, 777.

- Rybicki, G. B., & Lightman, A. L. 1979, *Radiative Processes in Astrophysics* (New York, John Wiley and Sons).
- Schulz, N. S., & Wijers, R. A. M. J. 1991, preprint, submitted to A&A.
- Seguin, F. J. 1975, ApJ, 197, 745.
- Shakura, N. I., & Sunyaev, R. A. 1988, Adv. Space Res., 8, 135.
- Shapiro, S. L., & Teukolsky, S. A. 1983, *Black Holes, White Dwarfs, and Neutron Stars* (John Wiley & Sons, Inc., New York).
- Sunyaev, R. A., & Shakura, N. I. 1986, Sov. Astron. Lett., 12, 117.
- Tan, J., Lewin, W. H. G., Hjellming, R. M., Penninx, W., van Paradijs, J., van der Klis, M., & Mitsuda, K. 1992, ApJ, 385, 314.
- Tylenda, R. 1981, Acta Astr., 31, 267.
- van der Klis, M. 1989, ARAA, 27, 517.
- van der Klis, M., Jansen, F., van Paradijs, J., Lewin, W. H. G., van den Heuvel, E. P. J., Trümper, J., & Sztajno, M. 1985, Nature, 316, 225.
- Vrtilek, S. D., Penninx, W., Raymond, J. C., Verbunt, F., Hertz, P., Wood, K., Lewin, W. H. G., & Mitsuda, K. 1991, ApJ, 376, 278
- White, N. E., Peacock, A., Hasinger, G., Mason, K. O., Manzo, G., Taylor, B. G., & Branduardi-Raymont, G. 1986, MNRAS, 218, 129.
- Walker, M. A. 1992, ApJ, 385, 661.
- Wood, D., Lewin, W. H. G., and Mitsuda, K. 1991, ApJ, 376, 278.
- Zel'dovich, Ya., & Shakura, N. 1969, Soviet Astron.-AJ, 13, 175.